Durchgeführt am Max-Planck-Institut für Herz- und Lungenforschung,

W.G. Kerckhoff-Institut Bad Nauheim

Enhanced H3K4me3 demethylation by inhibition of fatty acid oxidation enables heart regeneration in adult mice

INAUGURAL-DISSERTATION

zur Erlangung des Doktorgrades der Naturwissenschaften

- Doctor rerum naturalium -

(Dr. rer. nat.)

vorgelegt dem

Fachbereich für Biologie und Chemie (FB 08)

der Justus-Liebig-Universität Gießen

eingereicht von

Xiang Li

Gießen 2021

Die vorliegende Arbeit wurde am Max-Planck-Institut für Herz- und Lungenforschung, W.G. Kerckhoff-Institut in Bad Nauheim angefertigt.

Erstgutachter:

Prof. Dr. Dr. Thomas Braun

Abteilung Entwicklung und Umbau des Herzens

Max-Planck-Institut für Herz- und Lungenforschung

Ludwigstraße 43, 61231 Bad Nauheim

Zweitgutachter:

Prof. Dr. Reinhard Dammann

Institut für Genetik

Justus-Liebig-Universität Giessen

Heinrich-Buff-Ring 58-62

35392 Giessen

Datum der Disputation:

EIDESSTATTLICHE ERKLÄRUNG

„Ich erkläre: Ich habe die vorgelegte Dissertation selbständig und ohne unerlaubte fremde Hilfe und nur mit den Hilfen angefertigt, die ich in der Dissertation angegeben habe. Alle Textstellen, die wörtlich oder sinngemäß aus veröffentlichten Schriften entnommen sind, und alle Angaben, die auf mündlichen Auskünften beruhen, sind als solche kenntlich gemacht. Bei den von mir durchgeführten und in der Dissertation erwähnten Untersuchungen habe ich die Grundsätze guter wissenschaftlicher Praxis, wie sie in der „Satzung der Justus-Liebig-Universität Gießen zur Sicherung guter wissenschaftlicher Praxis“ niedergelegt sind, eingehalten.“

Bad Nauheim, den

ZUSAMMENFASSUNG

Im Laufe der Herzentwicklung wechselt das metabolische Profil kurz nach der Geburt von der Glykolyse zur Oxidation der Fettsäuren (engl. fatty acid oxidation, FAO). Gleichzeitig durchlaufen Kardiomyozyten (engl. cardiomyocyte, CM) eine Reifung, gekennzeichnet durch ein intensives hypertrophisches Wachstum, eine Chromatinrekonfiguration, den Umbau der Zytoarchitektur und den Austritt aus dem Zellzyklus. Die darauffolgenden strukturellen und funktionellen Veränderungen adulter CM weisen auf umfangreiche Änderungen der Transkriptionsnetzwerke hin, die von den epigenetischen Mechanismen gemeinsam mit umweltbedingten und metabolischen Signalen gesteuert werden.

Aktuelle Studien zum Zellstoffwechsels haben gezeigt, dass Metabolite aus diversen Stoffwechselwegen als Cofaktoren oder Substrate für verschiedene epigenetische Modifikatoren agieren und dadurch die Chromatin-abhängige Genregulation mit dem metabolischen Status verknüpfen. Um einen tieferen Einblick in die Verbindungen zwischen epigenetischen Prozessen und Stoffwechselwegen während der Entwicklung, der Reifung und der Regeneration des Herzens zu gewinnen, habe ich die metabolische Neuprogrammierung durch Ausschaltung des für FAO kritischen (besonders in den Kardiomyozyten) CPT1b-Enzym blockiert. Die Inaktivierung von Cpt1b in Herzmuskelzellen führte zur Kardiomegalie und verbesserte die Herzfunktion nach experimentell induzierten Myokardinfarkten. Die konnte vor allem auf die vermehrte Proliferation der Kardiomyozyten und auf die erhöhte Widerstandsfähigkeit zur ischämischen Schäden zurückgeführt werden. Bemerkenswert ist, dass die Inhibition der FAO nach Verlust des Cpt1b die intrazelluläre Konzentration von Acetyl-CoA (eines wichtigen Metaboliten, der überwiegend von der FAO produziert wird) nicht veränderte, was auf die erhöhte von Verstoffwechslung von Glukose und Aminosäuren bedingt ist. Die Cpt1b-Inaktivierung führte zudem infolge einer erhöhten Produktion und eines verminderten Verbrauchs zu einer ausgeprägten Erhöhung der intrazellulären αKG-Spiegel. Der erhöhte αKG-Spiegel resultierte in einer Aktivitätssteigerung des KDM5-Enzyms, was die Demethylierung von H3K4me3 in Promotorregionen verschiedener für kardiale Entwicklung und Reifung relevanter Gene bedingte. Durch die reduzierte Expression von kardialen Reifungsgenen nahmen adulte Kardiomyozyten einen unreifen, proliferationskompetenten Zustand an.

Die gewonnenen Erkenntnisse enthüllten ein kritisches Zusammenspiel zwischen epigenetischen und metabolischen Vorgängen bei der Regulation der Zellzustandserhaltung und der Funktion von Kardiomyozyten. Der mitochondriale oxidative Stoffwechsel wurde als ein vielversprechendes Target der Therapie von Herzinsuffizienz identifiziert. Die Manipulation von Histon-

modifizierenden Enzymen durch Eingriffe in den Zellmetabolismus erwies sich darüber hinaus als effektives Instrument um Regenerationsprozesse im adulten Herzen zu aktivieren. Als epigenetischer Effektor, der metabolische Signale erkennen kann, ist KDM5 ein attraktive Zielstruktur für die Behandlung von Herzerkrankungen.

SUMMARY

During early postnatal heart development, the metabolic profile switches from glycolysis to fatty acid oxidation (FAO). At the same time, cardiomyocytes (CM) undergo profound maturation characterized by hypertrophic growth, cytoarchitectural remodeling, chromatin reconfiguration, and cell cycle withdrawal. The subsequent structural and functional alterations in mature CM indicate synergistic rewiring of transcriptional networks regulated by epigenetic mechanisms in combination with environmental and metabolic signals.

Recent studies of cellular metabolism demonstrated that metabolites derived from various metabolic pathways function as cofactors or substrates for distinct epigenetic modifiers, thereby coupling chromatin-dependent gene regulation with the metabolic state. To gain a deeper insight into the interplay between epigenetic processes and metabolic pathways during cardiac development, maturation, and heart regeneration, I prevented metabolic maturation by cardiomyocyte-specific inactivation of CPT1B, a crucial enzyme for FAO. *Cpt1b* inactivation led to cardiomegaly and attenuated cardiac damage after myocardial injury due to augmented CM proliferation and enhanced resistance to ischemic injury. Interestingly, FAO inhibition after the loss of *Cpt1b* did not reduce the intracellular level of acetyl-CoA, which is an essential metabolite mainly produced by FAO, due to enhanced metabolic compensation from glucose and amino acids. In contrast, *Cpt1b* inactivation led to marked accumulation of αKG, caused by increased generation but decreased consumption. Excessive αKG was sensed by KDM5, leading to demethylation of cell-specific broad H3K4me3 peaks located in promoters of key genes driving cardiac development. Demethylation of H3K4me3 reduced expression of cardiac maturation genes, converting cardiomyocytes to a more immature, proliferation-competent state.

Overall, the results obtained for the thesis uncover a complex interplay between epigenetics and metabolic pathways for regulating the maintenance of CM maturity and cell cycle arrest. The study identifies mitochondrial oxidative metabolism as an attractive target to treat heart failure. Manipulation of metabolic processes were found to alter epigenetic events in the nucleus, which was exploited to regenerate diseased hearts. Furthermore, my research uncovered that KDM5 senses metabolic cues to deactivate crucial cardiac maturation genes, which offers new perspectives to treat heart diseases.

Contents

Introduction

1. Heart development, remodeling and regeneration

The life of all animals depends on continuous function of the heart and heart diseases are one of the leading causes of death worldwide. Various heart diseases may lead to catastrophic consequences, often associated with loss or dysfunction of cardiomyocyte (CM), the cell responsible for generating contractile force in the heart. Myocardial damage causes heart remodeling, heart failure, and eventually death. In the past decades, numerous efforts have been made to understand the molecular mechanisms modulating the myocardial response to injury, including immunological response, metabolic reprograming, and epigenetic rewiring of gene transcription. Although *bona fide* regeneration of the damaged human heart is still an unmet ambition due to the very limited proliferative capacity of adult CMs, the advance in discovery of fundamental principles in heart development, remodeling and regeneration have provided a framework for hypothesis-driven approaches towards the ultimate goal of adult heart regeneration and repair.

1.1 Heart development-prenatal cardiogenesis

Although many differences exist between cardiac regeneration and cardiogenesis, the regenerating heart shares certain hallmarks of embryonic and postnatal development, in that embryonic/neonatal-specific factors are repurposed upon injury to initiate heart regeneration. The heart originates from the cardiac mesoderm and is the first organ to form and function during embryogenesis (Garcia-Martinez and Schoenwolf, 1993; Tam et al., 1997). Around embryonic day E6.5, cardiac markers are first detected in mesodermal progenitors that migrate into splanchnic mesoderm to form the heart fields. At E7.5, the primary heart field (FHF) fuse at the midline thereby forming the cardiac crescent. The FHF progenitors, which eventually contribute to the formation of the left ventricle and atria, start to differentiate at E8.0 to form the beating, linear heart tube. At the same time, the second heart field (SHF) progenitors, which originate from extracrescent tissue, gradually migrate into the linear heart tube and differentiate to CMs that contribute to the formation of the outflow tract, right ventricle, and atria. From E8.5 to E10.5, the beating linear heart tube starts uneven growth and looping to form the more complex four-chambered heart. The valves within ventricles are constituted at E15, which indicates completion of a fully functional four-chambered heart (Fig 1a) (Buckingham et al., 2005; Olson, 2006; Srivastava, 2006).

The process of cardiac development is controlled tightly by a complex network of signaling pathways including Bone morphogenetic protein (BMP), WNT, Notch, and Sonic hedgehog (Shh) (Xin et al., 2013b). Both WNT and BMPs serve as the early inductive signals promoting differentiation of cardiac mesoderm. At early stages, the canonical Wnt/β catenin signal (WNT3A) directs migration of mesoderm posterior 1(Mesp1) positive cells and formation of the anterior and lateral plate mesoderm. Afterward, the Wnt/β catenin signal pathway has to be silenced to promote the cardiac progenitor cell specification in the primary heart fields (Lescroart et al., 2014; Yue et al., 2008). Within the secondary heart field, the Wnt/β catenin signal pathway facilitates the expansion of progenitor cells and promotes the expression of Islet1 (Isl1), which is a core transcription factor expressed in the early stage of FHF and required for SHF development (Bu et al., 2009). BMPs (BMP2, BMP4, BMP5, and BMP7) induce expression of early essential transcription factors in the Mesp1 positive cell population, including *Gata4*, *Tbx20*, *Tbx5*, *Hand2*, *Nkx2.5*, and *Mef2c*, which regulate the cardiac lineage-specific gene expression (Fig 1b) (Galdos et al., 2017; Lopez-Sanchez and Garcia-Martinez, 2011).

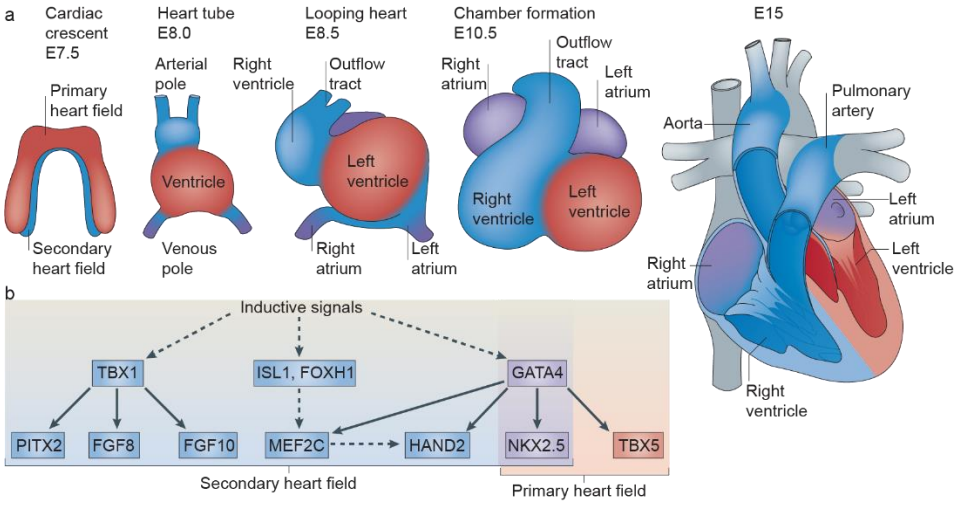

Fig 1. Developmental stages and regulation of cardiogenesis.

(a) Developmental stages of mouse embryonic heart. (b) Critical transcriptional network during early cardiogenesis (Xin et al., 2013b).

The Notch pathway mainly contributes to the coordination of cardiac precursor development during early cardiac lineage commitment and restricts premature differentiation of progenitor cells by counteracting the Wnt/β catenin pathway in Isl1 lineage (Kwon et al., 2009; MacGrogan et al., 2018). The Notch signal pathway also works synergistically with BMPs to promote transcription of *Snail1* and *Snail2* and protein translocation into the nucleus, thereby promoting Endothelial-Mesenchymal Transition (EndoMT) for valve development (Wang et al., 2013). The Hippo signaling pathway

regulates cardiac growth and controls heart size during heart development (Heallen et al., 2011; von Gise et al., 2012; Wang et al., 2018; Xin et al., 2011). TAZ, a component of the Hippo signaling pathway works as co-factor of TBX5 to regulate early cardiogenesis (Murakami et al., 2005). Sustained YAP activation in nuclei after *Sav* inactivation in cardiac progenitor cells leads to a cardiomegaly phenotype due to markedly enhanced CM proliferation (Heallen et al., 2011).

1.2 Heart development-fetal and postnatal CM maturation

Embryonic/fetal CM divide rapidly to increase cardiac mass during heart development, but the proliferative capacity of CMs declines strongly after birth. Instead, neonatal CMs undergo postnatal maturation during the first two weeks after birth, characterized by profound hypertrophic growth, metabolic reprograming, and cytoarchitectural remodeling until a fully differentiated state is reached. Maturation is essential to cope with the substantial increase in cardiac workload after birth. After a short term of hyperplastic growth (p1-p3), increasement of cardiac mass is achieved mainly through hypertrophic growth, typically achieved by uncoupling of DNA synthesis from karyokinesis and cytokinesis, which leads to polyploidy and multi-nucleated CMs (Gilsbach et al., 2018; Mollova et al., 2013). Functional changes of mature adult CMs include formation of an electromechanical syncytium via gap and adhesive junctions between adjacent CM (Dai et al., 2017; Yang et al., 2014). A fully mature mouse CM presents with rod-like shape, approximately 150µm in length, 20µm in width, and 15µm in height (Fig 2) (Gerdes et al., 1992).

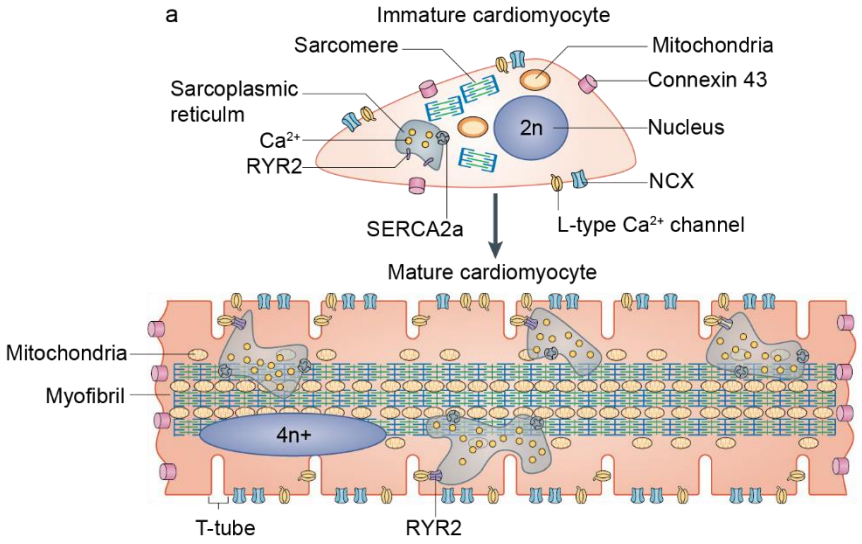

Figure 2. Dynamic structural and functional changes during CM maturation (Karbassi et al., 2020).

CMs in the adult mammalian heart turn over at a very low rate and are incapable of expansion to replenish the damaged cells following myocardial injury, since the adult CM permanently exits the cell cycle along with postnatal maturation (Adler and Friedburg, 1986; Bergmann et al., 2009; Brodsky et al., 1980; Soonpaa et al., 1996). The expression levels of cyclin and cyclin-dependent kinase (CDK) in adult CM are markedly reduced compared to proliferating fetal/neonatal CM (Brooks et al., 1997; Kang et al., 1997). Forced overexpression of cyclins such as cyclin B1, cyclin D2, cyclin A2, and their upstream regulator E2F but ablation of cell cycle inhibitors, like *p21*, are able to induce CM cell cycle re-entry and hyperplasia but only to a limited extent (Mohamed et al., 2018; Yuan and Braun, 2017; Zhang et al., 2017). Cell cycle arrest of adult CM might be induced, at least partially, by oxidative stress and resulting DNA damage after the metabolic shift from glycolytic metabolism in fetal hearts toward highly oxidative metabolism depending on fatty acid utilization rapidly after birth (Puente et al., 2014). Oxidative stress can activate Hippo signaling pathway, resulting in inhibition of YAP nuclear translocation and transcriptional repression of cell-cycle related genes (Heallen et al., 2011; Lin et al., 2016; Morikawa et al., 2017). The profound changes in the cell cycle machinery caused by the down-regulation of numerous essential cell cycle regulators contribute to endoreduplication or arrest of karyokinesis/cytokinesis, leading to multinucleation and polyploidization in adult CM. In both mouse and human, CM proliferation and functional recovery of the heart after myocardial infarction are positively correlated with the content of mononuclear diploid CMs before injury, suggesting that some mononuclear diploid CMs may maintain a certain proliferative potential and contribute at low level to heart regeneration after injury (Herget et al., 1997; Laflamme and Murry, 2011; Patterson et al., 2017).

Formation and organization of sarcomere, the basic functional contractile unit of cardiac muscle, depends on the expression of myofibrillar proteins, such as myosin heavy chain, titin, α-actin, and troponin, and occur in both immature and mature CMs (Fig 2). One of the hallmarks of CM maturation is sarcomere expansion and ultrastructure reorganization accompanied with sarcomeric isoform switching, in which several sarcomere components switch from a fetal to an adult isoform due to transcriptional changes or alternative splicing (Guo and Pu, 2020). For instance, the predominant myosin heavy chain switches from fetal β-isoform (MYH7) to adult α-isoform (MYH6) in rodents (Mahdavi et al., 1984). Fetal CMs primarily express the slow skeletal muscle isoform of troponin (ssTni, Tnni1), which is replaced by the cardiac isoform (cTni, Tnni3) in adult CMs (Gorza et al., 1993; Sabry and Dhoot, 1989). The regulatory myosin light chain 2 (Mlc2a) is predominantly expressed in early fetal CMs (E9.5), but its isoform Mlc2v is significantly up-regulated from prenatal to fetal and neonatal stages (Chuva de Sousa Lopes et al., 2006; Giudice et al., 2014). Likewise, smooth muscle α-actin

(ACTA2) is mainly expressed in embryonic CM, but its expression drops to nearly undetectable levels in postnatal CMs (Black et al., 1991). The relative amount of skeletal muscle α-actin (ACTA1) increases during fetal development until reaching a peak at birth but rapidly decreases in the adult rodent heart, while the expression of cardiac actin (ACTC1) predominates in mature adult CM (Gillespie-Brown et al., 1995; Vandekerckhove et al., 1986). The expression levels of ACTA1 and ACTA2 increase in de-differentiating CMs or failing hearts, indicating activation of the 'fetal gene' transcriptional program (Suurmeijer et al., 2003). In addition, alternative splicing also contributes to sarcomeric isoform switching, facilitating the switch of titin mRNA from the longer isoform N2BA to the short isoform N2B, which encodes the stiff Titin in matured CM (Hinson et al., 2015).

Generation of fully functional action potentials via ion transportation through the membrane is another hallmark of CM maturation (Liu et al., 2016a). During early cardiogenesis, CMs are electrically silent. However, CM's depolarization at fetal and neonatal stages is facilitated by sodium-calcium exchange, which stabilizes action potentials for a spontaneously beating heart (Carmeliet, 2019). The dynamic calcium flux mainly happens via the T-tube in adult CMs. An wave of calcium release from the sarcoplasmic reticulum (SR) occurs after activation of the ryanodine receptor (RYR2), which regulates the heart contraction and relaxation cycle (Bers, 2002). In the cytosol, calcium binds to components of the myofilament (troponin C) to induce sliding of filaments in sarcomeres, which eventually causes contraction of CM. During the relaxation phase, calcium is either transported by ATPase2a (SERCA2a) into the sarcoplasmic reticulum (SR) or exported from CM through the sodium-calcium exchanger (Bers, 2002). Both RYR2 and SERCA2a are lowly expressed during fetal stages, but expression levels increase dramatically during the postnatal maturation process (Giudice et al., 2014). The calcium handling ability, which regulates oscillation of calcium concentrations in the cytosol, is strongly associated with proper CM function and maturation.

Another major biological process during CM maturation is the metabolic switch from anaerobic glycolysis to fatty acid oxidation. In the prenatal and fetal hearts, glycolysis is the main metabolic pathway to generate ATP, and fatty acid oxidation only counts for 15% of energy production (Werner et al., 1989). However, over 70% of ATP is generated associated with fatty acid oxidation one week after birth (Lopaschuk et al., 1991). Likewise, the total number of mitochondria dramatically increases (up to 40% of cell volume in adult CM) and the morphology of mitochondria turns from a small round shape with few and poorly aligned cristae to a significantly larger oval shape with densely organized cristae in the fully matured adult CM (Schaper et al., 1985; Scuderi and Butcher, 2017). CM maturation

also involves a remarkable rearrangement of the cytoarchitecture. In immature CM, the mitochondria mainly localize around the nucleus, while mitochondria in adult CM are usually arranged in packed strands running between myofibrils (Galdos et al., 2017; Palmer et al., 1977; Saks et al., 2012). Mitochondria are also attached to the SR, potentially through ER-mitochondria contact sites (Figure 2). This close organization leads to efficient ATP transport from mitochondria to ATPases in sarcomeres and SR to support contraction (Seppet et al., 2001).

1.3 Heart remodeling- cardiac hypertrophy

During postnatal heart development, cardiac mass increases mainly through hypertrophic growth of individual CM instead of an increase of CM numbers. This physiological hypertrophic growth results in the addition of the sarcomere units to strengthen heart contractility and reduce ventricular wall stress at the organ level, thereby fulfilling the demand for enhanced heart contraction due to increased postnatal workload (Nakamura and Sadoshima, 2018). Physiological hypertrophy differs from pathological hypertrophy, which initially develops as an adaptive response to multiple harmful stimuli but often progresses to heart failure. Pathological hypertrophy results from a combination of several adverse signals and indicates a bad prognosis for the course of cardiac diseases (Fig 3).

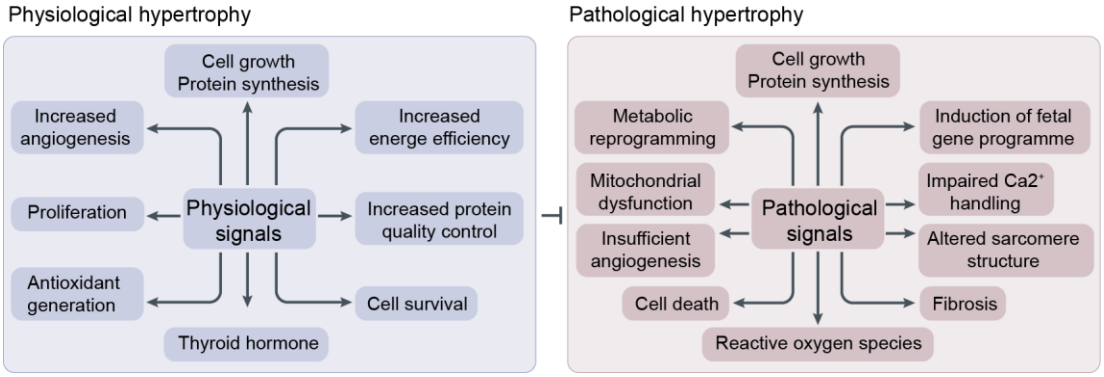

Figure 3. General features of physiological and pathological cardiac hypertrophy (Nakamura and Sadoshima, 2018).

1.3.1 Physiological hypertrophy

Besides the physiological hypertrophy during postnatal heart maturation, exercise training or pregnancy are also able to induce physiological hypertrophy, leading to around 10-20% increase in cardiac mass and enhanced heart contractility (Heineke and Molkentin, 2006; Perrino et al., 2006; Vega et al., 2017). Notably, physiological cardiac hypotrophy is fully reversible without evident interstitial fibrosis and cell death (Schiattarella and Hill, 2015). Elevated serum level of insulin-like growth factor1 (IGF1) and insulin-like growth binding protein 2 (IGFBP2) during exercise and pregnancy are assumed

to activate the PI3K-AKT1-mTOR and MAPK signaling pathway, promote protein synthesis and cell growth, thus leading to a physiological gain of cardiac mass (Kim et al., 2008; McMullen et al., 2004; Neri Serneri et al., 2001; Olszanecka et al., 2017). Exercise-induced activation of the PI3K-AKT1 pathway might inhibit transcription of CCAAT/enhancer-binding protein β (C/EBPβ), which negatively regulates CM proliferation by suppressing expression of *Gata4* and *Nkx2.5* (Bostrom et al., 2010). Additionally, mTOR activation promotes *Hif1a* expression, which favors angiogenesis by promoting *Vegf* expression in exercise-induced hypertrophy. As a consequence, the capillary network increases in proportion to increased cardiac mass during exercise-induced physiological hypertrophy, which efficiently supplies the cardiac muscle with nutrients and O_2 (Hamasaki et al., 2000; Nakamura and Sadoshima, 2018; Oka et al., 2014).

1.3.2 Pathological hypertrophy

Chronic hypertension, aortic stenosis, obesity, diabetes, and myocardial infarction can induce pathological cardiac hypertrophy, which initially reflects an adaptive response to increased pressure (Devereux et al., 2000; Turkbey et al., 2010). However, subsequent maladaptive processes can lead to ventricular dilation characterized by reduced wall thickness, severe fibrosis, reduced contractility, and eventually heart failure (Dunlay et al., 2017; Mohammed et al., 2015). Pathological cardiac hypertrophy can be induced by increased levels of angiotensin II or endothelin 1 in hypertension patients, which increases pressure and reduces the Ca^{2+} handling ability (Braz et al., 2004; Zhang et al., 2013). Similar to physiological hypertrophy, mTOR activity is also increased in pathological hypertrophy, allowing increased protein synthesis and mitochondrial quality control. However, sustained activation of mTOR signaling during pathological cardiac remodeling process can lead to reduced protein quality control via inhibition of autophagy (Zhang et al., 2010). Pharmaceutical inhibition of mTOR1 attenuates the angiotensin-II induced pathological cardiac remodeling (Sadoshima and Izumo, 1995; Shioi et al., 2003). Interstitial fibrosis as an outcome of hyper-proliferation of cardiac fibroblast, the primary cell that constitutes around 15% of the heart's non-CM population and contributes to collagen deposition, is observed specifically during pathological cardiac remodeling, leading to enhanced stiffness and contractile dysfunction (Pinto et al., 2016). The non-canonical SMAD-TAK1 signaling pathway activates fibroblasts through elevated *Tgfβ* expression, further contributing to severe fibrosis and reduced contractility (Koitabashi et al., 2011; Kuwahara et al., 2002; Zhang et al., 2000). In addition, the re-expression of embryonic or fetal CM genes e. g. *Nppa*, and *Nppb*, which are transcriptionally unchanged or even decreased in physiological hypertrophy, is a hallmark of pathological hypertrophy

in the adult heart, indicating that the different forms of hypertrophy are regulated by distinct cellular signaling pathways (Holtwick et al., 2003; Rainer and Kass, 2016).

1.4 Heart Regeneration

Based on the current knowledge of cardiac development, animal models of heart injury repair, and clinical observations, five hallmarks of cardiac regeneration including re-muscularization, electromechanical stability, resolution of fibrosis, immunological balance, angiogenesis, and arteriogenesis have been proposed (Fig 4) (Bertero and Murry, 2018). Over the decades, multiple factors involved in the regulation of cardiac regeneration have been identified.

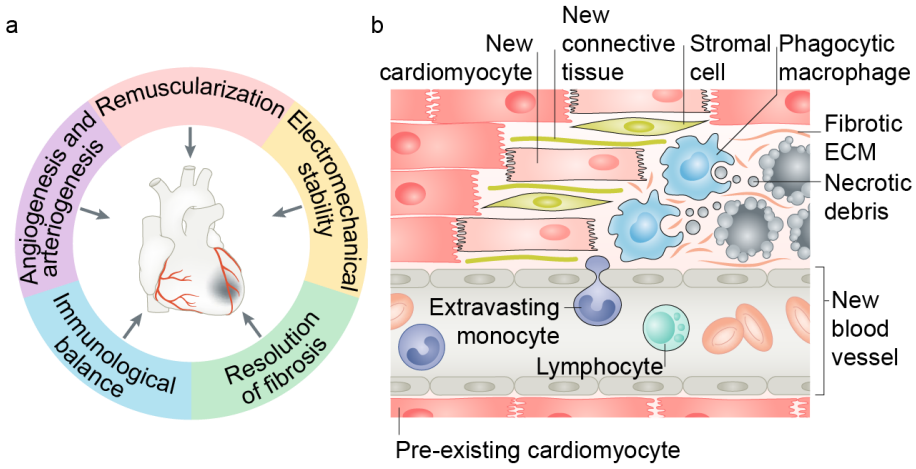

Figure 4. Properties of the regenerating heart.

(a) Hallmarks for heart regeneration (b) Cell types and process involved for optimal cardiac regeneration (Bertero and Murry, 2018)

1.4.1. Targeting the cell cycle machinery to promote heart regeneration

During cardiac regeneration, expansion of the primary function units, CMs, within the damaged area is the most critical step for functional regeneration. In general, there are three basic ways to achieve this goal: stimulation of CM proliferation from preexisting CMs; reprogramming non-myocytes into CMs; transplantation of exogenous stem cell or progenitor cells with cardiogenic potential or of fully differentiated CMs (Bertero and Murry, 2018). Based on different experimental approaches it has been demonstrated that a life-long symmetric division of CM occurs at very low rates in adult mouse hearts (5.5% in young adults and 2.6% in old mice) (Senyo et al., 2013), indicating the possibility of cardiac regeneration by stimulating proliferation of pre-existing adult CM. Efficient proliferation may be limited to a subset of mononucleated, diploid CMs, which are maintained in a hypoxic

microenvironment (Patterson et al., 2017; Senyo et al., 2013). By modulating developmental signal pathways or expression of cell cycle regulators directly promoting cell cycle re-entry of adult CM, cytokinesis of CMs may be accomplished. For example, forced overexpression of *Ccnb1*, *Ccnd1*, *Ccnd2*, and *Ccna2* individually or combined overexpression of *Cdk1*, *Cdk4*, *Ccnb1*, and *Ccnd* in cardiac lineage can stimulate the cell cycle activity of adult CM (Bicknell et al., 2004; Chaudhry et al., 2004; Leach et al., 2017; Leach and Martin, 2018; Pasumarthi et al., 2005; Soonpaa et al., 1997). Furthermore, inactivation of *p21* or *p27* elevates the self-renewal rate of CM in the murine heart (Flink et al., 1998; Foglia and Poss, 2016). In addition, CM-specific ablation of *Meis1*, which functions as a transcription co-activator of p15, p16, and p21, promotes CM proliferation after myocardial infarction (Mahmoud et al., 2013; Yuan and Braun, 2013).

1.4.2 Reactivation of developmental pathway restores CM proliferation

Since dedifferentiation of specified cell types is a pervasive process for tissue regeneration in diverse organs including the heart, attempts have been made to improve repair of cardiac damage by re-activating development-associated signaling pathways. For instance, ablation of Hippo signaling pathway components e. g. *Mst1*, *Mst2*, *Lats2,* or *Sav1* in CMs were reported to facilitate nuclear translocation of YAP1, thereby promoting CM proliferation and re-muscularization of the damaged heart (Heallen et al., 2013; Heallen et al., 2011; Xin et al., 2013a). Activation of neuregulin (NRG1) signaling by expressing of constitutively active *Erbb2*, a NRG1 receptor that is required for CM proliferation at embryonic/neonatal stages, has been shown to promote CM proliferation and initiate a cycle of CM dedifferentiation, proliferation, and redifferentiation during myocardial infarctions in juvenile and adult mouse heart (D'Uva G, et al., 2015). Moreover, an increased levels of GATA4, a cardiac transcription factor that plays an essential role to promote cardiac development by driving the embryonic CM proliferation, leads to improved cardiac regeneration at P7 (Mohammadi et al., 2017). Moreover, reintroduction of PKM2, an isoenzyme of the glycolytic enzyme pyruvate kinase expressed in fetal/neonatal but not in adult CMs, enhances proliferation of CMs, cardiac function, and long-term survival through increasing glycolytic flux and boosting the biosynthetic pentose phosphate pathway which is essential for cell growth and proliferation (Magadum et al., 2020).

1.4.3 Reconstruction of a pro-proliferative microenvironment favors heart regeneration

Resolution of fibrosis and reconstruction of the extracellular matrix (ECM) is another hallmark for functional heart regeneration. Myofibroblast activation and proliferation in the necrosis area after

myocardial damage leads to clearance of debris from dead cells and matrix and promotes subsequent formation of a mature cross-linked scar, which is beneficial for the healing process. However, excessive fibrosis in the scar increases stiffness and induces cardiac remodeling (Weber et al., 2013). Multiple pathways, such as the Wnt, angiotensin II, and TGFβ1 signaling pathways, are involved in cardiac fibrosis. Inhibition of these pathways or factors has beneficial effects on heart regeneration (Duan et al., 2012; Sassoli et al., 2013). However, the timing of interventions to resolve fibrosis is exceptionally critical for heart regeneration, since fibrosis is required for the initial healing phase after myocardial damage. Reconstruction of a pro-proliferative ECM with a single administration of Agrin, a component of the neonatal extracellular matrix, promotes cardiac regeneration in adult mice after myocardial infarction (Bassat et al., 2017). Intraepicardial delivery of Periostin, another ECM component normally expressed during cardiac development but also re-expressed following injury, promotes adult CM proliferation and cardiac repair after infarction (Kuhn et al., 2007; Polizzotti et al., 2012). Dynamic phenotypic and functional alterations of cardiac fibroblasts following myocardial infarction triggers immune responses, which have multiple functions in clearing necrotic cells, activating cardiac fibroblast, and promoting angiogenesis (Nahrendorf, 2018). Treatment of CMs with inflammatory cytokine Oncostatin M (OSM) induces dedifferentiation of adult CM and elevates expression of *Reg3β*, which is required for sufficient cardiac repair, via activation of the JAK/STAT3 signaling pathway, (Kubin et al., 2011; Lorchner et al., 2015). Notably, reduction of the influx of neutrophils, specifically in the epicardial area, benefits heart regeneration (Huang et al., 2012). Moreover, immune response, the paracrine effect from CM, and stroma cells stimulates angiogenesis, thereby enhancing supply of oxygen and nutrients for better heart regeneration (Bertero and Murry, 2018). It has been shown that collateral vessel formation from pre-existing arteries limits myocardial infarction damage in the neonatal stage before P7 (Das et al., 2019).

2. Metabolic reprogramming in heart regeneration and remodeling

2.1 Glycolysis promotes while FAO attenuates CM proliferation and heart regeneration

Before birth, the fetal CM strongly relies on anaerobic glycolysis as the main source for energy production (Zhou et al., 2011). Multiple intermediate metabolites serve as building blocks for synthesis of macromolecules to support cell growth and division (Quaife-Ryan et al., 2016). The rapid switch to fatty acids oxidation after birth promotes ROS production in mitochondria and causes DNA damage,

which leads to withdrawal of CMs from the cell cycle (Puente et al., 2014). Therefore, sustaining the CM at the glycolytic state might contribute to better cardiac regeneration in response to myocardial infarction. Supporting this line of reasoning, it has been reported that a rare population of adult CM, which maintains the ability of self-renewal, resides in a hypoxic niche within the myocardium. Gradual exposure to severe systemic hypoxemia induces robust regenerative responses through reactivation of mitosis in pre-existing CM (Kimura et al., 2015; Nakada et al., 2016). Impaired glycolysis after inactivation of PKM2, a key enzyme in the glycolysis pathway, decreases the number of proliferating CM following injury (Magadum et al., 2020). In contrast, ectopic overexpression of *Pkm2,* the enzyme that promotes production of pyruvate in the heart, thereby stimulating glycolysis, improves heart function in response to both chronic and acute cardiac infarction (Magadum et al., 2020). Another experimental evidence supporting the beneficial effect of glycolysis on CM proliferation and heart regeneration is a recent study, which demonstrates that an increase in pyruvate dehydrogenase activity and consequently glucose oxidation, through conditional deletion of PDK4 improves heart regeneration (Cardoso et al., 2020). Furthermore, inhibition of malonyl-CoA decarboxylase (MCD), which mediates malonyl-CoA degradation, increases levels of Malonyl-CoA, thereby inhibiting the enzymatic activity of CPT1, required for fatty acids transportation into mitochondria. As a consequence, glucose oxidation is increased and heart function after ischemia is improved (Stanley et al., 2005a). Restricted dietary fatty acid availability prolongs proliferation of CMs in young and adult hearts (Cardoso et al., 2020). Therefore, restriction of fatty acids uptake and oxidation may benefit the heart in response to pathological challenges.

2.2 Metabolic adaptation during heart regeneration and remodeling

The Randle cycle (also known as the glucose fatty-acid cycle), a biochemical mechanism involving the competition between glucose and fatty acids for oxidation and uptake, plays an important role in the cardiac metabolism (Randle et al., 1963). ATP consumed by the myosin ATPase (60%-70%), Ca^{2+}, and Na^{+}/K^{+} transporter (30%-40%) is mainly generated by fatty acid oxidation and oxidative phosphorylation (60% to 90%) under physiological condition (Bertero and Maack, 2018). However, the adaptive/maladaptive energy metabolism is characterized by impaired fatty acid utilization and reduced ATP production, which declines as much as 40% under pathological conditions (Fig5 A) (Bertero and Maack, 2018; Wilcox et al., 2015).

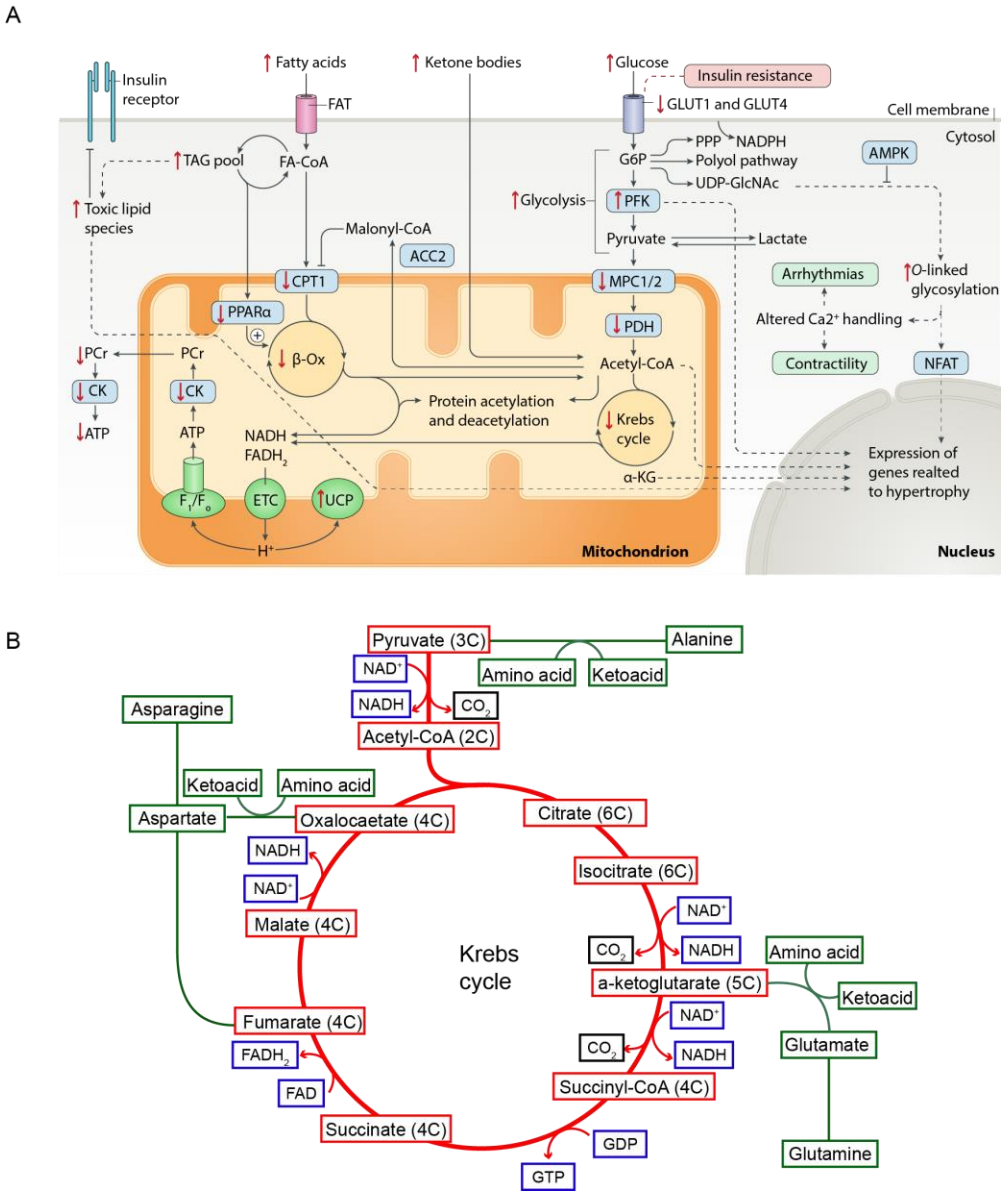

Fig5. Metabolic and transcriptional rewiring in cardiac remodeling.

(A) The red arrow indicates the transcriptional and metabolic rebalance in CM of cardiac remodeling (Bertero and Maack, 2018). **(B)** Amino acids and TCA cycle (Drake et al., 2012).

Elevated uptake of glucose and a high rate of glycolysis are hallmarks for metabolic remodeling in CMs. During compensatory cardiac hypertrophy, glucose oxidation tends to be elevated. Conditional ablation of mitochondria pyruvate carriers (MPC1 or MPC2) in CMs, dramatically reduces glucose oxidation, impairs myocardial function, and induces pathological cardiac remodeling. Interestingly, the reduced glucose oxidation does not induce significant differences of intermediate metabolites within the TCA cycle (Fernandez-Caggiano et al., 2020; Zhang et al., 2020). This observation might be

attributed to compensatory processes by channeling pyruvate into the TCA cycle in an Acetyl-CoA independent manner (anaplerosis) (Lydell et al., 2002; Sorokina et al., 2007). Elevated anaplerosis indicates a mismatch between up-regulated glycolysis and unchanged glucose oxidation rate found in the cardiac remodeling process via pyruvate carboxylation (Davila-Roman et al., 2002). To cope with the high demand for amino acids and nuclear acids during cardiac hypertrophy, pyruvate anaplerosis may provide precursors by producing intermediate metabolites within the TCA cycle at the expense of ATP production (Doenst et al., 2013). However, the oxidation rate of glucose does not show a dramatic difference at a late stage of cardiac remodeling when systolic dysfunction occurs (Doenst et al., 2010; Kolwicz et al., 2013; Pound et al., 2009). This mismatch might occur due to reduced pyruvate oxidation within mitochondria (Atherton et al., 2011). In the late stage of pathological remodeling, insulin insensitivity will further reduce ATP production from glucose oxidation. Therefore, the shift towards glucose oxidation for energy production only transiently compensates for reduced ATP production within a limited time window (Swan et al., 1997).

Fatty acid uptake and utilization under pathological conditions is a matter of debate. There is evidence for decreased glucose but increased FAO uptake, resulting from elevated serum levels of fatty acids in the animals with failing hearts. On the other hand, expression of a truncated inhibitory isoform of PPARγ has been reported in failing heart, which reduces transcription of enzymes for fatty acids uptake and utilization (Goikoetxea et al., 2006; Sack et al., 1996), Enforced uptake of fatty acid by CMs further causes accumulation of intracellular lipids, which contribute to lipotoxicity and CM apoptosis (Opie and Knuuti, 2009; Sharma et al., 2004). Hyperglycemia blocks uptake of glucose and combined with accumulation of free fatty acids stimulates the inflammatory system, which increases insulin resistance, accelerating progression of heart failure (Goldberg et al., 2012). These findings suggest that the metabolism of fatty acids in heart failure shows a stage-specific pattern, and depends strongly on the specific model.

Although pyruvate serves as one of the major substrates for energy production (10%-40%) in response to excessive workload in the ischemic heart (Stanley et al., 2005b), ketone bodies, d-β- soluble 4-carbon compounds, principally derived from fatty acids, also contribute to ATP production under prolonged fasting conditions and in failing hearts (Taegtmeyer et al., 2004). Moreover, amino acid metabolism is of particular importance in the diseased heart under conditions mitigating oxidation, *i.e.*, ischemia, anoxia, and many types of cardiomyopathy, in which fatty acid oxidation is inhibited. Decreased levels of TCA intermediates under unfavorable oxidation conditions can be supplemented by amino acid

catabolism, thereby prolonging cellular function during anoxia. For instance, glutamate and glutamine can be converted to α-ketoglutarate (αKG), a Krebs cycle intermediate (Fig5 B) (Drake et al., 2012; Peuhkurinen et al., 1983). Other amino acids, such as asparagine and aspartate, may also be important due to their ability to transfer amine groups to excess TCA intermediates downstream of succinate (Fig5 B) (Drake et al., 2012). The ability to produce ATP directly from glutamine and glutamate through substrate-level phosphorylation makes these amino acids important for ischemic and hypertrophied hearts when CMs begin to suffer from free radicals and low pH (Drake et al., 2012). In this context, it is important to note that amino acid metabolism may have several significant functions and provides protection against ischemia and anoxia, it is not sufficient to meet the energy demand of hearts for extended periods. Nevertheless, amino acids will extend the length of time between the onset of ischemia and the point of irreversible cardiac damage.

3. Epigenetics in heart remodeling and regeneration

Epigenetic mechanisms are central to sustain cell-specific gene expression, thereby controlling cell/tissue homeostasis including cell proliferation, differentiation, senescence, and apoptosis. Alterations of the epigenetic landscape might lead to developmental defects and diseases including cardiovascular disorders. During the last decades, emerging evidence revealed that multiple diverse epigenetic processes, including DNA methylation and histone modifications, affect the transcriptional programs in CM, regulating proliferation, differentiation and maturation. Obviously, this has strong effects on heart development, regeneration and remodeling.

3.1 DNA methylation in heart regeneration and remodeling

Methylation of the fifth carbon of cytosine (5-methylcytosine, 5mC) within CpG dinucleotides was first reported in 1975 (Holliday and Pugh, 1975; Riggs, 1975). DNA methylation is accomplished by the DNA methyltransferase (DNMT) family of enzymes catalyzing the transfer of a methyl group to DNA using S-adenosyl-methionine (SAM) as methyl donor. Among the known DNMTs, DNMT1 is responsible for maintenance of DNA methylation, which ensures fidelity of replication of inherited epigenetic patterns. In contrast DNMT3A and DNMT3B serve to establish *de novo* DNA methylation (Greenberg and Bourc'his, 2019; Okano et al., 1999; Okano et al., 1998). In the mammalian genome, 70-80% of the CpG regions are methylated. When located in a gene promoter, DNA methylation functions typically as a repressive marker for transcription (Li and Zhang, 2014). Although DNA methylation is chemically and genetically stable, it can be actively erased under several conditions such

as cell differentiation and during pathological processes. For active DNA demethylation, ten-eleven translocation methylcytosine dioxygenases (TET) progressively convert 5mC to 5-hydroxymethylcytosine (5hmC), 5-formylcytosine (5fC), and 5-carboxylcytosine (5caC) (Ito et al., 2010; Ito et al., 2011; Tahiliani et al., 2009). Complete DNA demethylation is eventually achieved by converting 5caC and 5fC to unmodified cytosine via activity of the thymine DNA glycosylase (TDG) coupled with the base excision DNA repair machinery (He et al., 2011).

The global level of 5mC dramatically decreases during postnatal CM maturation (Creco et al., 2016). Simultaneously, the expression of *Dnmt1*, the enzyme responsible for DNA methylation maintenance, is down-regulated with age (Wu et al., 2020). Postnatal demethylation within bodies of gene involved in maturation and function of CMs correlates strongly with increased gene expression (Gilsbach et al., 2014). In the adult stage, a subset of demethylated genes such as fetal cardiac genes and cell cycle regulators are repressed by the polycomb mark H3K27me3 or by DNA methylation. For instance, *de novo* DNA methylation by DNMT 3A/B causes repression of essential components of the fetal cardiac sarcomere (Gilsbach et al., 2014). Surprisingly, under pathological conditions, failing CMs generate a neonatal methylation pattern, although differentially methylated regions are prominent in intergenic regions (Gilsbach et al., 2014; Gilsbach et al., 2018). Interestingly, expression of *Dnmt1* is up-regulated in diseased hearts, suggesting that generation of a fetal methylation pattern and reprogramming of gene expression are adaptive responses following pathological stimuli (Wu et al., 2020). However, the function of DNMT3A and DNMT3B is dispensable under pathological conditions (Gilsbach et al., 2014; Madsen et al., 2020; Nuhrenberg et al., 2015).

The absolute level of 5hmC also drops dramatically from fetal/neonatal to adult stages (Greco et al., 2016). Moreover, in the neonatal stage, 5hmC is widely distributed over the whole genome, but becomes enriched on gene bodies of highly expressed genes in the adult stage (Greco et al., 2016). Compared to *Tet1*, which is primarily expressed at early embryonic development stages, *Tet2* and *Tet3* are expressed at a relatively high level in adult CMs (Dawlaty et al., 2011; Giudice et al., 2014; Greco et al., 2016). Cardiac-specific *Tet2* ablation did not show dramatic phenotypical changes, probably due to the compensation by *Tet3* (Greco et al., 2016). Notably, *Tet3* deficient embryonic stem cell (ESC) showed enhanced differentiation towards cardiac mesoderm instead of neuroectoderm, probably by activation of the Wnt signaling pathway *in vitro* (Li et al., 2016). Impressively, double knockout of *Tet2* and *Tet3* in cardiac progenitor cells with Nkx 2.5 Cre induces ventricular non-compaction cardiomyopathy characterized by reduced thickness of the ventricular wall and increased trabecular

areas starting from E13.5 (Fang et al., 2019). Mechanistically, the loss of 5hmC counteracts YY1 binding and disrupts promoter and enhancer looping of cardiac-specific genes (Fang et al., 2019).

3.2 Histone methylation in heart regeneration and remodeling

Histone proteins, fundamental components of the nucleosome, undergo post-translational modification (PTM), including methylation, acetylation, phosphorylation, sumoylation, ADP ribosylation, and biotinylation at the distinct amino acid residues at the histone core or at the tails. Such PTMs regulate gene expression by altering chromatin structure by modulating histone-DNA interactions or recruiting chromatin modifiers (Margueron and Reinberg, 2010). In particular, the function of histone lysine methylation in cardiac regeneration and remodeling has been well studied.

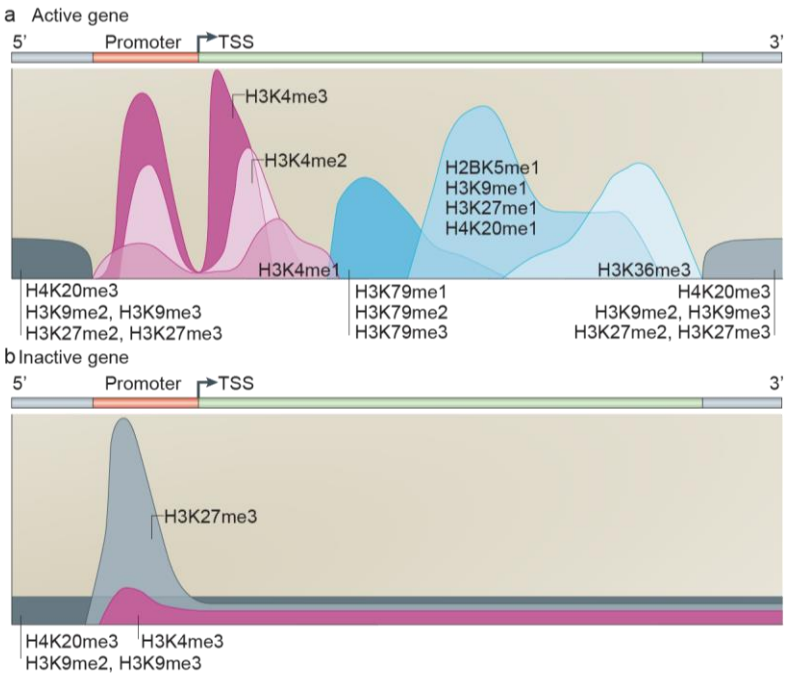

Fig6. Distribution of histone methylation markers on transcriptionally active genes (a) and inactive genes (b) (Kooistra and Helin, 2012).

Histone lysine methylation is a process that transfers methyl groups to various lysine residues of histone proteins. Depending on the degree of methylation and the location of the methylated residue, different functional outcomes occur (Fig.6 a&b) (Kooistra and Helin, 2012). Histone lysine methylation is a reversible process, as methyl marks can be removed by specific enzymes. Among the different histone lysine methylations, methylations on lysine 9, 27 in histone H3 tail, and on lysine 20 in histone H4 tail are primarily correlated to inhibition of transcription by instructing formation of

repressive chromatin structures. In contrast, methylation of H3K4, H3K36, and H3K79 is related to transcriptional activation. In particular, H3K4me3, which is methylated by the KMT2 family (KMT2A to KMT2F) and can be erased by the KDM5 demethylase family (KDM5A to KDM5D), KDM2B, and RIOX1, is an extensively studied histone modification (Kooistra and Helin, 2012). H3K4me3 is usually symmetrically distributed within approximately 1-kilobase around the transcription start site (TSS) of actively transcribed genes and promote gene transcription by directing assembly of the preinitiation complex through interaction with different effector proteins. Recent work has identified a small subset of genes exhibiting an H3K4me3 distribution extending further downstream into the gene body, although the majority of H3K4me3 is found with restricted width near the TSS of actively transcribed genes (Benayoun et al., 2014). Interestingly, the broad deposition of H3K4me3 is found in genes associated with cell identity in various species and cell types including CM, indicating a broad localization of H3K4me3 is a novel but evolutionarily conserved epigenetic signature (Chen et al., 2015; Dhar et al., 2018). Another recent work demonstrated that the MLL2/COMPASS establishes H3K4me3 with narrow breadth in mESC, while SET1A-B/COMPASS is responsible for broad H3K4me3 domains (Sze et al., 2020). However, the exact role of broad H3K4me3 domains has not yet been determined unambiguously. H3K4me3 broad domains have been proposed to function as "buffering" against spurious bursts of transcription without affecting the transcriptional output (Benayoun et al., 2014). However, other studies demonstrated a significant positive correlation of H3K4me3 breadth with gene expression level in both ESCs and terminally differentiated cells, which might be facilitated by release of poised RNA Pol II resulting in increased elongation rates (Chen et al., 2015; Sze et al., 2020). Interestingly, in pre-implantation embryos, the breadth of broad H3K4me3 domains that preferentially mark highly transcribed key cell identity/function genes changes gradually during developmental and is highly resistant to repressive H3K27me3. This finding suggests that inherited broad H3K4me3 and acquisition of specific broad H3K4me3 during differentiation protect transcription from occasional transient change to secure transcriptional stability in defined cell types (Liu et al., 2016b). In mammals, H3K4 methylation is mediated by the KMT2 family composed of six members, which operate in a complex called COMPASS (Complex of Proteins Associated with Set1) (Fig7 A&B). KMT2B (MLL2) is required for cardiac lineage specification in the ESC differentiation model by mediating H3K4me3 deposition on promoters of cardiac-specific genes (*Nkx 2.5*, *Gata4,* and *Tbx5*) (Wan et al., 2014). KMT2C is up-regulated in pathological hypertrophy induced by TAC, together with elevation of H3K4me2 (Jiang et al., 2017). Alterations of the distribution of H3K4me1 and H3K4me2 on enhancer and promoter regions of cell cycle and hypoxia-reoxygenation-related

genes by inactivation of KMT2D in cardiac progenitor cells leads to disrupted heart development with reduced CM proliferation (Ang et al., 2016). Humans have six H3K4 demethylases: KDM2B, RIOX1, and the KDM5 family, in which KDM5A, KDM5B, KDM5C, and KDM5D remove methyl groups from either H3K4me3 or H3K4me2. KDM5B mainly regulates H3K4me3 deposition on promoter regions, and KDM5B ablation in cardiac progenitor cell (Nkx2.5 Cre) leads to congenital heart defects by changing the balance between *Nkx2.5* and *Isl1* expression (Cho et al., 2018; Kidder et al., 2014; Lee et al., 2000). Interestingly, KDM5C is located on the X chromosome, and KDM5D is located on the Y chromosome; KDM5D down-regulation blocks CM differentiation from ESC in the embryonic body *in vitro*. Moreover, double mutations of KDM5C and KDM5D lead to non-compaction cardiomyopathy (Kosugi et al., 2020; Meyfour et al., 2019).

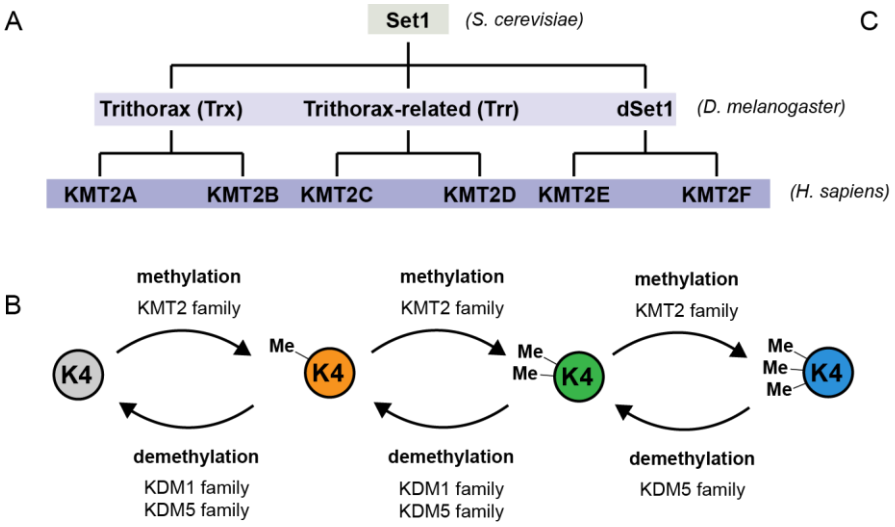

C

ENZYME	ALTERNATIVE NAME(S)
KMT2A	MLL1, MLL, ALL1
KMT2B	MLL2, MLL4, WBP7
KMT2C	MLL3
KMT2D	MLL4, MLL2, ALR
KMT2E	hSET1A
KMT2F	hSET1B
KDM1A	LSD1, BHC110
KDM1B	LSD2, AOF1
KDM5A	JARID1A, RBP2
KDM5B	JARID1B, PLU-1
KDM5C	JARID1C, SMCX
KDM5D	JARID1D, SMCY

Fig7. Enzymology of H3K4 methylation and demethylation (modified from (Collins et al., 2019))

(A) Evolutionary tree diagram of H3K4 methyltransferase (B) Diagram of H3K4 methylation and demethylation pathway (C) Enzymes for H3K4 methylation and demethylation.

Similar to H3K4 methylation, formation of H3K36me3 by SETD2 is tightly associated with active transcription. However, H3K36me3 is mainly enriched within bodies of active genes and is involved in reestablishing repressive chromatin structures, in part via recruitment of chromatin modifiers after the passage of elongating Pol II, thereby precluding spurious transcript initiation within the body of active genes (Neri et al., 2017). H3K79me2, which is important for the early phase of transcriptional elongation, shows strong signals at H3K4me3 broad domains relative to non-broad domains (Chen et al., 2015b). H3K79 is methylated by DOT1 and DOT1L, while the corresponding demethylase has

not been identified so far (Michalak et al., 2019). DOT1L is highly expressed in the fetal/neonatal CMs but drops down dramatically in the adult stage. Functionally, DOT1L facilities cardiac differentiation by promoting the expression of cardiac-specific genes e.g. *Gata4*, *Nkx2.5*, *Myh6*, *Myh7* (Cattaneo et al., 2016). The ablation of *Dot1l* in CM leads to cardiac dilation by reducing *Dmd* (Dystrophin) transcription, leading to dysfunctions of the Dystrophin-glycoprotein complex, which is important for viability of CMs (Nguyen et al., 2011).

3.3 Histone acetylation in heart regeneration and remodeling

Histone lysine acetylation is a reversible process that transfers an acetyl group from acetyl-coenzyme A (Acetyl-CoA) to the NH_3^+ group on lysine within the N-terminal tail protruding from the histone core of the nucleosome. Acetylation is catalyzed by lysine acetyltransferases (KATs); the deacetylation is mediated by lysine deacetylases (KDACs), which include HDACs and Sirtuins (Graff and Tsai, 2013). Acetylation removes the positive charge on the histones, thereby decreasing the interaction of the N terminal of histones with the negatively charged phosphate groups of DNA. As a consequence, condensed chromatin is transformed into a more relaxed structure, associated with higher levels of gene transcription. Thus, histone acetylation and deacetylation are essential parts of gene regulation. Both KATs and HDACs play vital roles in regulating cardiac remodeling and repair. For instance, p300 and CBP activities are activated in phenylephrine-induced cardiac hypertrophy (Gusterson et al., 2002; Gusterson et al., 2003). Overexpression of *p300* stimulates cardiac hypertrophic growth, whereas the dominant-negative mutation inhibits PE-induced cardiac hypertrophy (Yanazume et al., 2003a; Yanazume et al., 2003b). HDAC2 reduces histone acetylation at the promoter of the *Tagln* gene and promotes progression of cardiac remodeling (Kook et al., 2003). Overexpression of HDAC3 in mice led to CM hyperplasia but not hypertrophic growth by inhibiting several cyclin kinase inhibitors (Trivedi et al., 2008).

4. The interplay between metabolism and epigenetics

The activity of chromatin-modifying enzymes relies on the availability of various intermediate metabolites such as NAD, αKG, or Acetyl-CoA among others, which provide the chemical moieties for posttranslational modification of DNA and histone (Fig8). Therefore, changes of the cardiac metabolic state during adaptive/maladaptive responses during heart development, remodeling, and regeneration have the potential to affect modifications of chromatin in ways that change gene expression.

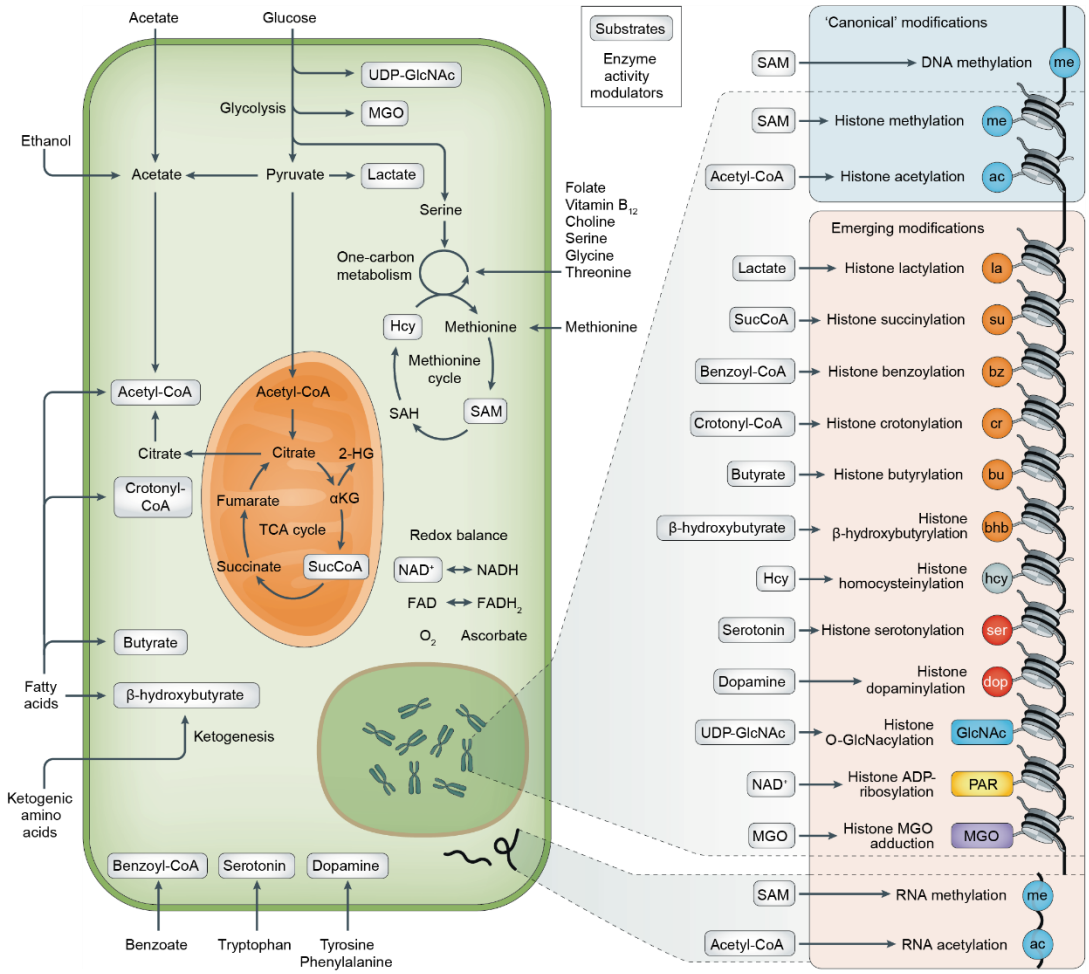

Fig8. The interplay between metabolism and epigenetics (Dai et al., 2020).

4.1 αKG and 2HG modulates the enzymatic activity of αKG-dependent DNA/histone demethylases

αKG is a key intermediate in the TCA cycle produced by the Isocitrate dehydrogenase (IDH) complex that catalyzes oxidative decarboxylation of isocitrate in both mitochondria and the cytoplasm. The oxoglutarate dehydrogenase complex (OGDH) further converts αKG to succinyl-CoA, NADH, and CO_2 within the TCA cycle. In addition, αKG can be derived from amino acids (Glutamate and Glutamine) by Glutamate dehydrogenase (GDH) in mitochondria or by transamination in the cytoplasm and mitochondria (Xiao et al., 2016). αKG serves as an essential cofactor for TETs and Jumonji-C (JmjC) domain-containing histone demethylases, although it remains unknown where/how nuclear αKG is produced. Since several TCA cycle enzymes e. g. PDH, ACO, IDH have been reported to translocate into the nucleus, it is likely that nuclear αKG is produced locally rather than freely diffuses from the cytoplasm through the nuclear pore (Nagaraj et al., 2017). It was estimated that the

αKG concentration varies from 0.5 to 3 mM in the proliferating cell, which is above the Km of most αKG-dependent demethylase (Chowdhury et al., 2011; Thirstrup et al., 2011). Notably, αKG-dependent enzymes can be inhibited by the oncometabolite, 2-hydroxyglutarate (2HG), a structural homolog of αKG produced by gain-of-function mutation of IDH1 (R132H) or IDH2 (R140Q, R172K) (Su et al., 2018). Intracellular αKG plays a vital role in the regulation of cellular homeostasis. For instance, enhanced αKG levels facilitate differentiation of primed pluripotent stem cells and tumor cells by inducing H3K4 hypomethylation (TeSlaa et al., 2016; Tran et al., 2020). Similarly, accumulation of 2HG has been shown to promote tumor cell proliferation and block tumor cell differentiation (Jezek, 2020). In the mouse, enhanced levels of circulating αKG after suppression of EGLN1 protects the heart from ischemic damage due to remote ischemic preconditioning (Olenchock et al., 2016). Additionally, αKG binds to the sarcolemma-localized oxoglutarate receptor OXGR1. Ablation of *Oxgr1* exacerbates pathological cardiac remodeling induced by TAC surgery due to enhanced activity of the pro-hypertrophic STAT3 pathway (Omede et al., 2016). These findings indicate the beneficial effect of αKG on cardiac tissue homeostasis, although the effects of αKG on epigenetic processes has not been determined. In contrast, increased concentrations of 2HG, produced by IDH2 mutant leukemic cells, cause contractile dysfunction in the heart by impairing αKG-dependent enzyme activity, leading to the globally increased H3K9me3 levels (Karlstaedt et al., 2016).

4.2 Succinate and fumarate regulate histone and DNA methylation

Both succinate and fumarate are endogenous inhibitors of αKG-dependent enzymes (Dai et al., 2020). Mutations of Succinate dehydrogenase (SDH) or Fumarate hydratase (FH) are frequently found in various cancer types, leading to aberrant accumulation of succinate or fumarate, respectively (King et al., 2006). Accumulation of oncometabolites such as succinate or fumarate may inhibit the DNA repair machinery by blocking transient demethylation of H3K9me3 at the DNA double-strand breaks (Sulkowski et al., 2020). Similar to IDH mutations, excessive accumulation of succinate and fumarate in leukemia cells leads to DNA hypermethylation by inhibiting αKG-dependent enzymatic activity of TETs (Figueroa et al., 2010; Xiao et al., 2012). Elevated level of fumarate generated locally in the nucleus specifically inhibits KDM2B-mediated H3K36me2 and enhances DNA damage repair (Jiang et al., 2015).

4.3 The ratio of SAM/SAH affects histone and DNA methylation

Both DNA and histone methyltransferase utilize SAM as substrate to catalyze cytosine, lysine, or arginine methylation. SAM is a conjugate of methionine at the sulfur atom with adenosine derived

from ATP, a reaction catalyzed by methionine adenosyltransferase (MAT). This process is reversible by converting SAM into S-adenosylhomocysteine (SAH). Since SAH inhibits the enzymatic activity of DNMT and KMT, the SAM/SAH ratio determines the methyltransferase activity in the mammalian cell (Mentch et al., 2015). The SAM/SAH ratio is significantly reduced in human patients with cardiovascular disease. Therefore, SAH levels in the plasma might serve as a biomarker for cardiovascular diseases (Huang et al., 2017). Glycine N-methyltransferase deficient mice show a high incidence of carcinoma and SAM levels are upregulated around 40-fold, leading to DNA hypermethylation at promoters of tumor suppressor genes and subsequent gene silencing (Martinez-Chantar et al., 2008).

4.4 Acetyl-CoA is the sole donor of the acetyl group for histone acetylation

In many mammalian cell, acetyl-CoA is primarily derived from oxidation of glucose. However, in adult CM, acetyl-CoA is dominantly produced via oxidation of fatty acids (Dai et al., 2020; Doenst et al., 2013). Citrate can be converted to acetyl-CoA by the ATP-citrate lyase (ACL) within the cytosol and nucleus (Fernandez et al., 2019). Moreover, Acetyl-CoA can also be generated from acetate by the acetyl-CoA synthetase 2 (ACSS2) in nuclei (Zlotorynski, 2017). It seems possible that citrate is used to generate acetyl-CoA in the nucleus after synthesis of citrate from acetyl-CoA in mitochondria, although other alternatives exist. It has been reported that the Pyruvate dehydrogenase (PDH) complex translocates into the nucleus, where it catalyzes conversion of pyruvate to Acetyl-CoA, facilitating histone acetylation (de Boer and Houten, 2014). Of note, the rate of Acetyl-CoA synthesis during glucose oxidation correlates with approximately half of the histone acetylation (Cluntun et al., 2015). Reduction of cytosolic Acetyl-CoA production by inhibiting ACL results in markedly impaired histone acetylation (Wellen et al., 2009).

Objective

The metabolism of CM switches from glycolysis to fatty acid oxidation (FAO) shortly after birth. In failing or regenerating CMs energy metabolism shifts back to glycolysis accompanied by reactivation of fetal cardiac genes. Changes in the metabolic state of CM during development and disease have the potential to alter the chromatin to either suppress or activate genes, leading to profound structural and functional changes. A direct assessment of the interplay between the metabolic state and epigenetic processes in regulating CM proliferation, maturation, and cardiac regeneration is still missing. In this study, I attempted to elucidate the impact of metabolic reprogramming after FAO inhibition on cardiac regeneration and remodeling and uncover the underlying epigenetic mechanisms. My eventual objective was to discover novel metabolic and/or epigenetic targets to enhance repair of cardiac injuries.

To achieve this aim, I have addressed the following issues:

(1) Investigation of the impact of FAO inhibition on CM proliferation and maturation *in vitro*.
(2) Assessment of the cardiac phenotype of different CPT1B knockout mouse lines under physiological and pathological conditions *in vivo*.
(3) Characterization of changes in metabolite production after FAO inhibition and assessment of potential compensatory pathways.
(4) Determination of epigenetic changes in response to metabolic reprograming after FAO inhibition.
(5) Identification of epigenetic modifiers that senses metabolic changes and change expression of target genes.
(6) Validation of the potential of putative metabolic and/or epigenetic targets to regulate CM proliferation and maturation *in vitro*.

Material and methods

Material

Table 1 Inhibitor & Chemicals

Inhibitor & Chemicals	Company	Catalog no.
(+)-Etomoxir (sodium salt)	Cayman	11969
Octyl-α-ketoglutarate	Cayman	11970
CPI-455 HCl	Selleckchem	S8287
(2R)-Octyl-α-hydroxyglutarate	Cayman	16366
Aprotinin	Sigma-Aldrich	10820
Leupeptin	Sigma-Aldrich	L8511-5MG
Sodium fluoride (NaF)	Sigma-Aldrich	S7920-100G
Sodium orthovanadate (Na_3Vo_4)	Sigma-Aldrich	450243
Pheylmethylsulfonyl fluoride (PMSF)	Sigma-Aldrich	P7626
Proteinase inhibitor cocktail	Merck	4693159001

Table 2 Drug for injection

Drug	Company	Catalog no.
Tamoxifen ≥ 99%	Sigma-Aldrich	T5648-5G
EdU (5-ethynyl-2'-deoxyuridine)	ThermoFisher Scientific	A10044

Table 3 Enzyme

Enzyme	Company	Catalog no.
Collagenase B	Sigma-Aldrich	11088815001
Proteinase K	Carl Roth	75282
SuperScript™ II Reverse	ThermoFisher Scientific	18064014

Taq Polymerase	Homemade	
Trypsin EDTA	ThermoFisher Scientific	R001100

Table 4 Chemicals

Chemicals	**Company**	**Catalog no.**
Agarose	Carl Roth	2267
Ammonium persulfate (APS)	Serva	3375
Benzonase® Nuclease	Merck	E1014-25KU
Bis-Tris	AppliChem	A10250500
Bovine serum albumi (BSA)	ThermoFisher Scientific	BP1605
Calcium Chloride x $2H_2O$	Carl Roth	52392
DAPI ((4', 6-diamidino-2-phenylindole)	ThermoFisher Scientific	D1306
Dimethyl sulfoxide (DMSO)	Sigma-Aldrich	D-4540
Disodium hydrogen phosphate (Na_2HPO_4)	Merck	65800500
1,4-Dithiothreit (DTT)	Carl Roth	69082
EDTA	Carl Roth	80403
EGTA	Carl Roth	E3889
Eosin Y solution, aqueous	Waldeck	2C-140
Ethanol (100%)	Carl Roth	90654
Ethidium bromide solution (1%)	AppliChem	A11520100
FSC 22 Frozen Section Compound	Leica	75806-668
Fetal calf serum (FCS)	Sigma-Aldrich	F2442
Glycerin (87%)	Merck	1040942500
Glycine	Sigma-Aldrich	15527

Glycogen for mol.biol.	Roche	10901393001
Hematoxylin solution modified	Merck	1.05174.0500
HEPES	Carl Roth	91053
Hydrochloric acid (37%)	Carl Roth	46251
InstantBlue Protein Stain	Expedeon	ISB1L
Isopropanol	Carl Roth	67524
Magnesium chloride x $6H_2O$	Carl Roth	21891
Magnesium sulfate hetahydrate ($MgSO_4$ x $7H_2O$)	Merck	5886
Methanol	Carl Roth	46275
Mowiol 4-88	Merck	3186101
NP-40 (Tergitol-type NP-40)	Fluka	74385
Oligo 15 primer	Promega	C110A
Opti-MEM™ I Reduced Serum Medium	ThermoFisher Scientific	31985062
Paraformaldehyde	Carl Roth	03354
Penicillin-Streptomycin. (10,000 U/mL)	ThermoFisher Scientific	15140122
Phenylmethylsulfonyl fluoride (PMSF)	Sigma-Aldrich	P7626
Potassium chloride (KCl)	Carl Roth	67813
Potassium bicarbonate ($KHCO_3$)	Merck	1048540500
Potassium dihydrogen phosphate (KH_2PO_4)	Carl Roth	P0181
Protein A-Agarose	Roche	11134515001
Protein G-Agarose	Roche	11243233001
Rnase, Dnase - free	Roche	11119915001

RNaseZAP™	Sigma-Aldrich	SLBQ7780V
Red Alert™ 10x	Merck	71078-3
REDTaq® ReadyMix™ PCR Reaction Mix	Sigma-Aldrich	R2523-100RXN
Rnase inhibitor	Promega	N2515
SDS	Carl Roth	23263
Skim milk	Fluka	70166
Sodium azide (NaN_3)	Carl Roth	K3051
Sodium Bicarbonate ($NaHCO_3$)	Merck	1063290500
Sodium chloride (NaCl)	Carl Roth	39572
Sodium deoxycholate	Merck	1065040100
Surcose	Carl Roth	90971
2 x Taq Master Mix	Vazyme	P111/P112
TEMED	Carl Roth	23671
Tissue - Tek® O.C.T Polyfreeze TM freezing	Leica	3801480
Tris	Carl Roth	54292
Triton-X 100	Carl Roth	66831
TRIZOL® reagent	Invitrogen	15596018
TurboFect transfection reagent	ThermoFisher Scientific	R0531
Tween-20	Merck	8221840500
Xylol	Carl Roth	97133
Fibronectin Solution, bovine (1 mg/ml)	Promo Cell	C-43050

Table 5 Cell culture medium

Medium	Composition	Company
Growth medium for H293T	DMEM (Dulbecco's Modified Eagle Medium) with 4.5 g/L glucose, 10% fetal calf serum, 100 U/mL penicillin / streptomycin, 20mM glutamine	Sigma-Aldrich
Growth medium for primary neonatal CM	80% DMEM with 4.5 g/L glucose, 20% Medium 199; 5% FCS, 100 U/mL penicillin / streptomycin	Gibco
Growth medium for primary adult CM	M199 medium supplied with Creatinine (5mM), L-carnitine (2mM), Taurin (5mM), HEPES (25mM), 100 U/mL penicillin / streptomycin, FCS (5%), ITS supplement (1%)	

Table 6 Buffers

Buffer	Composition
10% APS	Dilute 10 g APS in 100 mL Aqua dest
5% BSA	Dilute 5 g BSA in 100 mL 1 x PBS-T
Electron Microscopy fixation buffer	1.5% glutaraldehyde; 1.5% paraformaldehyde in 0.15 mol L-1 HEPES
Immunofluorescence blocking buffer (general)	3% BSA in 1x PBS
5% Immunoblot blocking solution	Dilute 5 g skim milk in 100 mL 1 x PBS-T
10 x PBS, pH 7.4	Dilute 80 g NaCl; 2 g KCL; 14.4 g Na_2HPO_4; 2.4 g KH_2PO_4 in 800 mL Aqua dest.; adjust pH to 7.4; refill to 1000 mL with Aqua dest.
1 x PBS, pH 7.4	100 mL 10 x PBS + 900 mL Aqua dest
1 x PBS-T	1 x PBS + 0.1% Tween 20

SDS running buffer (10x)	250 mM Tris base, 1 % SDS, 1.9 M Glycine
ChIP dilution buffer	20 mM Tris-HCl, pH 8.0, 150 mM NaCl, 2 mM EDTA, 1% Triton X-100, complete protease inhibitor cocktail
High salt washing buffer for ChIP - qPCR	20 mM Tris-HCl, pH 8.0, 500 mM NaCl, 2 mM EDTA, 1% Triton X-100
LiCl washing buffer for ChIP - qPCR & ChIP - seq	10 mM Tris-HCl, pH 8.0, 250 mM LiCl, 1% Na-deoxycholate, 1% NP40
TE washing buffer for ChIP - qPCR & ChIP - seq	10 mM Tris-HCl pH 8.0, 1 mM EDTA
RIPA buffer for ChIP - seq	0.1% SDS, 0.1% Sodium deoxycholate, 1% Triton X-100, 1mM EDTA, 10mM Tris-HCl pH 8.1, 150mM NaCl
RIPA 500 buffer for ChIP - seq	0.1% SDS, 0.1% Sodium deoxycholate, 1% Triton X-100, 1mM EDTA, 10 mM Tris-HCl pH 8.1, 500 mM NaCl
Elution buffer for ChIP - seq	10 mM Tris-HCl pH 7.4, 5 mM EDTA, 300 mM NaCl, 0.5% SDS
Lysis buffer (200mM)	20mM Tris-HCL, pH 8.0, 200 mM NaCl, 1mM EDTA, 1mM EGTA, 1% Triton X-100
10% SDS	Dilute 10 g SDS in 100 mL Aqua dest
50 x TAE	Dilute 242 g Tris Base; 57.1 mL acetic acid; 100 mL 0.5 mol EDTA, pH 8.0 in 1000 mL Aqua dest.
20 x Transfer buffer	Dilute 163.2 g Bicine; 209.6 g Bis-Tris; 12 g EDTA in 1000 mL Aqua dest
1 x Transfer buffer	250 mL 20 x transfer buffer; 1000 mL methanol; 3750 mL Aqua dest
1 M Tris, pH 6.8	Dilute 12.1 g Tris in 80 mL Aqua dest; adjust pH to 6.8; refill to 100 mL with Aqua dest
1.5 M Tris, pH 8.8	Dilute 18.17 g Tris in 80 mL Aqua dest; adjust pH to 8.8; refill to 100 mL with Aqua dest

Lysis buffer for FACS	5mM $CaCl_2$, 3mM MgAc, 2mM EDTA, 0.5 mM EGTA, and 10mM Tris-HCl, pH8
Nuclei stain buffer	DPBS, 1% BSA, 0.2% NP40, 1mM EDTA
Calcium-free buffer for adult CM isolation	NaCl 113mM, KCl 4.7mM, KH_2PO_4 0.6mM, Na_2HPO_4 0.6mM, $MgSO_4$ 1.2mM, $NaHCO_3$ 12mM, $KHCO_3$ 10mM, HEPES 10mM, Taurin 30mM, Glucose 5.5mM, 2,3-Butanedionemonoxime 10mM
Enzyme Buffer for adult CM isolation	Calcium-free buffer supplied with Liberase DH 0.25mg/ml, Trypsin 0.14mg/ml, $CaCl_2$ 12.5uM
Stop Buffer for adult CM isolation	Enzyme Buffer supplied with 10% FCS and $CaCl_2$ 12.5uM

Table 7 Antibody

Antibody	**Use**	**Use Supplier**	**Cat. No.**
α-Actinin (Sarcomere)	IF	Sigma-Aldrich	A7811
Ki67	IF	Abcam	ab15580
cTnT-FITC	IF	Abcam	ab105439
pH3	IF	Millipore	06-570
Ccne1	WB	Abcam	ab7959
Cpt1b	WB	Proteintech	22170-1-AP
Pan actin	WB	Cell Signaling	4968
WGA, Alexa FluorTM 488	IF	ThermoFisher Scientific	W11261
PCM1	FACS	Sigma-Aldrich	HPA023374-100UL
PDH1a	WB	Proteintech	18068-1-AP
PDK4	WB	Proteintech	12949-1-AP
ACSS1	WB	Proteintech	17138-1-AP
ACSS2	WB	GeneTex	GTX30020

ACL	WB	Proteintech	18068-1-AP
IDH1	WB	Biorbyt	orb135710
IDH2	WB	ThermoFisher Scientific	MA5-17271
IDH3a	WB	Abcam	ab58641
OGDH	WB	Sigma-Aldrich	HPA020347-100UL
DLST	WB	Cell Signaling	5556
DLD	WB	ThermoFisher Scientific	PA5-27367
H3K4me1	WB	Abcam	ab8895
H3K4me2	WB	Active Motif	39141
H3K4me3	WB	Millipore	07-473
H3K9me1	WB	Abcam	ab8896
H3K9me2	WB	Abcam	ab1220
H3K9me3	WB	Abcam	ab8898
H3K27me3	WB	Millipore	07-449
H3K36me3	WB	Abcam	ab9050
H3K79me2	WB	Millipore	04-835
H3K79me3	WB	Abcam	ab2621
H4K20me1	WB	Abcam	ab9051
H4K20me2	WB	Abcam	ab9052
H4K20me3	WB	Abcam	ab9053
H3	WB	Abcam	ab1791
H3K4me3	ChIP-seq	Diagenode	C15410003-50
5hmC	DB, MeDIP	Active Motif	39769
5mC	DB	Eurogentec	81103
5fC	DB	Active Motif	61225

5caC	DB, MeDIP	Active Motif	61223
Goat anti-Mouse IgG (H+L) Alexa Fluor 488	IF, FACS	ThermoFisher Scientific	A28175
Goat anti-Rabbit IgG (H+L) Alexa Fluor 594	IF, FACS	ThermoFisher Scientific	A-11037

Table 8 Primers

Name	Primer sequence (5'-->3')	Application
Slc2a1 qF	CAGTTCGGCTATAACACTGGTG	qPCR
Slc2a1 qR	GCCCCCGACAGAGAAGATG	qPCR
Slc2a4 qF	GTGACTGGAACACTGGTCCTA	qPCR
Slc2a4 qR	CCAGCCACGTTGCATTGTAG	qPCR
Ldhb qF	CATTGCGTCCGTTGCAGATG	qPCR
Ldhb qR	GGAGGAACAAGCTCCCGTG	qPCR
Pfkm qF	TGTGGTCCGAGTTGGTATCTT	qPCR
Pfkm qF	GCACTTCCAATCACTGTGCC	qPCR
Cpt1a qF	CTCCGCCTGAGCCATGAAG	qPCR
Cpt1a qR	CACCAGTGATGATGCCATTCT	qPCR
Cpt1b qF	TCTAGGCAATGCCGTTCAC	qPCR
Cpt1b qR	GAGCACATGGGCACCATAC	qPCR
Acta1 qF	CCCAAAGCTAACCGGGAGAAG	qPCR
Acta1 qR	CCAGAATCCAACACGATGCC	qPCR
Nppa qF	GCTTCCAGGCCATATTGGAG	qPCR
Nppa qR	GGGGGCATGACCTCATCTT	qPCR
Nppb qF	GAGGTCACTCCTATCCTCTGG	qPCR

Nppb qR	GCCATTTCCTCCGACTTTTCTC	qPCR
Ldha qF	TGTCTCCAGCAAAGACTACTGT	qPCR
Ldha qR	GACTGTACTTGACAATGTTGGGA	qPCR
Atp2a2 qF	GAGAACGCTCACACAAAGACC	qPCR
Atp2a2 qR	CAATTCGTTGGAGCCCCAT	qPCR
Pln qF	AAAGTGCAATACCTCACTCGC	qPCR
Pln qR	GGCATTTCAATAGTGGAGGCTC	qPCR
Slc8a1 qF	CTTCCCTGTTTGTGCTCCTGT	qPCR
Slc8a1 qR	AGAAGCCCTTTATGTGGCAGTA	qPCR
Ryr2 qF	ACGGCGACCATCCACAAAG	qPCR
Ryr2 qR	AAAGTCTGTTGCCAAATCCTTCT	qPCR
Cacna1c qF	CCTGCTGGTGGTTAGCGTG	qPCR
Cacna1c qR	TCTGCCTCCGTCTGTTTAGAA	qPCR
Cacna2d1 qF	GTCACACTGGATTTTCTCGATGC	qPCR
Cacna2d1 qR	GGGTTTCTGAATATCTGGCCTGA	qPCR
Cpt1b flox F	GTGATGGCAATTATAGGCTAGTG	Genotyping
Cpt1b flox R	CTCCAGCCCCCAATCTCTAT	Genotyping
Cre F	GACCAGGTTCGTTCACTCATGG	Genotyping
Cre R	AGGCTAAGTGCCTTCTCTACAC	Genotyping

Plasmid

Table 9 Plasmid

Plasmid	Catalog no.	Company
pLJM1-KDM5B		Homemade
psPAX2	#12260	Addgene

pMD2.G	#12259	Addgene

Table 10 Kits

Kit	Company	Catalog no.
Click-iT™ EdU Cell Proliferation Kit for Imaging, Alexa Fluor™ 594 dye	ThermoFisher Scientific	C10339
Click-iT™ Plus EdU Alexa Fluor™ 647 Flow Cytometry Assay Kit	ThermoFisher Scientific	C10634
Trichrome stain (Masson) Kit	Sigma-Aldrich	HT15
LIVE/DEAD™ Viability/Cytotoxicity Kit, for mammalian cells	ThermoFisher Scientific	L3224
Click-iT™ Plus TUNEL Assay for In Situ Apoptosis Detection, Alexa Fluor™ 594 dye	ThermoFisher Scientific	C10618
Neonatal Cardiomyocyte Isolation Kit, mouse	MACS	130-100-825
Neonatal Heart Dissociation Kit, mouse and rat	MACS	130-098-373
A-KG Dehydrogenase Activity Assay Kit	Sigma-Aldrich	MAK189-1KT
Direct-zol Total RNA and small/miRNA from TRIzol without phase separation	Zymo Research	R2053
Dneay Blood & Tissue Kit	QIAGEN	69504
MinElute® PCR Purification Kit	QIAGEN	28004
truChIP Chromatin Shearing Kit with Formaldehyde	COVARIS	RK000958

Table 11 Equipment

Equipment	Company
Agarose gel electrophoresis chamber	Peqlab

Bio Doc analyzer	Bio RAD
ChemiDoc™ MP Imaging System	Bio RAD
Cold Plate for Tissue Embedding System	Leica
Eppendorftubes, 0.5 mL, 1.0 mL	Eppendorf
Filter tips 10 µL, 20 µL, 100 µL, 1000 µL	Fisher Scientific
Gelsystems (Mini, Maxi)	VWR
Greiner centrifuge tubes, 15 mL	Sigma-Aldrich
Greiner centrifuge tubes, 50 mL	Sigma-Aldrich
Keyence Fluorescence Microscope	Keyence
Nitrocellulose membranes	Invitrogen
StepOnePlus™ Real-Time PCR System	ThermoFisher SCIENTIFIC
SuperFrost Plus slides	Menzel-Glaeser
Tips 10 µL, 20 µL, 100 µL, 1000 µL	Greiner Bio-One
UV Transilluminator	INTAS
Xcell SureLock™ Mini-Cell and Xcell 11™ Blot Module	ThermoFisher SCIENTIFIC

Table 12 Software

Software	**Company**
Graph Pad Prism 6.0	Graph Pad Software
Image J / Fiji	NIH
Image Lab	Bio RAD
Adobe Phtoshop CS4	Adobe
Adobe Illustrator CS4	Adobe

Methods

Neonatal CM isolation and culture in vitro

The neonatal hearts were dissected from P0-1 C57bl/6 pups and washed with ice-cold PBS. After removal of atria, ventricles were pooled and primary CM isolation was performed according to manufacturer instruction (MACS, 130-100-825, 130-098-373). The variability of isolated CMs was checked by Trypan Blue staining (ThermoFisher, 15250061). Neonatal CMs were seeded in fibronectin pre-coated culture surfaces (0.8-1 million per 3.5 dish or 0.25 to 0.4 million per well of 2-well chamber slides) and cultured in primary neonatal CM culture medium (80% DMEM with 4.5 g/L glucose, 20% Medium 199; 5% FCS, 100 U/mL penicillin/streptomycin). After overnight culture, the chemicals were added into the medium and the neonatal CMs were further cultured for 72 to 96 hours before harvest. The chemical concentrations are listed as follows: Etomoxir 100μM (Cayman, 11969); αKG 500μM (Cayman, 11970); CPI-HCl 25μM (Selleckchem, S8287); R2HG 500μM (Cayman, 16366). The neonatal CMs were cultured with chemicals for 72 to 96 hours and harvested for further analysis.

Immunohistochemistry, Immunofluorescence, and histological analysis.

The heart was dissected and immediately fixed in 4% PFA. For paraffin sections, samples were dehydrated following standard protocols, embedded into paraffin, sectioned at 8 μm for immunofluorescence (IF) staining, hematoxylin/eosin (H&E) staining, or trichrome staining using established techniques. *In vitro* cultured neonatal CMs were fixed with 4% PFA for 10min in room temperature and permeabilized (0.3% Triton X-100 and 5% BSA) for 1 hour under room temperature. Microscopic images were acquired with a fluorescent stereomicroscope (Leica M205 FA). IF images were acquired with a fluorescent microscope (ZEISS Imager Z1). Histological image acquisition was performed with a light microscope (ZEISS Axioplan2). Antibodies for immunofluorescence staining are listed in Table 7.

EdU incorporation assay

EdU and other reagents were prepared according to the manufacturer's instruction (ThermoFisher C10339). The in vivo EdU incorporation assay was done according to a previous publication (Richardson, 2016). To analyze EdU incorporation in cultured neonatal CMs, cells in 2-well chamber slides were labeled with 10 μM EdU for 12 hrs. After two times washes with pre-warmed PBS, cells were fixed with 4% PFA for 10min at room temperature and EdU incorporation was visualized using the Click-iT EdU kit (Invitrogen) according to the manufacturer's protocol.

Western blot and Dot blot assays

Freshly isolated or cultured cells were washed with ice-cold PBS and lysed in cell lysis buffer (20 mM Tris (pH 7.5), 400 mM NaCl, 1 mM EDTA, 1 mM EGTA, 1% Triton X-100, 1x Complete Protease Inhibitor Cocktail (Roche Diagnostics) for 10 min on ice, followed by sonication with Bioruptor (Dianagene) at 4°C for 5 min. Proteins were separated by SDS-PAGE and transferred to nitrocellulose membranes (Millipore, Billerica, MA). Dot blot assays were performed with 100ng genomic DNA using a Bio-Dot Microfiltration apparatus (catalog No. 170-6545 and No. 170-6547). Proteins or DNA detected by antibodies were visualized using an enhanced chemiluminescence detection system (GE Healthcare) and quantified using the ChemiDoc gel documentation system (Bio-Rad). Antibodies used in this study are listed in Table 7.

Animals

Cpt1b$^{fl/fl}$ mice were generated in-house by using a targeting vector purchased from the European Conditional Mouse Mutagenesis Program (EUCOMM), in which exons 10-11 of the *Cpt1b* gene are flanked by two *LoxP* sites. αMHC-Cre$^{Pos/+}$ and αMHC-MCM$^{pos/+}$ mice were obtained from The Jackson Laboratory. C57bl/6 mice were obtained from Charles River. All mouse strains were backcrossed and maintained on a C57bl/6 genetic background. Primers used for genotyping are listed in Table 8. Tamoxifen (Sigma) was administered intraperitoneally at 75mg/kg body weight daily for 10 days. All animal experiments were done in accordance with the Guide for the Care and Use of Laboratory Animals published by the US National Institute of Health (NIH Publication No. 85-23, revised 1996) and according to the regulations issued by the Committee for Animal Rights Protection of the State of Hessen (Regierungspraesidium Darmstadt, Wilhelminenstr. 1-3, 64283 Darmstadt, Germany) with the project number B2/1137, B2/1125.

Genotyping

To perform mouse genotyping, tail biopsies were first digested in 200 µl tail lysis buffer (NID buffer) supplemented with 3 µl Proteinase K (20 mg mL^{-1}). After incubation overnight at 56 °C with 1000 rpm shaking, digested tail DNA samples were incubated at 95 °C for 10 min to inactivate Proteinase K. Genotyping PCRs were performed with self-designed primers as indicated in Table 8 using appropriate cycling conditions.

The master mix for one PCR reaction was prepared as followed:

Reaction mixture with commercial Taq polymerase:	
Taq mix (2 x Taq Master Mix)	5
ddH_2O	3.5
Primer 1 (forward)	0.5
Primer 2 (reverse)	0.5
Genomic DNA	1

PCR products were loaded on 2 % agarose gel, and ran for 30 min at 150-200 V. Double-stranded DNA was visualized under UV light and gels imaging was done by using Bio Doc analyzer.

Adult CM isolation and culture *in vitro*

Isolation of adult CM was performed as described previously (O'Connell et al., 2007). In brief, dissected hearts were cannulated via the aorta and arrested by retrograde perfusion with calcium-free buffer. Cannulated hearts were enzymatically digested by perfusion with enzyme buffer solution and cut off from the cannula. Atria were separated, and ventricles were minced in Enzyme Buffer. After gentle pipetting, myocytes were centrifuged at 500 rpm for 1 min and cell pellets, containing the CM fraction, were re-suspended in Stop Buffer. The calcium content of the cell suspension was then stepwise adjusted to 1 mM and CM-containing cell pellets were re-suspended in M199 cell culture medium, supplemented with creatinine, L-carnitine, HEPES, penicillin/streptavidin, 5% FCS, and insulin-transferrin-sodium selenite media supplement. Cells were seeded in Laminin pre-coated dishes and maintained at 37°C and 5 % CO2. To determine the CM number in the adult heart, the dissected heart was washed with ice-cold PBS and fixed with 1% PFA overnight. After washing with ice-cold PBS, the heart was cut into 1-2mm^3 pieces and incubated with digestion buffer (PBS containing 0.5U/mL collagenase B (Roche #11088807001) and 0.2% NaN_3) with oscillation at 1000 rpm at 37 °C. Every 12-24 hours, the digested CM was collected, and a new digestion buffer was added until the heart was fully dissolved. The CMs were pooled, plated into xx and the rod shape adult CM was counted under microscope.

Heart weight and body weight measurement with anesthesia

The adult mice were sacrificed under anesthetized condition with ketamine and xylazine. The body weight was measured individually. Then the adult heart was dissected and washed with ice-cold PBS.

The aorta and other connective tissue were completely removed under the microscope. The blood was washed out by PBS and the heart weight was measured after the heart was dried on the paper tissue.

MRI and data processing

Cardiac MRI measurements were performed on a 7.0 T Bruker Pharmascan (Bruker, Ettlingen, Germany) equipped with a 760 mT/m gradient system, using a cryogenically cooled 4 channel phased array element 1H receiver-coil (CryoProbe) and a 72 mm room temperature volume resonator for transmission and the IntraGateTM self-gating tool (Larson et al., 2004). The parameters for identification of the ECG were adapted for one heart slice and transferred afterward to the navigator signals of the remaining slices. Thus the in-phase reconstruction of all pictures is guaranteed. The measurement is based on the gradient echo method (repetition time = 6.2 ms; echo time = 1.3 ms; field of view = 2.20x2.20 cm; slice thickness = 1.0 mm; matrix = 128 x 128; oversampling = 100). The imaging plane is localized using scout images showing the 2- and 4-chamber view of the heart, followed by acquisition in short-axis view, orthogonal on the septum in both scouts. Multiple contiguous short-axis slices consisting of 7 to 10 slices are acquired for complete coverage of the left and right ventricle. Mice are measured under volatile isoflurane (1.5 – 2.0 % in oxygen and air with a flow rate of 1.0 L/min) anesthesia; the body temperature is maintained at 37°C by a thermostatically regulated water flow system during the entire imaging protocol. MRI data are analyzed using Qmass digital imaging software (Medis Imaging Systems, Leiden, Netherlands).

FACS sorting sample preparation

The ventricle was washed with ice-cold PBS after dissection and snap-frozen in liquid N_2. For cardiac nuclei isolation, the frozen ventricle was thawed in 3ml lysis buffer (5mM CaCl2, 3mM MgAc, 2mM EDTA, 0.5mM EGTA, and 10mM Tris-HCl, pH 8) in M tube (Miltenyi Biotec) and homogenized by gentleMACS Dissociator (Miltenyi Biotec) following the protocol (protein_01). The resultant homogenate was mixed with lysis buffer containing 0.4% Triton X-100, incubated on ice for 10 min, and subsequently filtered through 40 μm cell strainer (BD Bioscience). The flow-through was subjected to centrifugation at 1000 g for 5min at 4 °C to harvest nuclei. The nuclei were further purified through 1M sucrose cushion (3mM MgAc, 10mM Tris-HCl, pH8) by centrifugation at 1000g for 5 min at 4 °C, and then stained with PCM1 antibody in nuclei stain buffer (DPBS, 1% BSA, 0.2% Igepal CA-630, 1mM EDTA). DNA was stained by DAPI before FACS sorting. FACS sorting was done using a FACSAria™ III (BD Biosciences). Quantification of PCM+ cardiac nuclei and DNA content was

performed with the LSR Fortessa (BD Biosciences) analyzer. Data acquisition and analysis were done using BD FACS Diva v8 software.

RNA-seq

RNA was extracted from isolated adult CMs using the Direct-zol Total Kit (Zymo Research) combined with on-column DNase digestion (DNase-Free DNase Set, Qiagen) to avoid contamination by genomic DNA. RNA and library preparation integrity were verified LabChip Gx Touch 24 (Perkin Elmer). 200ng of total RNA was used as input for SMARTer Stranded Total RNA Sample Prep Kit - HI Mammalian (Clontech) following the manufactures instructions. Sequencing was performed on the NextSeq500 instrument (Illumina) using v2 chemistry, resulting in an average of 22M reads per library with 1x75bp single end setup. Raw reads were assessed for quality, adapter content, and duplication rates with FastQC 0.11.8 (Andrews S. 2010, FastQC: a quality control tool for high throughput sequence data. Available online at: http://www.bioinformatics.babraham.ac.uk/projects/fastqc). Trimmomatic version 0.36 was employed to trim reads after a quality drop below a mean of Q15 in a window of 5 nucleotides (Bolger et al., Trimmomatic: A flexible trimmer for Illumina Sequence). Only reads of at least 15 nucleotides were cleared for subsequent analyses. Trimmed and filtered reads were aligned versus mouse genome version mm10 (GRCm38.p5) using STAR >=2.5.4b with the parameters "--outFilterMismatchNoverLmax 0.1 --alignIntronMax 200000" (Dobin et al., STAR: ultrafast universal RNA-seq aligner). The number of reads aligning to genes was counted with featureCounts 1.6.0 from the Subread package (Liao et al., featureCounts: an efficient general-purpose program for assigning sequence reads to genomic features). Only reads mapping at least partially inside exons were admitted and aggregated per gene. Reads overlapping multiple genes or aligning to multiple regions were excluded. Differentially expressed genes were identified using DESeq2 version 1.14.1 (Love et al., Moderated estimation of fold change and dispersion for RNA-Seq data with DESeq2). Genes were classified to be significantly differentially expressed (DEG) with P-Value < 0.05. The annotation was enriched with UniProt data (release 24.03.2017) based on Ensembl gene identifiers (Activities at the Universal Protein Resource (UniProt)).

ChIP-seq, MeDIP-seq, and data analysis

The MeDIP samples were prepared according to the manufacturer's instruction (MeDIP kit, Diagenode) with genomic DNA extracted from isolated adult CM. ChIP was performed according to standard protocols. Briefly, FACS-purified cardiac nuclei were first cross-linked with 1% formaldehyde

for 10 min and then quenched using the truChIP Chromatin Shearing Kit (COVARIS) for 10 min at RT. Chromatin was sheared to an average size of 200–500 bp by sonication (Diagnode Biorupter). Protein-DNA complexes were eluted from beads by incubation with 50 µl elution buffer (10 mM Tris-HCl pH 7.4, 5 mM EDTA, 300 mM NaCl, 0.5% SDS) at RT for 5 min and treated with 1 µg DNase free-RNase (Roche) at 37 °C for 30 min. After incubation with 25 µg of proteinase K (10 mg/ml), 1 µg Glycogen at 37 °C for 2 hours, samples were heated at 65 °C with constant shaking at 1350 rpm overnight. DNA was purified with MinElute® PCR purification Kit (Qiagen) and quantified by Qubit dsDNA HS Assay Kit (Thermo Fisher Scientific). 0.5-10 ng of DNA was used as input for TruSeq ChIP Library Preparation Kit (Illumina) with the following modifications: libraries were size selected by SPRI-bead based approach after final PCR with 18 cycles instead of gel-based size selection before final PCR step. Samples were 1st cleaned up by 1× bead: DNA ratio to eliminate residuals from PCR reaction, followed by 2-sided-bead cleanup step with initially 0.6× bead: DNA ratio to exclude larger fragments. The supernatant was transferred to a new tube and incubated with additional beads in 0.2× bead: DNA ratio to eliminate small fragments, like adapter and primer dimers. Bead-bound DNA was washed with 80% ethanol, dried, and re-suspended in TE buffer. Library integrity was verified with LabChip Gx Touch 24 (Perkin Elmer). Sequencing was performed on the NextSeq500 instrument (Illumina) using v2 chemistry with 1x75bp single end setup.

Raw reads were assessed for quality, adapter content, and duplication rates with FastQC 0.11.8 (Andrews S. 2010, FastQC: a quality control tool for high throughput sequence data. Available online at: http://www.bioinformatics.babraham.ac.uk/projects/fastqc). Trimmomatic version 0.39 was employed to trim reads at a quality drop below a mean of Q15 in a window of 5 nucleotides (Bolger et al., Trimmomatic: A flexible trimmer for Illumina Sequence). Only reads of at least 15 nucleotides were cleared for subsequent analyses. Trimmed and filtered reads were aligned versus mouse genome version mm10 (GRCm38) using STAR 2.6.1d with the parameters "--outFilterMismatchNoverLmax 0.1 --outMultimapperOrder Random --outSAMmultNmax 1 --outFilterMultimapNmax 1 --alignEndsType EndToEnd --alignIntronMax 1" (Dobin et al., STAR: ultrafast universal RNA-seq aligner). These options exclude spliced and multi-mapping alignments. Reads were further de-duplicated using Picard 2.21.7 (Picard: A set of tools (in Java) for working with next-generation sequencing data in the BAM format) to mitigate PCR artifacts leading to multiple copies of the same original fragment. The MUSIC peakcaller (version from Dec. 2015) was employed in punctate mode to identify enriched regions when comparing the respective ChIP to input samples (Harmanci et al., MUSIC: identification of enriched regions in ChIP-Seq experiments using a mappability-corrected

multiscale signal processing framework). The MUSIC FDR was set to 0.2. Peaks overlapping ENCODE blacklisted regions (known misassemblies, satellite repeats) were excluded. In order to be able to compare peaks in different samples to assess reproducibility, the resulting lists of significant peaks were overlapped and unified to represent identical regions. Sample counts for union peaks were produced using bigWigAverageOverBed (UCSC Toolkit) and normalized with DESeq2 1.26.0 to compensate for differences in sequencing depth, library composition, and efficiency (Anders et al., Differential expression analysis for sequence count data). Peaks were annotated with the promoter of the nearest gene in range (TSS +- 5000 nt) using reference data of GENCODE vM15. Peaks were classified to be significantly differentially expressed with P-Value < 0.05 as produced by DESeq2.

I/R surgery

Animals were anesthetized using 4.5% isoflurane and subjected to endotracheal intubation with a 22 Gauge intravenous catheter. Mice were placed on a 37°C heating plate in the supine position and artificially ventilated at a rate of 225 strokes/min and a stroke volume of 250µl with a mixture of oxygen and 1.5% isoflurane using a MiniVent rodent ventilator. The chest hair was removed, skin disinfected, and skin opened with a small incision of several mm length from the left armpit to the sternal border. Pectoralis major and minor muscles were separated, chest opened in the 3rd intercostal space, and retractors were inserted. Then pericardium was opened to allow access to the heart. The left coronary artery was ligated for 30min and reopened for I/R in a proximal position using a prolene suture (7-0). The retractors were removed, the chest wall was closed by bringing together the 2nd and 3rd rib using a vicryl suture (5-0). The muscles were placed into their original position and the skin incision was closed with vicryl (5-0). Mice waked up several minutes after ventilation with oxygen were extubated and put back in their cages.

Adult CM hypoxia challenge and viability assay

Freshly isolated adult CMs seeded in chamber slides were immediately cultured in the hypoxia chamber with 1% O_2, 5% CO_2 at 37 °C for 18 hours. Cells cultured in normoxia condition were utilized as a control group. Cells were washed with room temperature PBS and incubated with PBS containing EthD1 (4µM) and calcineurin (2µM) for 45 min on RT. The immunofluorescence images were captured with a microscope (ZEISS Imager Z1) immediately.

Quantification of TCA cycle metabolites

Isolated CM was homogenized in 85% methanol (4µL/10,000 cells), and the homogenate was centrifuged (10,000 g, 5 minutes, 4 °C). An equal volume of supernatant was collected, isotope-labeled internal standards were added, and the samples were evaporated to dryness in a ConcentratorPlus (Eppendorf, Wesseling-Berzdorf, Germany). Samples were reconstituted in 50 µL water, transferred to autosampler vials, and subsequently analyzed by LC-MS/MS.

Liquid chromatography was performed on an Agilent 1290 Infinity LC system (Agilent, Waldbronn, Germany) consisting of a 1290 Bin Pump, a 1290 TCC column oven, a 1290 Sampler, and a 1290 Thermostat. The reversed-phase LC separation was performed using a Waters Acquity UPLC HSS T3 column (150 mm × 2.1 mm, 1.8 µm (Waters, Eschborn, Germany)) at 40 °C. Gradient elution was performed with 0.15% formic acid in water (mobile phase A) and 0.15% formic acid in acetonitrile (mobile phase B) at a flow rate of 400 µL/min. Gradient conditions were 2% B for 1.5 min, followed by a 3 min gradient to 100% B, followed by a cleaning and equilibration step, making 10 min total LC run time. The injection volume was 2.5 µL for all samples. The Autosampler temperature was 6 °C. Mass spectrometry was performed on a QTrap 5500 mass spectrometer (Sciex, Darmstadt, Germany) equipped with an ESI TurboIonSpray source. Electro spray ionization at 400 °C and -4500 V in negative ionization mode was employed. Ion source gas parameters were as followed, CUR 30 psi, GS1 45 psi, GS2 25 psi. The specific MRM transition for every compound was normalized to appropriated isotope-labeled internal standards. Calibration curves were performed with authentic standards. Analyst 1.6.2 and MultiQuant 3.0 (both from Sciex, Darmstadt, Germany), were used for data acquisition and analysis, respectively.

Quantification of metabolites using the Biocrates p400 kit

Isolated CM was homogenized in 85% methanol (4µL/10,000 cells), and the homogenate was centrifuged (10,000 g, 5 minutes, 4 °C). 10 µL of supernatant were transferred to the p400 kit filter plate and processed according to the manufactures instruction. The samples were dried under nitrogen in a TurpoVap (Biotage, Uppsala, Sweden) for 30 minutes. 50 µL of 5% phenylisothiocyanate reagent were added to each filter, and the plate was incubated at RT for 20 minutes and then dried under a nitrogen stream in a TurpoVap for 60 minutes. 300 µL of 5 mM ammonium acetate in methanol were added, and the plate was shaken at 450 rpm for 30 minutes and then centrifuged for 2 minutes at 500 g. From the eluate 150 µL were transferred to a new 96-deep well plate and 150 µL of water was added to each well and used for LC analysis. For FIA analysis, 250 µL of FIA solvent were added to each

well of the original eluate. Both plates were then shaken for 5 minutes. Ultra-performance liquid chromatography-mass spectrometry (UPLC-MS) utilized on an Accela LC system (Thermo Scientific, Dreieich, Germany) coupled to a Q-Exactive (Thermo Scientific, Dreieich, Germany) high-resolution mass spectrometer with a heated electrospray ionization (HESI-II) source and Orbitrap mass analyzer. 5 μL sample was injected onto a Biocrates UHPLC Absolute IDQ column for analysis. The mobile phases for the LC plate were solvent A (milli-Q water, 0.2% formic acid) and solvent B (acetonitrile, 0.2% formic acid) The gradient used to separate the metabolites was: 0–0.25 minutes 0% B, 1.5 minutes: 12% B; 2.7 minutes: 17.5% B; 4 minutes: 50% B; 4.50 minutes: 95% B; 5.25-5.80 minutes: 0% B at a flow rate of 860 μL/min and column oven temperature of 50 °C. Xcalibur 4.0 software (Thermo Scientific, Dreieich, Germany) was used for data acquisition calculation of molar concentrations. For FIA analysis, 20 μl sample were injected directly onto the MS, with the isocratic flow with methanol containing 3.33% Biocrates Solvent I, at a flow rate of 95 μl/min. Data evaluation for LC and FIA were performed with the MetIDQ 6.0 software (Biocrates, Innsbruck, Austria).

TUNEL Assay

The TUNEL assay was performed to manufacturer instruction with the heart paraffin section. The sarc-actinin was utilized to label the CM and DAPI was used to label the DNA. The Dnase treatment was applied on an additional paraffin section to work as a positive control.

Lentiviral transduction of CMs

HEK293T cells were grown in DMEM (Sigma) supplemented with 10% FCS (Sigma), 2mM L-Glutamine, 100U Penicillin, and 100 μg /ml Streptomycin at 37°C, 5% CO_2. HEK293T cells ($2x10^6$/10 cm dish) were transfected with 5 μg pLJM1-Kdm5B, 4.5 μg psPAX2 (Addgene #12260), and 0.5 μg pMD2.G (Addgene, 12259) using Turbofect transfection reagent and Opti-MEM™ for 6-8 hours. The lentivirus was collected 48 and 72 hours after transfection, respectively. The lentivirus was filtered through a 0.45 μM cell strainer to remove the HEK293T cell and concentrated with a Lenti-X concentrator according to the manufacturer's instruction (TaKaRa, 631231). The primary neonatal CM was infected in suspension with Polybrene (8 μg/ml) for 6 to 8 hours.

Gene expression analysis

Total RNA was extracted using TRIzol reagent (Invitrogen) according to manufacturer instruction. RNA was reverse-transcribed with Superscript II (Invitrogen) following standard procedures. Real-time PCR was performed with 2 technical replicates using StepOne™ Real-time PCR system and

KAPA SYBR ® FAST qPCR Master Mix (KAPA Biosystems, CH). Relative quantitation of gene expression was performed using the ΔΔCT method. The Ct values of the target genes were normalized to the β-actin gene using the equation $\Delta Ct = Ct_{reference} - Ct_{target}$ and expressed as ΔCt. Relative mRNA expressions are shown with the average from control samples set as 1. Primers and PCR conditions are listed in Table 8.

Statistical analysis.

For all quantitative analyses, a minimum of three biological replicates was analyzed. Statistical tests were selected based on the assumption that sample data comes from a population following a probability distribution based on a fixed set of parameters. Student's t-tests were used to determine the statistical significance of differences between the two groups. One-way AVOVA was used for multiple comparison tests. The following values were considered to be statistically significant: $*p<0.05$, $**p<0.01$, $***p<0.001$, $****p<0.0001$. Calculations were done using the GraphPad Prism 8 software package. Data are represented as mean ± the standard error of the mean. No statistical method was used to predetermine sample size.

Results

1. Inhibition of fatty acid oxidation in neonatal CMs promotes cell cycle progression *in vitro*

The heart can utilize both carbohydrates and lipid as main sources for energy production. However, utilization of these nutrients changes during heart development. To assess the shift in the energy metabolism during postnatal cardiac development, I performed bioinformatics analysis of published RNA-seq datasets of fetal, neonatal, and adult CMs for visualization of expression level of genes associated with glycolysis, cell cycle, fatty acid oxidation (FAO), and TCA cycle. mRNA levels of the glucose transporter *Slc2a4*, the dominant isoform in the adult CM, was gradually elevated, but the predominant neonatal stage glucose transporter *Slc2a1* was down-regulated during postnatal cardiac development. Cell cycle-related genes and several key enzymes catalyzing glycolysis i.e *Aldoc*, *Pgk1, Pgm1,* and *Eco2* were downregulated from neonatal to the adult stages, while expression of a large group of genes related to FAO and TCA cycle were substantially up-regulated (Fig. 9A). In parallel, expression of the muscle isoform of carnitine palmitoyltransferase *Cpt1b* but not the hepatic isoform *Cpt1a*, enzymes that catalyze a rate-limiting step of fatty acid oxidation (FAO), was rapidly upregulated in the first week after birth, confirming the metabolic shift from glycolysis to FAO in the early phase of postnatal development (Fig. 9A&B). Consistent with previous studies, my results revealed a rapid switch of energy metabolism from glycolysis into fatty acid oxidation during the early postnatal cardiac development (Lopaschuk and Jaswal, 2010; Lopaschuk and Spafford, 1992).

To test whether metabolic reprogramming affects cell cycle activity, I treated cultured P0-1 neonatal CMs with Etomoxir, an inhibitor of CPT1. After 72 hours of treatment, EdU incorporation in neonatal CM increased from 3% to 6% (Fig. 9C). In addition, the percentage of Ki67 positive and pH3 (Ser10) CMs also increased significantly (Fig. 9D). Furthermore, protein levels of the cell cycle marker Cyclin E1 were strongly elevated after CPT1 inhibition (Fig. 9E). These results indicate that FAO inhibition in CM reprograms energy metabolism and promotes CM proliferation.

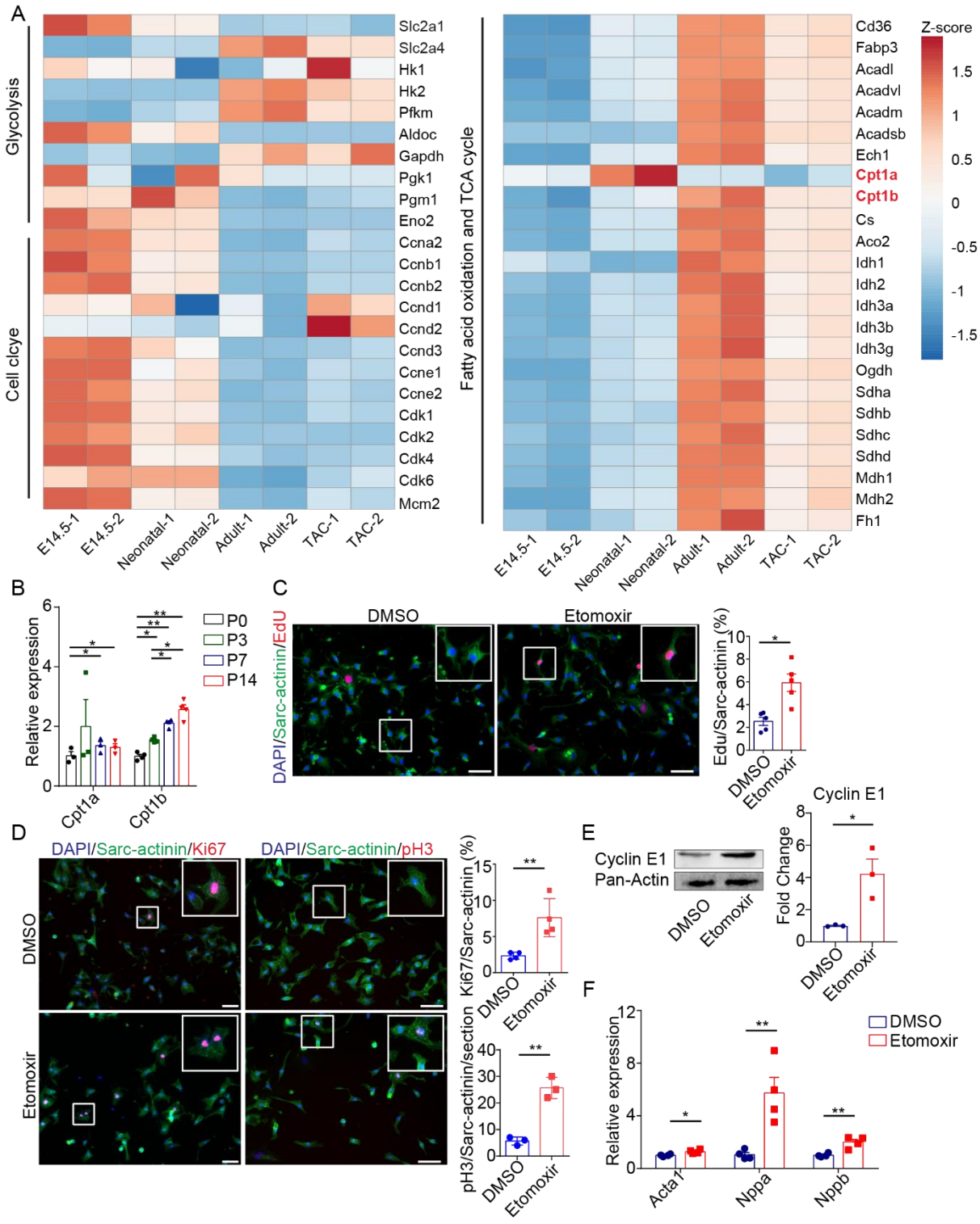

Fig 9. Etomoxir (CPT1i) treatment promotes P0-1 CM cell cycle progression

(A) Heat map reflecting normalized counts transformed by z score of genes involved in glycolysis, cell cycle, fatty acids oxidation, and TCA cycle based on published RNA-seq of CMs isolated from mouse fetus at E14.5, P1-2 neonatal and 2-month-old adult mice, or adult mice one week after TAC (GSE79883). **(B)** RT-qPCR analysis of *Cpt1a* (n=3) and *Cpt1b*

(n=4) expression during different heart developmental stages (P0, P3, P7, P14) with ventricle samples isolated from C57BL6 pups. *36b4* was utilized as a reference gene. **(C)** EdU incorporation assay with neonatal CMs 72 hours after DMSO or Etomoxir treatment. The amplified immunofluorescence (IF) images of selected areas are shown in the white frames. Quantification of EdU+/Sac-actinin+ CM is shown in the right panel. Scale bar: 50 μm. **(D)** Representative IF images of neonatal CMs co-stained for Sarc-actinin and proliferative markers Ki67 (n=4) or pH3 (Ser10) (n=3) with or without Etomoxir treatment, respectively. Quantification of Ki67+/Sac-actinin+ or pH3+/Sac-actinin+ CMs is shown in the right panels. Scale bar: 50 μm. **(E)** Western blot analysis of Cyclin E1 in P0-1 neonatal CMs after 3 days culture in the presence of DMSO or Etomoxir (n=3). Pan-Actin was used as an internal loading control. **(F)** RT-qPCR analysis of hypertrophic associated gene expression in P0-1 neonatal CMs 72 hours after DMSO or Etomoxir treatment (n=4). *36b4* was utilized as a reference gene. **B-F**: Error bars represent mean ± s.e.m. Statistical analysis was performed with one-way ANOVA in **B**, with unpaired t-test in **C-F**. * $p<0.05$, ** $p<0.01$, *** $p<0.001$. (RNA-seq data analysis was assisted by Dr. Carsten Künne)

In addition, I also determined the expression level of cardiac hypertrophic growth-associated markers after inhibition of FAO via Etomoxir treatment. The mRNA levels of *Nppa* and *Nppb*, which are highly expressed during early CM maturation and dedifferentiating adult CM were significantly increased in Etomoxir-treated neonatal CMs. Notably, the skeletal muscle α-actin (*Acta1*), which is up-regulated in neonatal and de-differentiating adult CMs, was also significantly increased upon Etomoxir treatment (Fig9 F). In conclusion, these results suggest that abrogation of fatty acid oxidation maintains neonatal CMs in an immature state, characterized by proliferation capacity and elevated expression of early developmental stage markers. I, therefore, speculated that manipulation of CM metabolism provides an approach to extend the proliferation window of CMs and enhance heart regeneration capacity after myocardial infarction.

2. Specific ablation of *Cpt1b* in CM leads to cardiomegaly of adult hearts

To further investigate the correlation between energy metabolism and heart regeneration and remodeling *in vivo*, a mouse line was generated in which *Cpt1b* is specifically deleted in CM. This mouse line contained the *Cpt1b* gene alleles in which exon ten and eleven of the *Cpt1b* gene were flanked by two *loxP* sites after homology recombination with a targeting vector. The Cre recombinase that directs excision of flanked exons was expressed under control of the αMHC promoter (Myosin Heavy Chain 6, *Myh6*, αMHC). Since αMHC is a cardiac-specific gene, αMHC-Cre mediated deletion of these two exons from *Cpt1b* loci was specifically restricted to CMs (Fig10 A).

To validate the efficiency of *Cpt1b* ablation, I performed RT-qPCR to detect the mRNA level of *Cpt1b* in isolated adult CMs. *Cpt1b* expression was substantially reduced in mutant CMs isolated from αMHC-

$Cre^{Pos/+}$ $Cpt1b^{fl/fl}$ (thereafter referred as $Cpt1b^{cKO}$) mice compared to control CMs from αMHC-$Cre^{Pos/+}$ $Cpt1b^{+/+}$ mice (thereafter referred as $Ctrl^{Cre}$) and αMHC-$Cre^{+/+}$ $Cpt1b^{fl/fl}$ (thereafter referred as $Ctrl^{Flox}$). A compensatory up-regulation of *Cpt1a* was not observed (Fig10 B). In addition, the protein of CPT1B was almost undetectable by western blot analysis in adult CMs isolated from $Cpt1b^{cKO}$ mice, confirming the high efficiency of *Cpt1b* inactivation in this mouse line (Fig10 C).

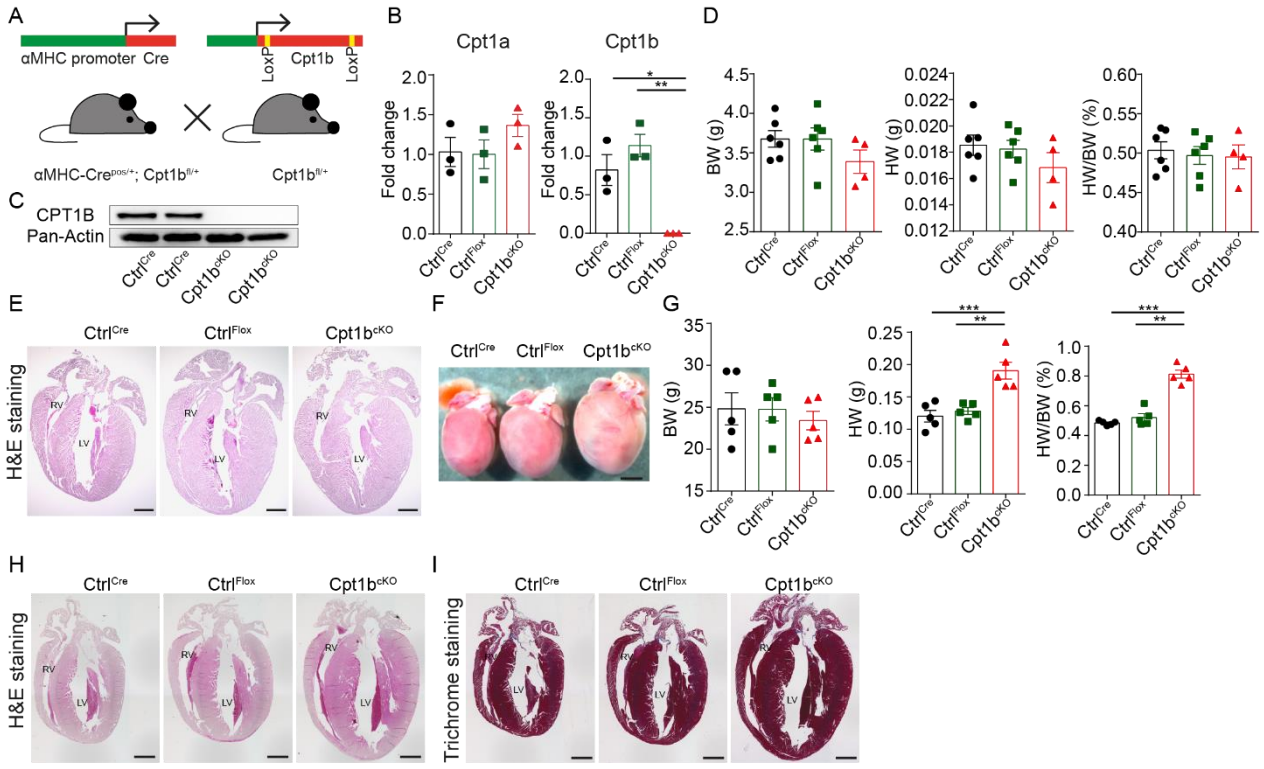

Fig10. Conditional inactivation of *Cpt1b* in CM induces cardiomegaly in adult mice

(A) Strategy for generation of *Cpt1b* conditional KO mouse. **(B)** RT-qPCR analysis of *Cpt1a* and *Cpt1b* gene expression in CMs isolated from 10-week-old αMHC-$Cre^{pos/+}$, $Cpt1b^{+/+}$ ($Ctrl^{Cre}$); αMHC-$Cre^{+/+}$, $Cpt1b^{fl/fl}$ ($Ctrl^{flox}$) or αMHC-$Cre^{pos/+}$, $Cpt1b^{fl/fl}$ ($Cpt1b^{cKO}$) mice (n=3). *36b4* was utilized as a reference gene. **(C)** Western blot analysis of CPT1B in adult CMs isolated from 10-week-old $Ctrl^{Cre}$ and $Cpt1b^{cKO}$ mice (n=2). Pan-Actin was used as an internal loading control. **(D)** Analysis of body weight (BW), heart weight (HW) and the ratio of heart weight/body weight (HW/BW) of P7 $Ctrl^{Cre}$ (n=6), $Ctrl^{Flox}$ (n=6) or $Cpt1b^{cKO}$ (n=4) mice. **(E)** H&E staining of heart paraffin sections dissected from P7 $Ctrl^{Cre}$, $Ctrl^{Flox}$, and $Cpt1b^{cKO}$ mice (n=3). Scale bar: 500 µm. **(F)** Macroscopic image of the hearts dissected from 10-week-old $Ctrl^{Cre}$, $Ctrl^{Flox}$, and $Cpt1b^{cKO}$ mice. Scale bar: 2 mm. **(G)** Analysis of BW, HW, and the HW/BW ratio of 10 weeks $Ctrl^{Cre}$, $Ctrl^{Flox}$, or $Cpt1b^{cKO}$ mice (n=5). **(H)** H&E staining of heart paraffin sections dissected from 10-week-old $Ctrl^{Cre}$, $Ctrl^{Flox}$, and $Cpt1b^{cKO}$ mice (n=3). Scale bar: 1000 µm. **(I)** Trichrome staining of paraffin sections of the heart dissected from 10-week-old $Ctrl^{Cre}$, $Ctrl^{Flox}$, and $Cpt1b^{cKO}$ mice (n=3). Scale bar: 1000 µm. **B, D, G**: Error bars represent mean ± s.e.m. Statistical analyses were performed with one-way ANOVA in **B**, **D**, **G**. * $p<0.05$, ** $p<0.01$, *** $p<0.001$.

To evaluate the impact of FAO inhibition cardiac homeostasis at the early postnatal stage, mutant mice were examined at P7. No significant differences in body weight, heart weight, and the heart weight/body weight ratio, a parameter used to quantify cardiac hypertrophic growth, were detected between $Ctrl^{Cre}$, $Ctrl^{Flox}$, and $Cpt1b^{cKO}$ mice at P7 (Fig10 D). In addition, H&E staining did not reveal any obvious morphological abnormities caused by loss of *Cpt1b* in P7 hearts (Fig10 E). In conclusion, CM-specific *Cpt1b* ablation has no adverse effects on early postnatal development of the heart. It seems likely that inhibition of the metabolic switch from glycolysis to fatty acid oxidation in P7 CM did not cause dramatic phenotypical changes, because potential consequences of metabolic reprogramming need more time to unfold.

In contrast to the normal appearance at P7, the situation changed dramatical 8-10 weeks after birth. Hearts of *Cpt1b* mutant mice were markedly enlarged compared to control littermates, although the body weight did not show a significant difference (Fig10 F&G). In line with these findings, both the heart weight and the heart weight/body weight ratio were dramatically increased in $Cpt1b^{cKO}$ mice compared with $Ctrl^{Cre}$ and $Ctrl^{Flox}$ animals (Fig10 G). Morphological analysis by H&E staining revealed a strong increase of thickness of both left ventricle and septum in *Cpt1b* mutant heart without any dilation indicating that FAO inhibition growth of the heart (Fig10 H).

To determine whether the increase in heart size observed in $Cpt1b^{cKO}$ mice was physiological or pathological, I evaluated the collagen deposition within the myocardium by trichrome staining, since severe fibrosis is one of the hallmarks of pathological cardiac hypertrophy. The valve was positively stained, while no apparent collagen deposition within ventricles and septum was found in $Ctrl^{Cre}$, $Ctrl^{Flox}$, and $Cpt1b^{cKO}$ animals (Fig10 I). This result indicates that the *Cpt1b* ablation results in strong physiological cardiac growth when fatty acids are not anymore the dominant source used for energy production.

3. CPT1B deficiency does not impair contractility of the adult heart

Next, I performed Magnetic resonance imaging (MRI) of ten weeks old $Ctrl^{Cre}$, $Ctrl^{Flox}$, and $Cpt1b^{cKO}$ mice to evaluate the impact of *Cpt1b* deficiency on heart function. Consistent with physiological cardiac growth, MRI analysis revealed that the wall thickness of the left ventricle and septum were dramatically increased at both the end of the systolic phase and the end of the diastolic phase (Fig11 A). Both the

end of the systolic volume (ESV) and the end of the diastolic volume (EDV) did not show any significant differences between these three groups of mice. Similarly, both the ejection fraction (EF) and cardiac output in Cpt1b^{cKO} mice remained at a similar level as in Ctrl^{Cre} and Ctrl^{Flox} mice, indicating that contractility was not impaired in *Cpt1b* deficient heart (Fig11 B).

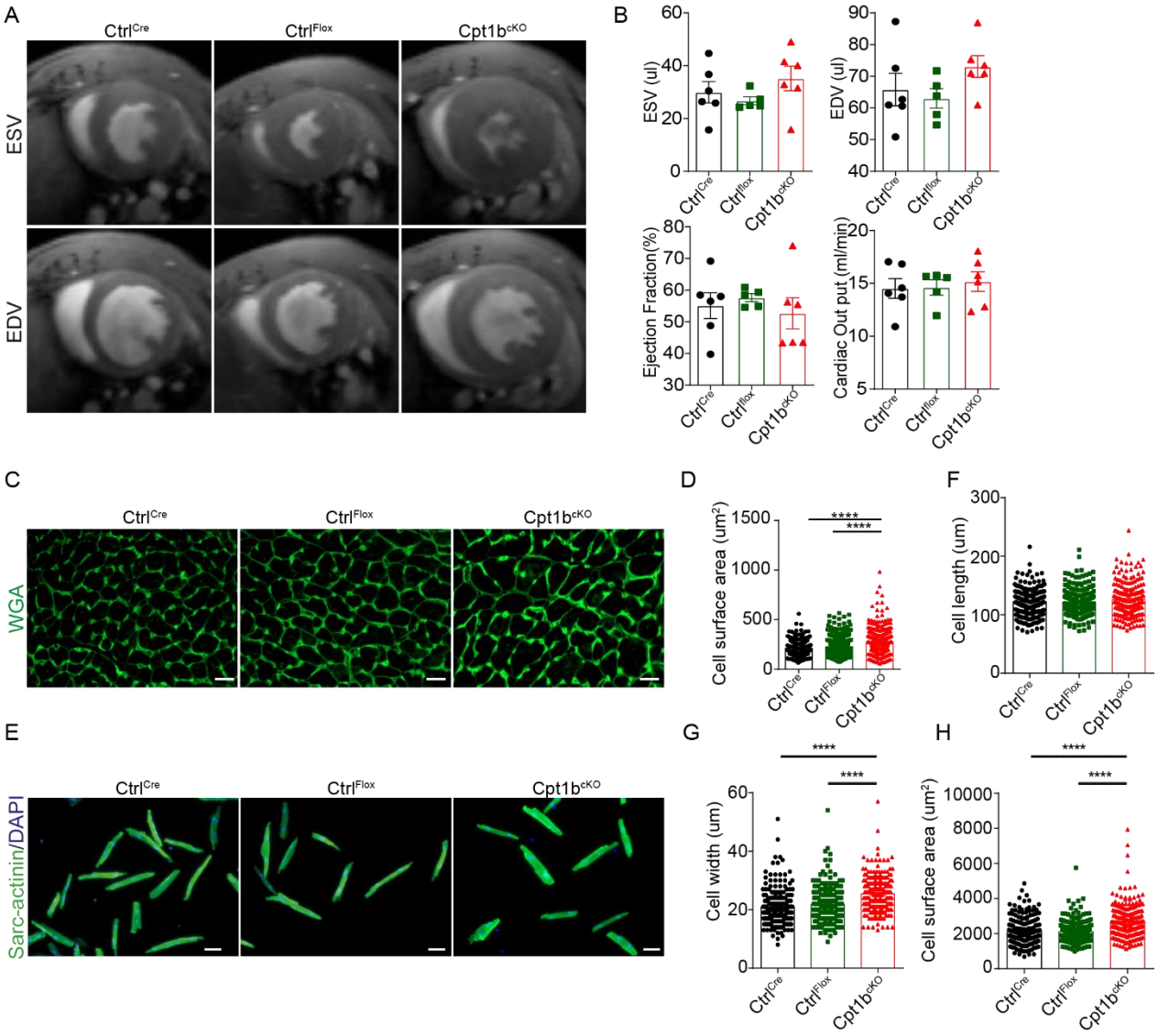

Fig11. Cardiac-specific ablation of *Cpt1b* does not impair cardiac contraction.

(A-B) Representative cardiac Magnetic resonance imaging (MRI) images of 10-week-old Ctrl^{Cre}, Ctrl^{Flox}, and Cpt1b^{cKO} mice (A). MRI analysis of heart function of 10-week-old Ctrl^{Cre} (n=6), Ctrl^{Flox} (n=5) and Cpt1b^{cKO} (n=6) mice. End of systolic volume (ESV), End of diastolic volume (EDV), Ejection Fraction, and Cardiac Output were evaluated with Medis® Suite software, respectively (B). **(C-D)** IF staining of heart paraffin sections dissected from 10-week-old Ctrl^{Cre} (n=3), Ctrl^{Flox} (n=3) or Cpt1b^{cKO} (n=3) mice with α-WGA antibody (C). Scale bar: 20μm. Cell surface area of individual adult CM was quantified with ImageJ software (D). Around 120 CMs randomly selected from 5-6 sections of each heart sample were quantified. **(E-H)** Representative images of sarc-actinin+ adult CMs isolated from 10-week-old Ctrl^{Cre}, Ctrl^{Flox}, and Cpt1b^{cKO} mice (n=3) (E). Quantification of cell length (F), width (G), and surface area (H) were performed with ImageJ.

Around 60-70 CMs randomly selected from each heart sample were quantified. Scale bar: 50 μm. **B, D, F-H**: Error bars represent mean ± s.e.m. Statistical analysis were performed with one-way ANOVA in **B, D, F-H**, * $p<0.05$, ** $p<0.01$, *** $p<0.001$, **** $p<0.0001$. (MRI analysis was assisted by Dr. Astrid Wietelmann)

To further address the growth phenotype of *Cpt1b* mutant hearts, I evaluated the individual cell size of adult CMs. The cell surface area of individual CM was quantified after Wheat Germ Lectin (WGA) immunofluorescence staining of paraffin heart section obtained from adult $Ctrl^{Cre}$, $Ctrl^{Flox}$, and $Cpt1b^{cKO}$ mice (Fig11 C). I found that the surface area of CM from $Cpt1b^{cKO}$ animals was significantly increased compared to $Ctrl^{Cre}$ and $Ctrl^{Flox}$ mice (Fig11 D). To exclude the influence of different CM orientations in the myocardium, the cell length, width, and surface area of isolated adult CM (Sarc-actinin positive) were evaluated, respectively (Fig11 E). Consistent with the results on sections, the cell surface area was increased significantly in isolated $Cp1b^{cKO}$ CM compared with both $Ctrl^{Cre}$ and $Ctrl^{Flox}$ CM. Moreover, isolated $Cp1b^{cKO}$ CM showed a marked increase in cell width but not cell length, attributing the enlarged cell size mainly to an increase of cell width (Fig11 F-H). Together with the morphology analysis, the enlarged heart size observed in *Cpt1b* deficient animal is, at least partially, caused by the hypertrophic growth of individual CM.

4. Cardiac hyperplasia induced by *Cpt1b* ablation contributes to the cardiomegaly phenotype

An increase of CM numbers may also account for increased cardiac growth. To examine this possibility, I performed immunofluorescence staining for Ki67 to evaluate the cell cycle activity of adult CMs, using heart paraffin section prepared from 10 weeks old $Ctrl^{Cre}$, $Ctrl^{Flox}$, and $Cpt1b^{cKO}$ mice (Fig12 A). Adult CM primarily reside in the G0 phase with a low self-renewal capacity under physiological conditions (McCommis et al., 2020). Impressively, the number of Ki67 positive adult CM increased strongly in *Cpt1b* mutant compared to $Ctrl^{Cre}$ and $Ctrl^{Flox}$ hearts, in which the number of Ki67 positive CM was very low (Fig12 B).

To confirm that enhanced proliferation of $Cpt1b^{cKO}$ CM occurs *in vivo*, I performed an EdU incorporation assay by six times injection of EdU into adult $Ctrl^{Cre}$ and $Cpt1b^{cKO}$ mice (Fig12 C). To quantify EdU-labeled CMs, I stained isolated nuclei with PCM1 antibody, which specifically marks cardiac but not other nuclei in the heart (Gilsbach et al., 2018). The percentage of EdU positive cardiac nuclei (EdU+/PCM1+) was evaluated by FACS analysis, which revealed a higher percentage of EdU

incorporation in *Cpt1b* deficient than in control CMs (Fig12 D&E). DNA content analysis showed an increased percentage of polyploidization (4N and ≥ 4N) nuclei within *Cpt1b* deficient adult CM, indicating an enhanced DNA synthesis (Fig12 D&E).

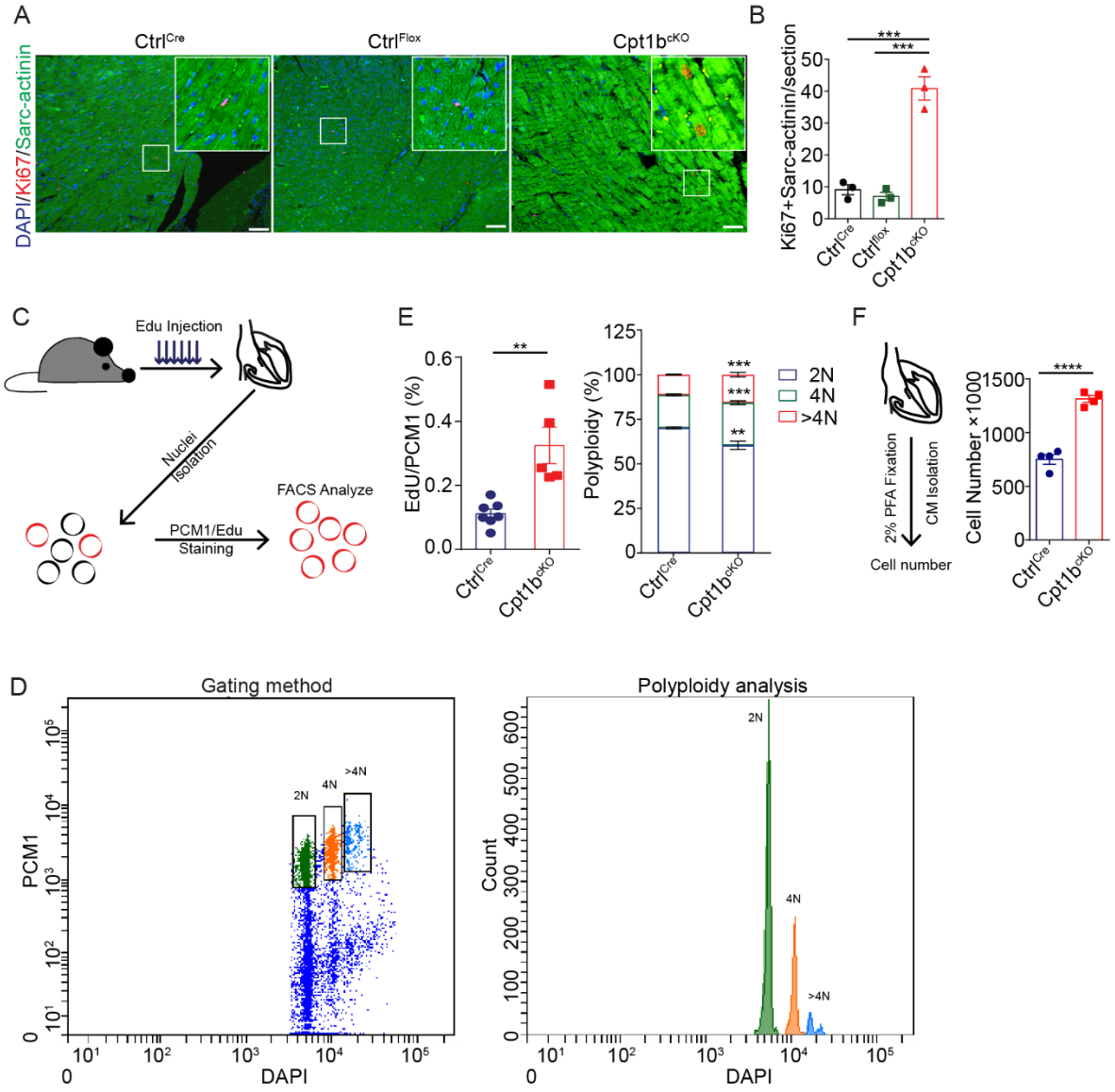

Fig12. *Cpt1b* ablation increases the number of CMs in the heart.

(A-B) Representative IF staining images of paraffin section of the hearts dissected from 10-week-old Ctrl^{Cre}, Ctrl^{Flox}, and Cpt1b^{cKO} mice stained with Ki67 and Sarc-actinin antibodies (A). The quantification of Ki67+ Sarc-actinin+ CMs per heart section was shown in B (n=3). Scale bar: 50 μm. **(C)** Scheme depicting the experimental design of EdU incorporation assay with isolated cardiac nuclei by FACS. **(D)** Gating strategy to sort PCM1 positive adult CM nuclei (left panel). The polyploidy DNA content was determined by DAPI staining (right panel). **(E)** FACS analysis of PCM1+ cardiac nuclei isolated from Ctrl^{Cre} (n=7) and Cpt1b^{cKO} (n=5) hearts to detect EdU incorporation (left panel) and DNA content based on DAPI staining signal per nuclei (right panel). **(F)** Quantification of adult CM number isolated from Ctrl^{Cre} and Cpt1b^{cKO}

hearts after collagenase B digestion (n=4). **B, E-F**: Error bars represent mean ± s.e.m. Statistical analysis was performed with one-way ANOVA in **B**, with unpaired t-test in **E-F**, * $p<0.05$, ** $p<0.01$, *** $p<0.001$, **** $p<0.0001$. (FACS data analysis was assisted by Dr. Ann Atzberger)

Ki67 staining and EdU incorporation only indicates that CMs have entered the cell cycle. To investigate whether enhanced cell cycle activity under *Cpt1b* deficient conditions led to proliferation of CMs, I quantified the CM number in hearts. After 2% PFA fixation, the hearts were digested with Collagenase B, and the number of rod-shaped adult CM was counted after complete disassociation of the tissue. Impressively, the *Cpt1b* mutant mice contained more than 1 million CMs per heart on average, whereas the $Ctrl^{Cre}$ heart had around 0.75 million CMs (Fig12 F). This result strongly suggests that the abrogation of fatty acid utilization due to inactivation of *Cpt1b* in CM leads to continuous CM proliferation and hypertrophic growth, which eventually results in cardiomegaly without adverse effects on heart function.

5. Genes associated with heart maturation and function are down-regulated in *Cpt1b* deficient adult CM

To better understand the molecular mechanism causing cardiomegaly following *Cpt1b* ablation, transcriptional changes induced by inactivation of *Cpt1b* in CM were evaluated by RNA-seq. Differentially expressed genes (DEG) were defined with the following standards: Counts > 5; $\log_2$ (fold change of mutant vs control) > 0.3 or <-0.3; p-value ≤ 0.05 (Fig13 A). Based on these standards, I identified 751 up-regulated genes and 762 down-regulated genes (Fig13 A). Next, I performed Gene Ontology (GO term) analysis of both up and down-regulated genes using a website-based functional ontology tool (DAVID website). Within the group of up-regulated genes, GO terms associated with lipid metabolic process, triglyceride metabolic process were over-represented, suggesting a compensatory effect after blockage of fatty acid oxidation. Interestingly, the down-regulated genes were mainly associated with cardiac muscle contraction, heart development, and cardiac myofibril assembly (Fig13 B&C), indicating the *Cpt1b* deficient adult CMs are relatively immature compared to $Ctrl^{Cre}$ CMs.

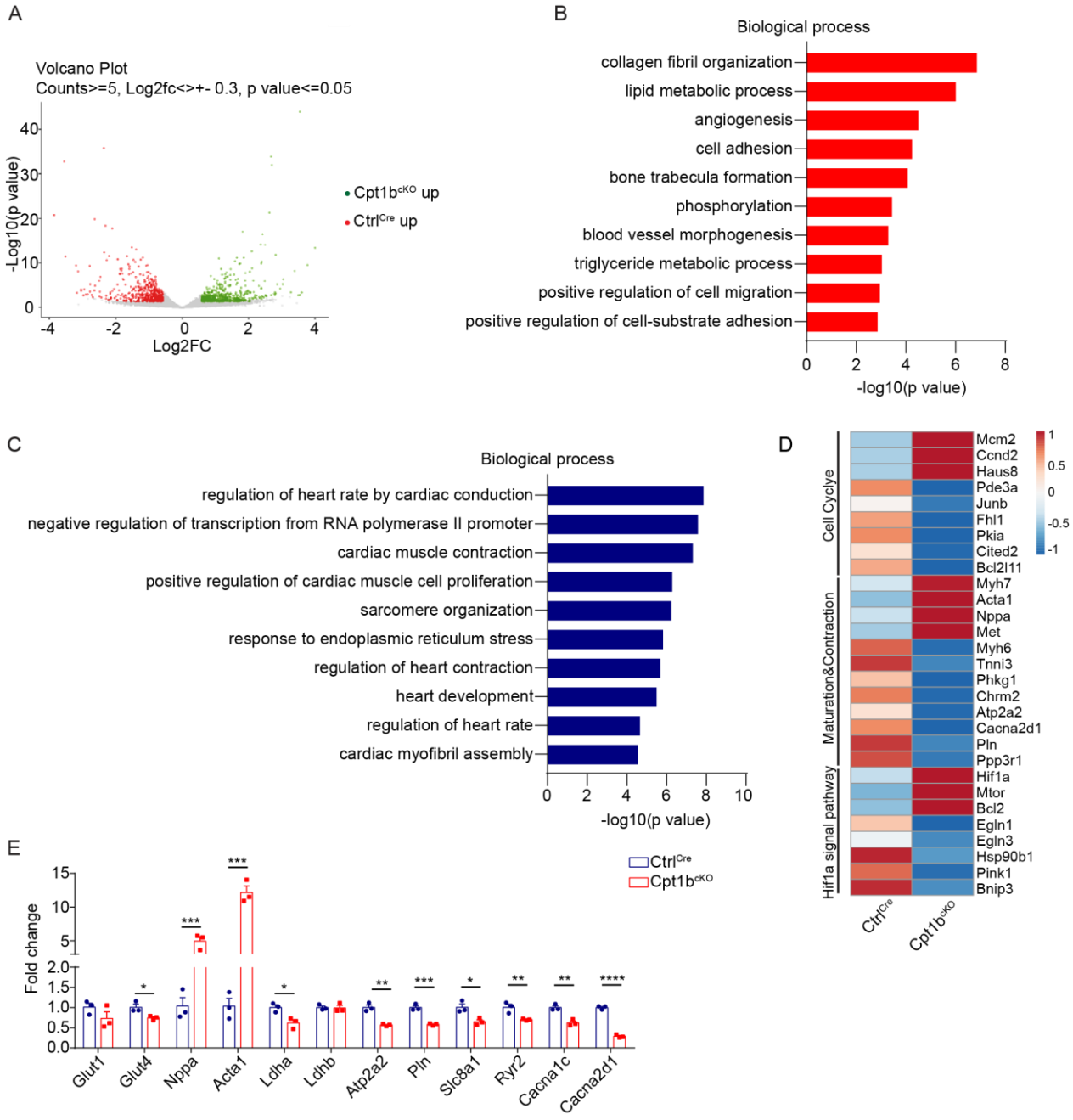

Fig13. Genes associated with cardiac postnatal maturation and contractile function are down-regulated in *Cpt1b* mutant adult CM.

(A) Volcano plot showing the differentially regulated genes (DEGs) comparing $Ctrl^{Cre}$ vs. $Cpt1b^{cKO}$ (n=3). Green dots indicate upregulated genes in CPT1B deficient adult CM, and red dots indicate downregulated DEGs, respectively. **(B-D)** GO term enrichment analysis of both upregulated (B) and downregulated (C) genes in $Cpt1b^{cKO}$ CMs. Heat map of selected DEGs involved in the cell cycle, maturation, and contraction, and the HIF1α signaling pathway based on the Z-score transformed DEseq normalized counts (D). **(E)** RT-qPCR analysis of expression of selected genes in CMs isolated from 10-week-old $Ctrl^{Cre}$ and $Cpt1b^{cKO}$ mice. *36b4* was utilized as a reference gene. **E:** Error bars represent mean ± s.e.m.

Statistical analysis was performed with unpaired t-test in **E**, * $p<0.05$, ** $p<0.01$, *** $p<0.001$. (NGS experiment was done with the help of Dr. Stefan Guenther, RNA-seq data analysis was assisted by Dr. Carsten Künne)

Next, I dissected the specific pathways over-represented by DEGs to gain a deeper insight into transcriptional network changes (Fig13 D). Consistent with the enhanced proliferation observed in *Cpt1b* mutant CM, mRNA levels of several cell cycle-related genes e. g. *Mcm2*, *Ccnd2*, and *Haus8* were significantly enhanced in *Cpt1b* mutant adult CM. Interestingly, similar to the Etomoxir-treated P0-1CM, genes associated with the early postnatal development such as *Myh7*, *Acta1*, and *Nppa* were significantly up-regulated. Moreover, genes linked to sarcomere assembly like *Myh6*, *Tnni3*; Ca^{2+} signaling e.g. *Atp2a2*, *Pln*, *Cacna2d1*, that are highly expressed in mature adult CMs to support heart contraction, were strongly down-regulated. RT-qPCR results further validated the changes of mRNA levels of genes related to postnatal maturation, such as *Nppa*, *Acta1*, *Atp2a2*, *Pln*, *Cacna2d1, Slc8a1,* and *Ryr2* (Fig13 E). These findings confirm that FAO inhibition retains CM in an immature state. Interestingly, the expression of *Hif1a,* a gene that has been reported to support adult CM self-renewal and enhance heart regeneration after acute myocardial infarction (Nakada et al., 2016), was markedly up-regulated, whereas the genes *Egln1* and *Egln3* encoding Prolyl hydroxylases responsible for HIF1a degradation were significantly down-regulated (Fig13 D).

In conclusion, the transcriptome analysis results indicate that inhibition of FAO in the early postnatal development stage, CMs retain proliferation capacity but lose their ability to reach full maturity.

6. *Cpt1b* inactivation improves the repair of myocardial ischemia-reperfusion injury

To investigate whether immature adult CMs, characterized by enhanced proliferation capacity are able to improve heart regeneration following myocardial injury, ischemia/reperfusion (I/R) surgery was performed in seven weeks old $Ctrl^{Cre}$ and $Cpt1b^{cKO}$ mice. After 30 min of ischemia via ligation of the left anterior descending artery, the heart was re-perfused. The heart samples were collected three weeks after surgery and Trichrome Staining was performed to evaluate collagen deposition, indicative of scar formation. Successive heart paraffin sections were prepared, starting from the apex to the ligation site for each individual heart. Four sections, namely the 1st to 4th layers were selected for analysis to account for effects resulting from differences in heart size. The outermost layer of the heart, which shows blue-stained areas representing collagen deposition, indicates the ligation site (Fig14 A). Importantly, the damaged area was nearly undetectable in the myocardium of $Cpt1b^{cKO}$ mice, while

prominent blue-stained damage areas were present in both the 2nd and 3rd layer of Ctrl^{Cre} hearts (Fig14 A). Quantification of damaged areas at the 2nd layer of the section revealed reduced scar areas in *Cpt1b* mutant heart compared to control mice after I/R injury, both on an absolute scale and relative to the heart size (Fig14 B&C). Furthermore, analysis of heart samples 72 hours after I/R surgery by immunofluorescence staining analysis for Ki67 and CM markers on the paraffin section identified Ki67+Sarc-actinin+ CM in the border zone of *Cpt1b* deficient heart, which were absent in control hearts (Fig15 A). The damaged areas themselves were loaded with infiltrating immune cells, including macrophages and neutrophils, which help to remove the dead CMs after I/R injury (Fig15 A) (Lorchner et al., 2015). In contrast to the border zone, no cells that stained positive for CM markers were present in the damaged area (Fig15 A) This result indicates that the improved heart regeneration capacity of *Cpt1b* deficient heart is based, at least partially on the proliferative capacity of CM. Damage-induced infiltration of immune cells was still ongoing 72 hours after I/R surgery and scar formation or collagen deposition had just started.

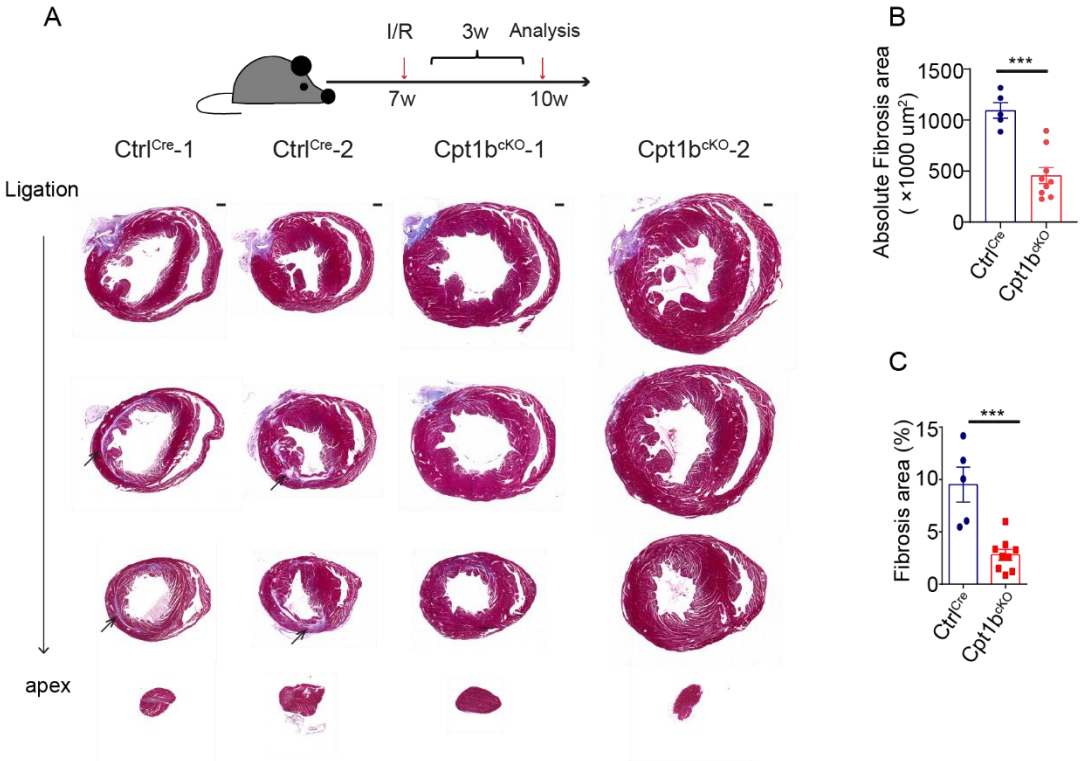

Fig14. *Cpt1b* deficient CMs reduce scar formation induced by ischemia/reperfusion

(A-C) Trichrome staining of heart paraffin sections dissected from Ctrl^{Cre} (n=5) and Cpt1b^{cKO} (n=9) 3 weeks after I/R induced myocardial injury (A). A scheme depicting the experimental procedure is presented in the upper panel. The black arrows indicate the damaged areas within the myocardium. Quantification of scar area was performed with ImageJ software

and shown in B and C. Scale bar: 600 μm. **B-C:** Error bars represent mean ± s.e.m. Statistical analysis was performed with unpaired t-test in **B** and **C**. * $p<0.05$, ** $p<0.01$, *** $p<0.001$. (I/R surgery was done with the help of Marion Wiesnet)

7. *Cpt1b* deficiency protects the myocardium from ischemia/reperfusion injury

Since HIF1α signaling was more active in *Cpt1b* deficient adult CM, I assumed that *Cpt1b* deficient CM might also be more resistant to ischemia-induced injury. Resistance to ischemia-induced injury may be caused by a different architecture of the vascular tree in *Cpt1b* deficient adult hearts including presence of collateral vessels or enhanced survival of Cpt1b-mutant CM under hypoxia. Careful analysis of the extent of non-perfused myocardium after LAD-ligation, which manifests by a pale color of the myocardium, did not uncover any notable difference between mutants and controls, essentially ruling out differences in the vascular network as the underlying cause for reduced scar formation in *Cpt1b* deficient heart (Fig15 B). To investigate improved tolerance of *Cpt1b* deficient CM to hypoxia, adult CMs from 10 weeks old $Ctrl^{Cre}$ and $Cpt1b^{cKO}$ mice were isolated and subjected for 18 hours to hypoxia (1% O_2) in vitro. Viability of control and *Cpt1b* deficient CM was analyzed by visualizing the incorporation of either EthD1, which stains DNA of dying cells, or Calcein, which labels living cells (Fig15 C). I found that the percentage of dead cells (EthD+) was significantly reduced in *Cpt1b* deficient adult CMs after exposure to hypoxia (Fig15 C). Taken together, these data suggest that the reduced myocardium damage in *Cpt1b* deficient heart results from a combination of cardiac regeneration, manifest by enhanced CM proliferation and protective effect, based on increased resistance of *Cpt1b* deficient CM to hypoxia.

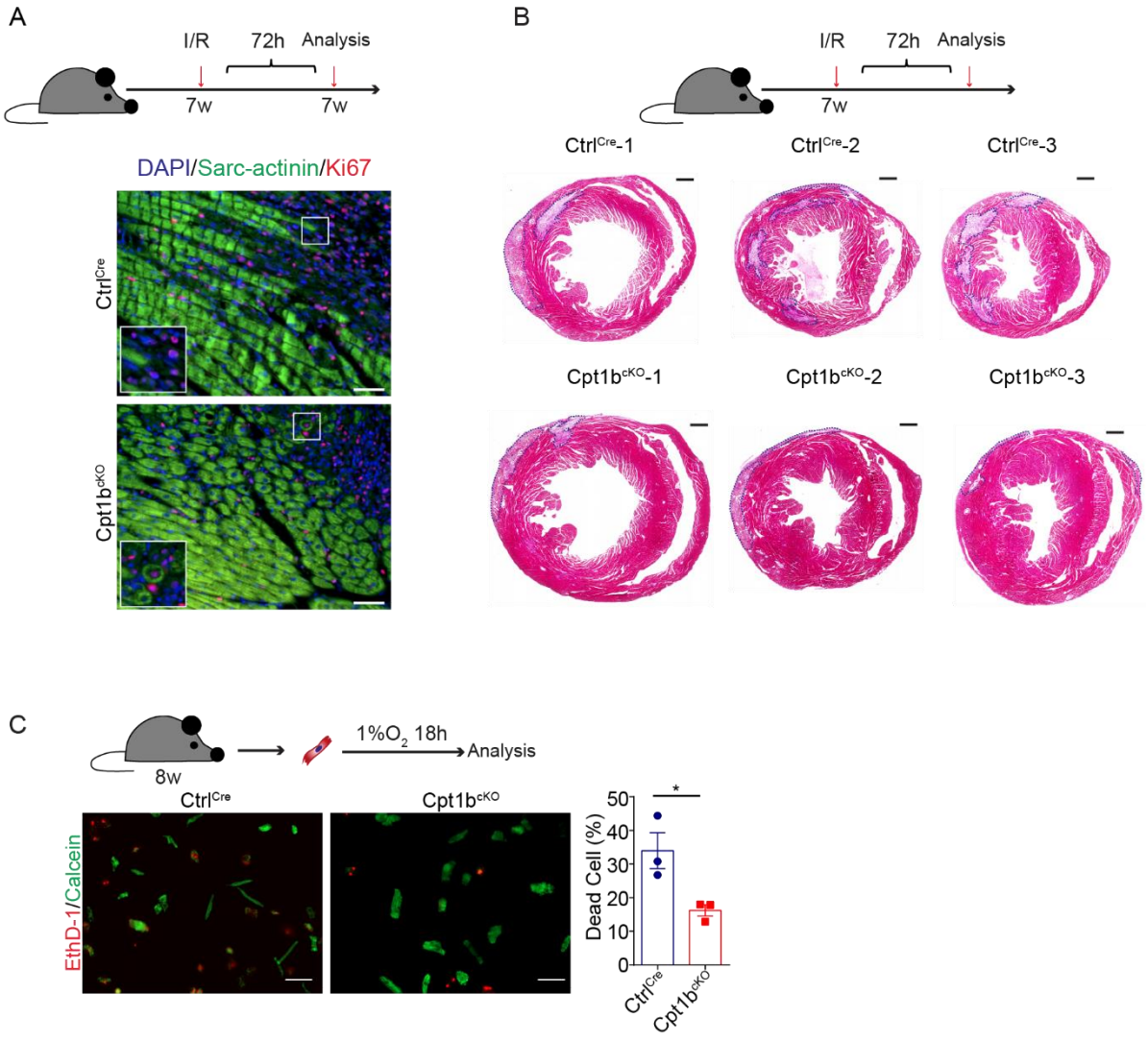

Fig15. *Cpt1b* deficiency protects the myocardium from ischemia/reperfusion damage.

(A) IF analysis of Ki67 and Sarc-actinin with paraffin sections of adult hearts dissected from $Ctrl^{Cre}$ and $Cpt1b^{cKO}$ mice 72 hours after I/R induced myocardial injury. Scale bar: 50 µm. A scheme depicting the experimental procedure is presented in the upper panel. **(B)** Trichrome staining of heart paraffin sections dissected from $Ctrl^{Cre}$ and $Cpt1b^{cKO}$ mice 72 hours after I/R induced myocardial injury. A scheme depicting the experimental procedure is presented in the upper panel. The blue dashed lines mark the damaged areas within the myocardium. Scale bar: 500 µm. **(C)** Cell viability assay of adult CMs isolated from $Ctrl^{Cre}$ and $Cpt1b^{cKO}$ mice after hypoxic exposure (1% O_2) for 18 hrs. The experimental design is shown in the upper panel. Quantification of dead cells (EthD-1+) is shown in the right panel (n=3). Scale bar: 100 µm **C:** Error bars represent mean ± s.e.m. Statistical analysis was performed with an unpaired t-test in **C**, * $p<0.05$. (I/R surgery was done with the help of Marion Wiesnet)

8. Inducible ablation of *Cpt1b* in adult CM causes heart enlargement with persevered heart function

So far, inactivation of *Cpt1b* ablation was achieved by αMHC-Cre, which mediated excision of floxed exons at embryonic stage E9.5. My findings demonstrated that inhibition of fatty acid utilization during postnatal development retains the CM in an immature state. To address the impact of FAO inhibition in terminally differentiated adult CM, I generated a *Cpt1b* inducible KO animal model using αMHC-MerCreMer mouse line, in which activity of Cre recombinase was started in fully matured adult CM by Tamoxifen (TAM) injections (Fig16 A). To induce ablation of *Cpt1b* in adult hearts, eight-weeks-old animals were subjected to daily TAM injection over 10 days. Heart samples were collected 4 and 8 weeks after the last TAM injection for further analysis.

To validate the *Cpt1b* ablation efficiency, mRNA level of *Cpt1b* was monitored in adult CMs isolated 4 weeks after TAM injection from αMHC-MCM$^{pos/+}$Cpt1b$^{+/+}$ (Ctrl), αMHC-MCM$^{pos/+}$ Cpt1b$^{fl/+}$ (Cpt1b^{Heter}) and αMHC-MCM$^{pos/+}$ Cpt1b$^{fl/fl}$ (Cpt1b^{iKO}) mice. Expression of *Cpt1b* was reduced by around 50% in Cpt1b^{Heter} CMs compared to the Ctrl CMs, since only one *Cpt1b* allele was deleted. In Cpt1b^{iKO} CMs, *Cpt1b* mRNA was nearly undetectable, confirming the high efficiency of *Cpt1b* ablation (Fig16 B). Expression of *Cpt1a* showed a tendency of compensatory up-regulation, but this elevation was not statistically significant (Fig16 B).

I next evaluated the body weight, heart weight, and of heart weight/body weight ratios of Ctrl and Cpt1b^{iKO} mice, 4 and 8 weeks after TAM injection. While the body weights did not show a significant difference between Ctrl and Cpt1b^{iKO} mice at both time points (Fig16 C), the heart weight and the heart weight/body weight ratio significantly increased in Cpt1b^{iKO} mice but not in Ctrl mice both 4 and 8 weeks after TAM injection (Fig16 C-E). Of note, the heart weight and heart weight/body weight ratios increased further in Cpt1b^{iKO} mice, albeit not significantly, between 4 and 8 weeks 8 weeks after TAM injection, suggesting a tendency of continuous cardiac growth (Fig16 C&D).

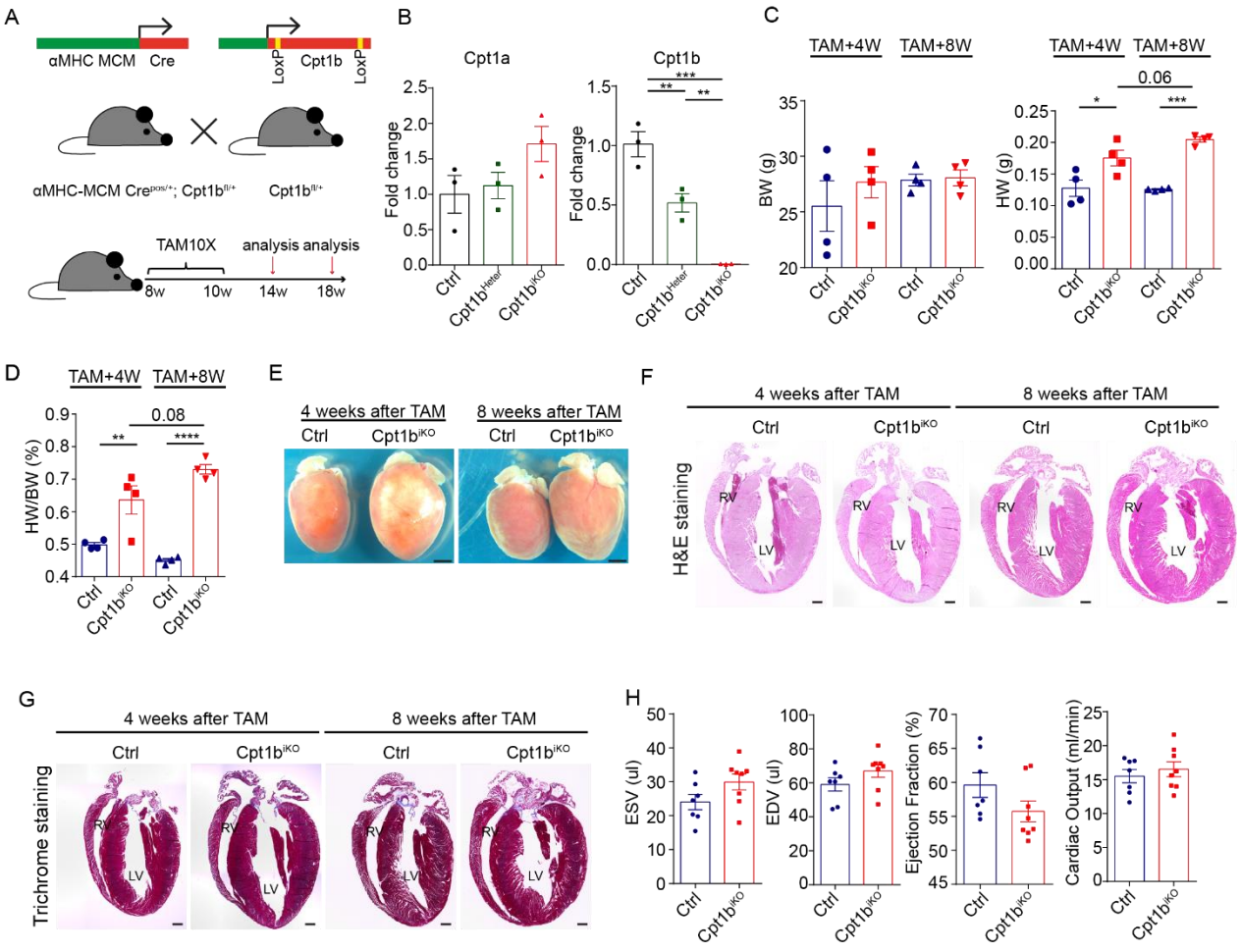

Fig16. Induced ablation of *Cpt1b* in adult CM causes enlargement of heart without impaired cardiac function.

(A) Scheme of the strategy for generation of inducible *Cpt1b* conditional KO mice. The experiment design is depicted in the lower panel. **(B)** RT-qPCR analysis of *Cpt1a* and *Cpt1b* expression in adult CMs isolated from hearts of αMHC-MCM-Cre$^{pos/+}$, Cpt1b$^{+/+}$ or αMHC-MCM-Cre$^{+/+}$, Cpt1b$^{fl/fl}$ (Ctrl); αMHC-MCM-Cre $^{pos/+}$, Cpt1b$^{fl/+}$ (Cpt1b^{Heter}) and aMHC-MCM-Cre $^{pos/+}$, Cpt1b$^{fl/fl}$ (Cpt1b^{iKO}) mice 4 weeks after TAM injection (n=3). *36b4* was utilized as a reference gene. **(C-D)** Analysis of BW, HW, and the ratio of HW/BW of Ctrl and Cpt1b^{iKO} mice 4 and 8 weeks after TAM injection (n=4). **(E)** Macroscopic image of the hearts dissected from Ctrl and Cpt1b^{iKO} mice 4 and 8 weeks after TAM injection. Scale bar: 2 mm. **(F)** H&E staining of paraffin sections from the hearts dissected from Ctrl and Cpt1b^{iKO} mice 4 and 8 weeks after TAM injection (n=3). Scale bar: 600 μm. **(G)** Trichrome staining of paraffin sections from the hearts dissected from Ctrl and Cpt1b^{iKO} mice 4 and 8 weeks after TAM injection (n=3). Scale bar: 600 μm. **(H)** MRI analysis of heart function of Ctrl (n=7) and Cpt1b^{iKO} (n=8) mice 8 weeks after TAM injection. **B-D**, **H**, Error bars represent mean ± s.e.m. Statistical analyses were performed with one-way ANOVA in **B-D**, with unpaired t-test in **H** * p<0.05, ** p<0.01, *** p<0.001, **** p<0.0001. (MRI analysis was assisted by Dr. Astrid Wietelmann)

Although the induced inactivation of *Cpt1b* in adult hearts caused an enlargement, no apparent cardiac dilation was observed (Fig16 F). Instead, the Cpt1b^{iKO} heart showed increased wall thickness in both the left ventricle and septum compared to the Ctrl group 4 and 8 weeks after TAM injection (Fig16 F).

The collagen deposition was also evaluated in heart samples 4 and 8 weeks after TAM injection. Similar to αMHC-Cre induced *Cpt1b* knockout mice, the heart did not show prominent collagen deposition within the myocardium (Fig16 G). To directly evaluate the cardiac function, Ctrl and $Cpt1b^{iKO}$ mice were subjected to MRI analysis 8 weeks after TAM injection. The ESV, EDV, Ejection Fraction, and Cardiac Output were evaluated, respectively. None of these parameters showed a significant difference, suggesting that enlarged $Cpt1b^{iKO}$ hearts maintain normal function (Fig16 H).

9. Enlargement of CMs and expansion of CM numbers contribute to the enlargement of heart in $Cpt1b^{iKO}$ mice

Enlargement of $Cpt1b^{iKO}$ heart may be attributed to cell size enlargement, CM number expansion, or both. To evaluate the size of CMs, I performed WGA staining on paraffin sections from Ctrl and $Cpt1b^{iKO}$ hearts 8 weeks after TAM injection, and quantified the cell surface area (Fig17 A). After quantification with ImageJ, I found that the individual cell size of CM was increased in $Cpt1b^{iKO}$ hearts (Fig17 B). Cell cycle activity was also evaluated by immunofluorescence staining for Ki67, which is expressed in proliferating cells. Interestingly, the $Cpt1b^{iKO}$ heart contained significantly more Ki67 positive CMs compared to the Ctrl group (Fig17 C&D). To examine whether enhanced cell cycle activity leads to cytokinesis, the total number of CMs was determined after complete disassociation of fixed intact hearts. The CM cell number of Ctrl heart accounted to 0.75 million, similar to adult $Ctrl^{Cre}$ mice (Fig12 F). Interestingly, the total number CMs was dramatically increased to above 1 million in $Cpt1b^{iKO}$ heart, 8 weeks after TAM injection (Fig17 E). These data suggest that similar to the $Cpt1b^{cKO}$ heart, both enlarged cell size and increased cell number expansion contribute to the enlargement of $Cpt1b^{iKO}$ hearts.

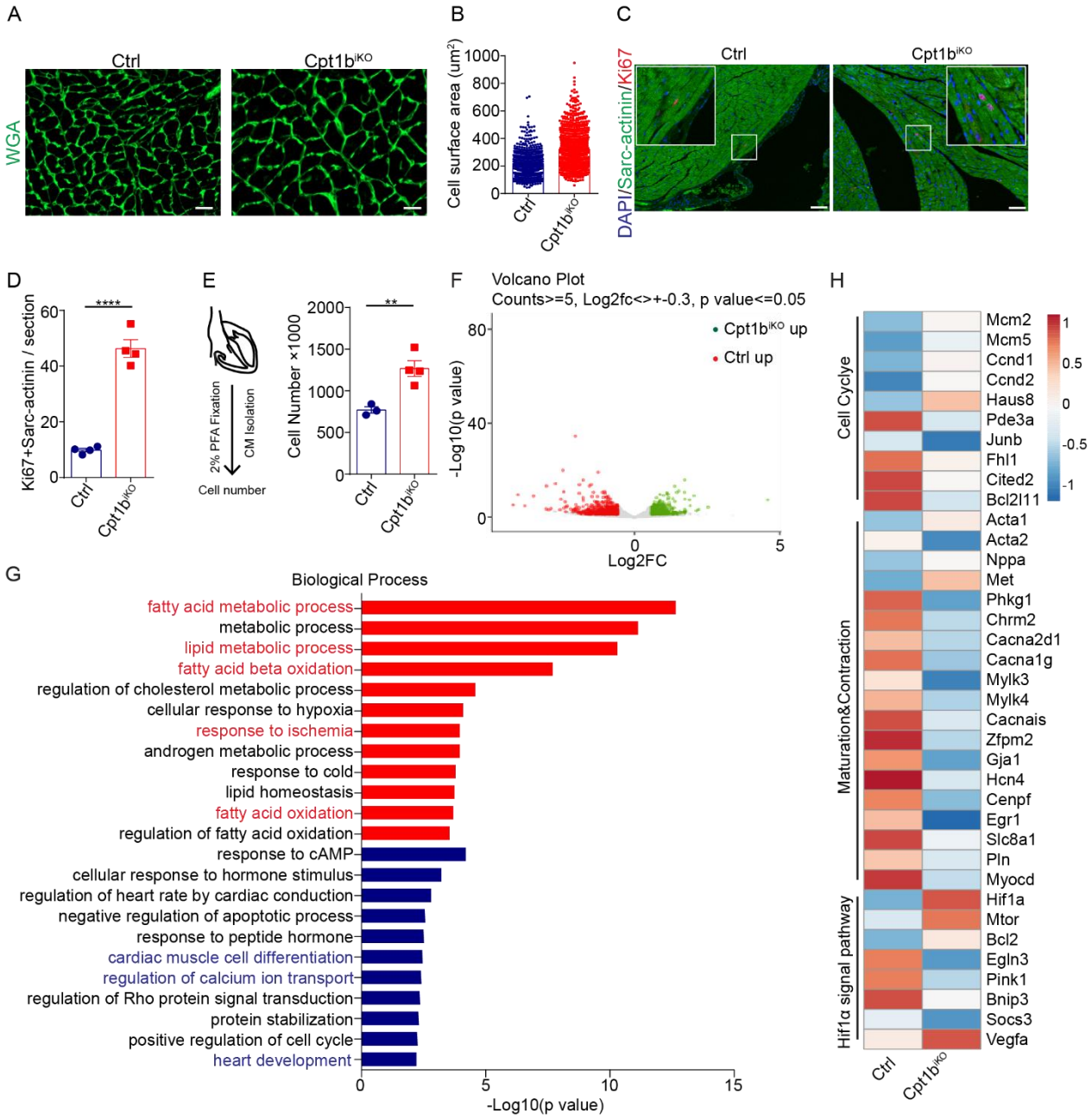

Fig17. Induced ablation of *Cpt1b* in adult CM leads to hyperplasic and hypertrophic growth of CM.

(A-B) Representative IF images and quantification of WGA staining with heart paraffin sections dissected from Ctrl and Cpt1b^{iKO} mice 8 weeks after TAM injection. Scale bar: 20 μm. **(C-D)** IF analysis of Ki67 and Sarc-actinin with heart paraffin section dissected from Ctrl and Cpt1b^{iKO} mice 8 weeks after TAM injection. The number of Ki67+/Sarc-actinin+ CM per heart section was quantified and shown D (n=4). Around 10 sections per heart were quantified. Scale bar: 50 μm **(E)** Quantification of CM number in the hearts dissected from Ctrl and Cpt1b^{iKO} mice 8 weeks after TAM injection (n=4). **(F)** Volcano plot showing the DEGs comparing Ctrl vs. Cpt1b^{iKO} (n=3). Green dots indicate upregulated genes in inducible *Cpt1b* deficient adult CM, and red dots indicate downregulated DEG, respectively. **(G)** GO terms analysis with DEGs comparing Ctrl and Cpt1b^{iKO}. The biological processes enriched with up-regulated genes are represented in red and

the biological processes enriched with down-regulated genes are in blue. **(H)** Heat map of selected DEGs involved in the cell cycle, maturation, and contraction, and the HIF1α signaling pathway based on the Z-score transformed DEseq normalized counts. **B**, **D**, **E**, Error bars represent mean ± s.e.m. Statistical analysis were performed with unpaired t-test in **B**, **D**, **E.** * $p<0.05$, ** $p<0.01$, *** $p<0.001$, **** $p<0.0001$. (NGS experiment was done with the help of Dr. Stefan Guenther, RNA-seq data analysis was assisted by Dr. Carsten Künne)

To investigate transcriptional changes after *Cpt1b* ablation in adult CM, RNA-seq was performed using RNA extracted from Ctrl and Cpt1b^{iKO} CMs. A total of 1432 DEGs (709 genes up-regulated and 723 genes down-regulated) were identified by bioinformatics analysis (Fig17 F). Gene ontology analysis revealed that up-regulated genes were mainly associated with fatty acid metabolism, lipid metabolism, and fatty acid oxidation (Fig17 G). I assume that the up-regulation of these genes might be a compensatory response after FAO inhibition in the adult CMs. Interestingly, down-regulated genes were enriched in pathways related to cardiac muscle cell differentiation, calcium ion transport, and heart development (Fig17 G). Specific pathways over-represented among DEGs were dissected to gain a deeper insight into the change of transcriptional networks, indicating increased expression of cell cycle genes and enhanced Hif1 pathway activity and decreased expression of cardiac maturation genes (Fig17 H). Taken together, these data suggest that induced inactivation of *Cpt1b* converts the fully differentiated CMs into an immature state.

10. Induced inactivation of *Cpt1b* in adult CM reduces myocardial I/R damage

Compared with the Cpt1b^{cKO} mouse line, in which *Cpt1b* is inactivated as early as in embryonic stage, the inducible *Cpt1b* KO model is more clinically relevant since it can be used to induce FAO inhibition specifically in adult animals and investigate its impact on heart injury repair and regeneration in response to myocardial injury. Therefore, I/R surgery was performed 4 weeks after TAM injection and scar formation was evaluated by Trichrome staining 3 weeks after surgery. Similar to the finding in Cpt1b^{cKO} mice, I/R injury-induced fibrotic scar in Cpt1b^{iKO} heart was significantly reduced (Fig18 A). Quantification results confirmed that the fibrotic areas before (absolute) or after (presented as a percentage) normalization to heart section size were dramatically reduced in the Cpt1b^{iKO} heart (Fig18 B&C).

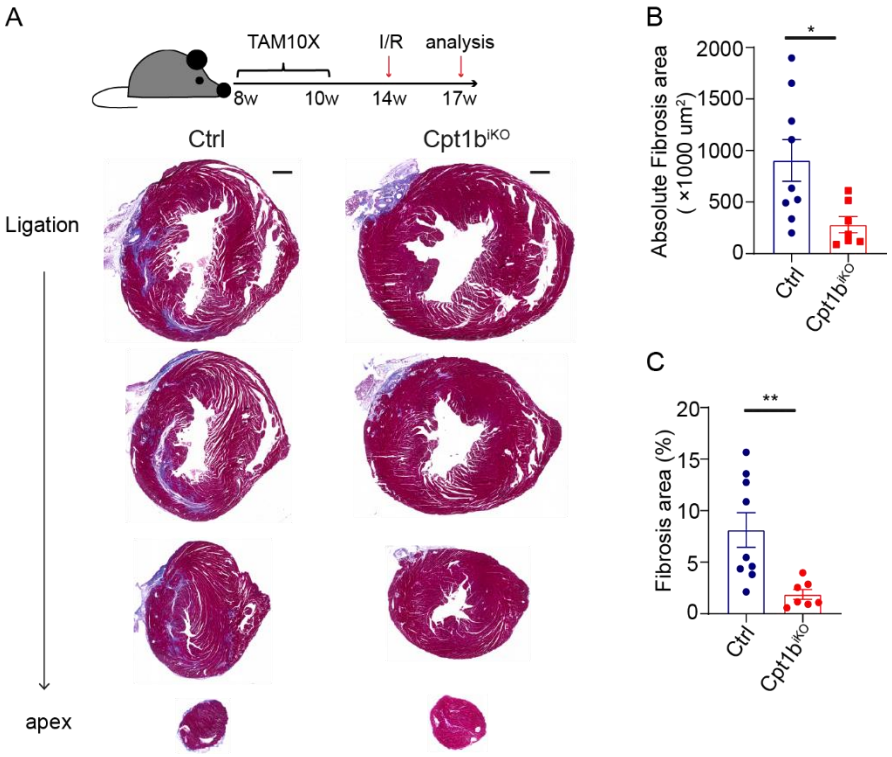

Fig18. Inducible ablation of *Cpt1b* in the adult CMs reduces myocardial infraction damage induced by I/R.

(A-C) Trichrome staining of heart paraffin sections from Ctrl (αMHC-MCM-Cre$^{pos/+}$, Cpt1b$^{+/+}$ or αMHC-MCM-Cre$^{+/+}$, Cpt1b$^{fl/fl}$; n=9) and Cpt1b^{iKO} (n=7) mice 3 weeks after I/R injury (A). Schemes depicting the experimental procedure are presented in the upper panels. Quantification of scar area is shown in B and C. Scale bar: 600 µm. **B-C:** Error bars represent mean ± s.e.m. Statistical analysis was performed with an unpaired t-test in **B-C**, * p<0.05, ** p<0.01. (I/R surgery was done with the help of Marion Wiesnet)

11. FAO is required to maintain CM maturity

Since *Cpt1b* deficiency in the embryonic and adult stages caused similar phenotypes, I assumed that common molecular mechanisms regulating CM proliferation, differentiation and maturation were deregulated in both *Cpt1b* mutant mouse lines. To test this, I performed an integrative analysis of RNAseq datasets obtained from Cpt1b^{cKO} and Cpt1b^{iKO} hearts and identified a total of 471 overlapping DEGs. 172 genes were upregulated and 299 genes were down-regulated in both mutant mouse lines (Fig19 A). Interestingly, the significantly down-regulated genes are mainly involved in biological processes of heart development and positive regulation of cell differentiation (Fig19 B).

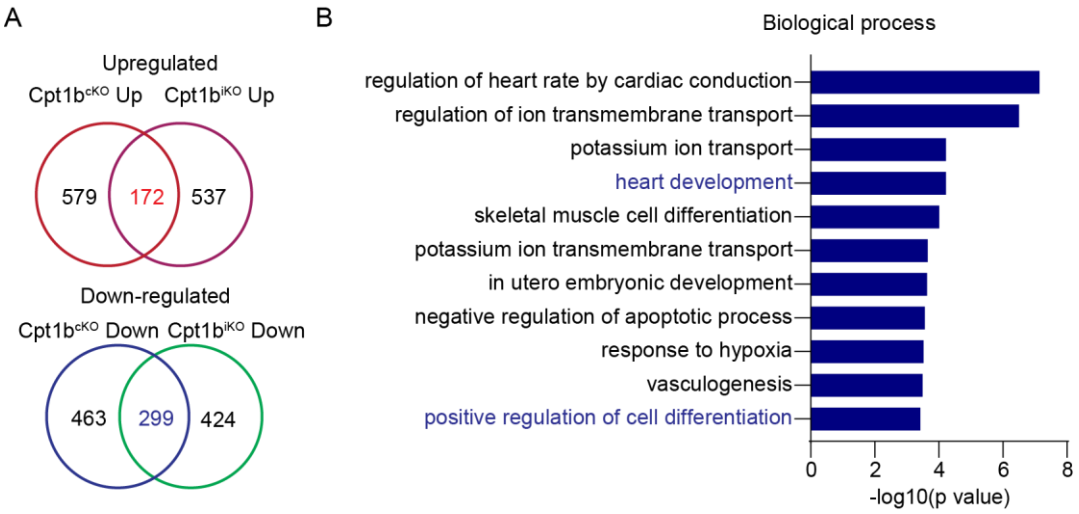

Fig19. Fatty acids oxidation regulates CM lineage commitment by regulating CM maturation

(A) Overlap of up-regulated (upper panel) or down-regulated (lower panel) genes in Cpt1b^{cKO} and Cpt1b^{iKO} CMs compared to control CMs. **(B**) GO term enrichment analysis of overlapped down-regulated genes in both Cpt1b^{cKO} and Cpt1b^{iKO} CMs.

Altogether, my findings demonstrate that both in the neonatal CM and in fully differentiated adult CM, fatty acid oxidation enhances CM maturation. Inhibition of FAO reduced maturity of CM, characterized by retained hypertrophic and hyperplasic growth even in the adult stage. This relative immature state of CM bestows the Cpt1b^{cKO} and Cpt1b^{iKO} hearts with improved regenerative capacity and enhances resistance to ischemic injury. Thus, I conclude that FAO not only supplies the necessary fuels to generate energy, supporting the pump function of the heart but also maintains CM at a mature state.

12. Loss of *Cpt1b* in CM abrogates FAO oxidation and enhances amino acid metabolism

Fatty acids are the heart's main source of fuel, which contribute ~70% of ATP production in the adult heart under physiologic conditions (Lopaschuk et al., 1991). To track the changes of metabolic profiles after inhibition of fatty acids oxidation, a targeted metabolome was performed using adult CMs isolated from control and *Cpt1b* mutant mice. Since Cpt1b^{cKO} and Cpt1b^{iKO} mice exhibit similar cardiac phenotypes and similar transcriptional alterations, I reasoned that there are common molecular and cellular mechanisms underlying the cardiac phenotypes. Therefore, the experiments in the following section were performed using the Cpt1b^{cKO} mouse line.

Over 500 different metabolites were analyzed in the targeted metabolome analysis. Data are summarized in the volcano plot with the following cutoff: fold of change>2 or fold of change <0.5; p-value ≤ 0.05. The blue dots represent reduced metabolites, mostly Acylcartitines due to the lack of CPT1B; whereas the red dots show increased metabolites in *Cpt1b* deficient adult CMs (Fig20 A). Under physiological conditions, CPT1B supports a shuttle for transporting fatty acids from the cytosol into mitochondria by producing Acylcarnitine with fatty acid CoA and free carnitine. As expected, excessive accumulation of free carnitine was detected in *Cpt1b* deficient adult CMs (Fig20 B). Accordingly, the levels of 24 different kinds of Aclycarnitines are reduced in *Cpt1b* deficient adult CM (Fig20 C). Long-chain fatty acids (with carbon length from 13 to 21, LCFA) are the primary substrates for energy production in adult CM. Aclycarnitines with carbon numbers up to 19 were measured individually in the targeted metabolome analysis. Notably, among the significantly reduced Aclycarnitines, long-chain Acylcarnitines are most dramatically reduced (from C14 to C18) (Fig20 C). Medium-chain Aclycarnitines (C6 to C12) are also reduced in *Cpt1b* deficient adult CM (Fig20 C). In conclusion, *Cpt1b* KO blocks fatty acid oxidation by reducing the substrates' transportation from the cytosol into mitochondria.

Surprisingly, amino acids are strongly after *Cpt1b* ablation in CM. The intracellular levels of 12 out of 21 different amino acids measured in the targeted metabolome analysis were increased in *Cpt1b* deficient adult CM, including Asparagine, Arginine, Aspartate, Citrulline, Glycine, Histidine, Methionine, Phenylalanine, Threonine, and Valine, Leucine, and Isoleucine (Fig20 D). This result indicates that increased amino acid catabolism might compensate for decreased levels of TCA intermediate metabolites derived from FAO, thereby maintaining ATP production after inhibition of fatty acid utilization.

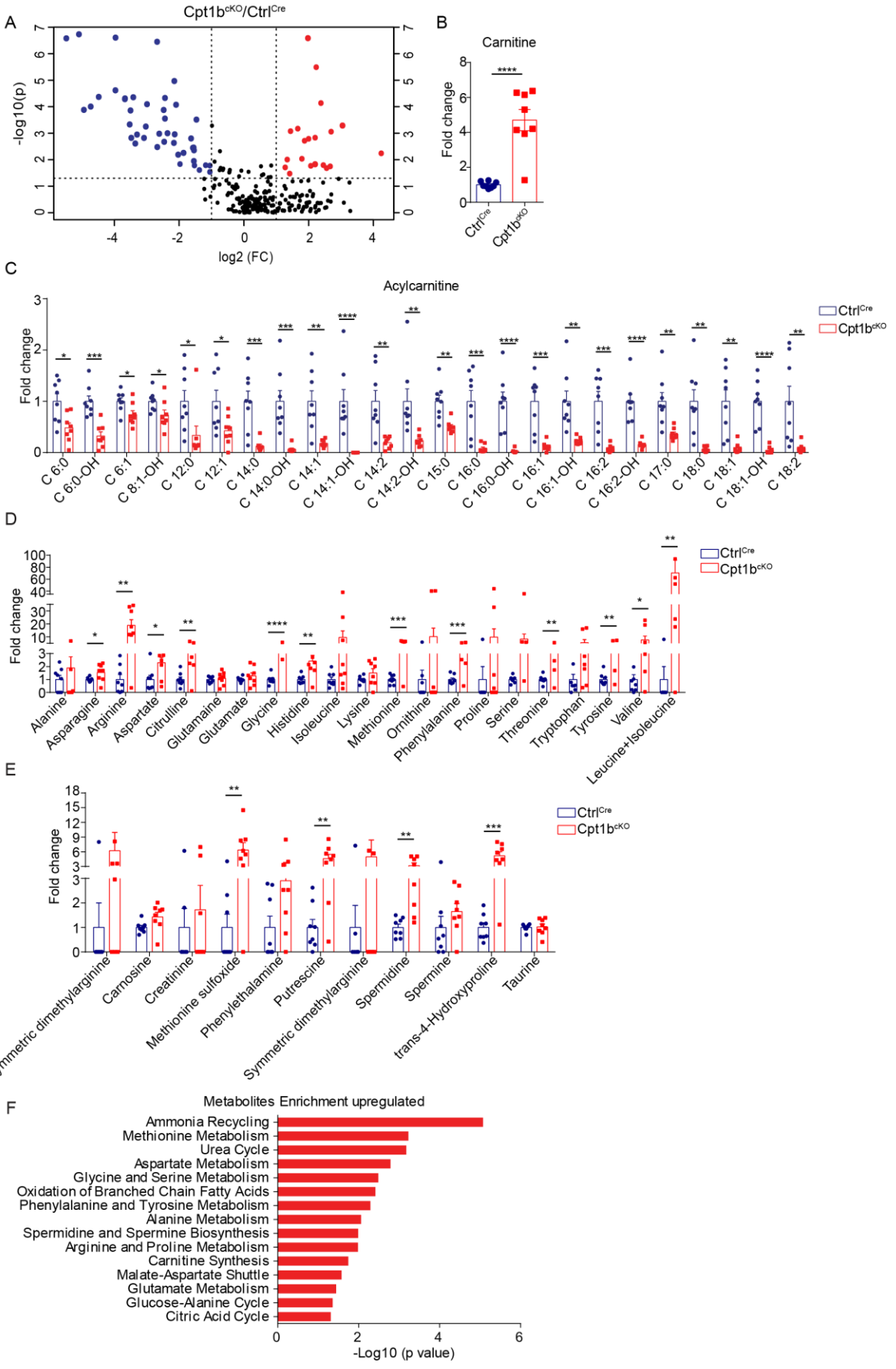
A
Cpt1b^{cKO}/Ctrl^{Cre}
-log10(p)
log2 (FC)
B
Carnitine
Fold change
Ctrl^{Cre}
Cpt1b^{cKO}
C
Acylcarnitine
Fold change
Ctrl^{Cre}
Cpt1b^{cKO}
C 6:0
C 6:0-OH
C 6:1
C 8:1-OH
C 12:0
C 12:1
C 14:0
C 14:0-OH
C 14:1
C 14:1-OH
C 14:2
C 14:2-OH
C 15:0
C 16:0
C 16:0-OH
C 16:1
C 16:1-OH
C 16:2
C 16:2-OH
C 17:0
C 18:0
C 18:1
C 18:1-OH
C 18:2
D
Fold change
Ctrl^{Cre}
Cpt1b^{cKO}
Alanine
Asparagine
Arginine
Aspartate
Citrulline
Glutamine
Glutamate
Glycine
Histidine
Isoleucine
Lysine
Methionine
Ornithine
Phenylalanine
Proline
Serine
Threonine
Tryptophan
Tyrosine
Valine
Leucine+Isoleucine
E
Fold change
Ctrl^{Cre}
Cpt1b^{cKO}
Asymmetric dimethylarginine
Carnosine
Creatinine
Methionine sulfoxide
Phenylethalamine
Putrescine
Symmetric dimethylarginine
Spermidine
Spermine
trans-4-Hydroxyproline
Taurine
F
Metabolites Enrichment upregulated
Ammonia Recycling
Methionine Metabolism
Urea Cycle
Aspartate Metabolism
Glycine and Serine Metabolism
Oxidation of Branched Chain Fatty Acids
Phenylalanine and Tyrosine Metabolism
Alanine Metabolism
Spermidine and Spermine Biosynthesis
Arginine and Proline Metabolism
Carnitine Synthesis
Malate-Aspartate Shuttle
Glutamate Metabolism
Glucose-Alanine Cycle
Citric Acid Cycle
-Log10 (p value)

Fig20. Fatty acid oxidation is blocked but amino acid metabolism is enhanced in *Cpt1b* deficient CMs.

(A) Volcano plot showing deregulated metabolites identified by targeted metabolome analysis of adult CM isolated from 10-week-old $Ctrl^{Cre}$ and $Cpt1b^{cKO}$ mice (n=8). Red dots indicate increased metabolites and blue dots show reduced metabolites in $Cpt1b^{cKO}$ CMs compared to $Ctrl^{Cre}$ CMs. **(B-E)** Quantification of free carnitine (B), acylcarnitine (C), amino acids (D), biogenic amines (E) in adult CMs isolated from 10-week-old $Ctrl^{Cre}$ and $Cpt1b^{cKO}$ mice. **(F)** Metabolites enrichment assay of elevated metabolites in adult $Cpt1b^{cKO}$ CMs. **B-E:** Error bars represent mean ± s.e.m. **B-E:** statistical analysis was performed with unpaired t-test in **B-E**. * $p<0.05$, ** $p<0.01$, *** $p<0.001$, **** $p<0.0001$. (Targeted metabolome experiment was done with the help of Dr. Sven Zukunft)

In addition, the levels of biogenic amines including methionine sulfoxide, phenylethylamine, putrescine, spermidine, and trans-4-Hydroxyproline are increased in *Cpt1b* deficient adult CM (Fig20 E). The deregulated metabolites were subjected to enrichment assay to determine affected metabolic pathways. Interestingly, reduced metabolites were not enriched in any specific pathway, whereas up-regulated metabolites were significantly enriched in pathways associated with amino acid metabolism (Fig20 F). Ammonia recycling and Urea cycle were among the most significantly enriched pathways, implying enhanced amino acid synthesis from by-products of cellular metabolism after inhibition of fatty acid oxidation. Moreover, the spermidine and spermine biosynthesis pathway was also significantly up-regulated. As previous study showed that spermidine induces protein breakdown and rejuvenates adult CM in old animals, suggesting that the breakdown of proteins might also contribute to the elevated amino acid levels in *Cpt1b* deficient adult CM (Eisenberg et al., 2016). Thus, I conclude that once the fatty acid utilization was inhibited after *Cpt1b* ablation, amino acids derived from protein breakdown or metabolic recycling enter into the TCA cycle to compensate for the absence of fatty acid-derived acetyl-coA in maintaining energy production.

13. CM-specific *Cpt1b* ablation does not cause lipotoxicity in the heart

A previous study showed that fatty acids could not be oxidized in MCK-Cre mediated *Cpt1b* knockout mice, leading to accumulation of fatty acids in the cytosol, formation of lipid droplets, and lipotoxicity-induced CM apoptosis (Haynie et al., 2014). However, this lipotoxic effect was not observed in $Cpt1b^{cKO}$ mice. No significant change of 15 different diglycerides and 36 different kinds of triglycerides analyzed in the targeted metabolome was observed in *Cpt1b* deficient CMs (Fig21 A-C). Compared to LCFA (C13-21), very-long-chain fatty acids (C>22, VLCFA) cannot be metabolized in the mitochondria but can be broken down to medium-chain fatty acids (MCFA) through β-oxidation in

the peroxisome. MCFA can further serve as substrates in a CPT1-independent manner in energy metabolism. To check whether VLCFA catabolism contribute to CPT1-independent energy production, the levels of CoA thioesters of VLCFA were analyzed. The levels of CoAs with >20 carbons did not show a significant difference between $Ctrl^{Cre}$ and $Cpt1b^{cKO}$ groups, indicating no obvious compensatory energy metabolism in the peroxisome (Fig21 D). These results imply that once fatty acids utilization is inhibited in CM, the uptake of fatty acids is reduced by an unclear negative feedback loop.

Interestingly, the levels of Methylamalonyl-CoA and Propionyl-CoA, intermediate metabolites of branched amino acid (BCAA) breakdown, were dramatically increased in *Cpt1b* ablated adult CM. This finding indicates that conversion of BCAA into acyl-CoA derivatives, which subsequently enter the TCA cycle, may compensate for energy metabolism when FAO is inhibited (Fig21 D).

To directly exclude lipotoxicity-induced apoptosis in the $Cpt1b^{cKO}$ heart, I performed a TUNEL assay using heart paraffin section from adult animals. DNase-treated sections were utilized as a positive control, in which TUNEL positive signals, as shown in red and merged with DAPI signals, were clearly detected. No TUNEL assay positive nuclei were found in heart paraffin sections from either $Ctrl^{Flox}$ or $Cpt1b^{cKO}$ mice (Fig21 E). This result further corroborates that *Cpt1b* ablation in CM does not cause lipid droplet formation and lipotoxicity-induced cell death.

To better understand the molecular mechanism regulating the fatty acid metabolism in the *Cpt1b* deficient heart, the expression of related genes was checked in the transcriptome dataset. Surprisingly, the mRNA levels of fatty acid transporters (*CD36*, *Slc27a1*, *Slc27a4*, *Fabp3*, *Fabp4*, and *Fabp5*) localized on the cell surface did not change in $Cpt1b^{cKO}$ CM compared with $Ctrl^{Cre}$ CMs (Data not shown). However, the expression of lipoprotein lipase (LPL) was dramatically decreased in *Cpt1b* KO adult CM (Fig21 F). Due to the low dissolvability under physiological conditions, LCFAs are transported within the circulation as triglycerides or albumin-bound form. LPL, which is mainly secreted by adult CM and localizes on the endothelial cell surface towards the vessel lumen, supports release of LCFA from triglycerides and facilitates uptake and transportation of fatty acids into the endothelial cell in the cardiac vasculature. Therefore, decreased expression of *Lpl* in the *Cpt1b* deficient adult CM might reduce uptake of circulating fatty acids, thereby avoiding the pathological accumulation of fatty acids in the cytosol.

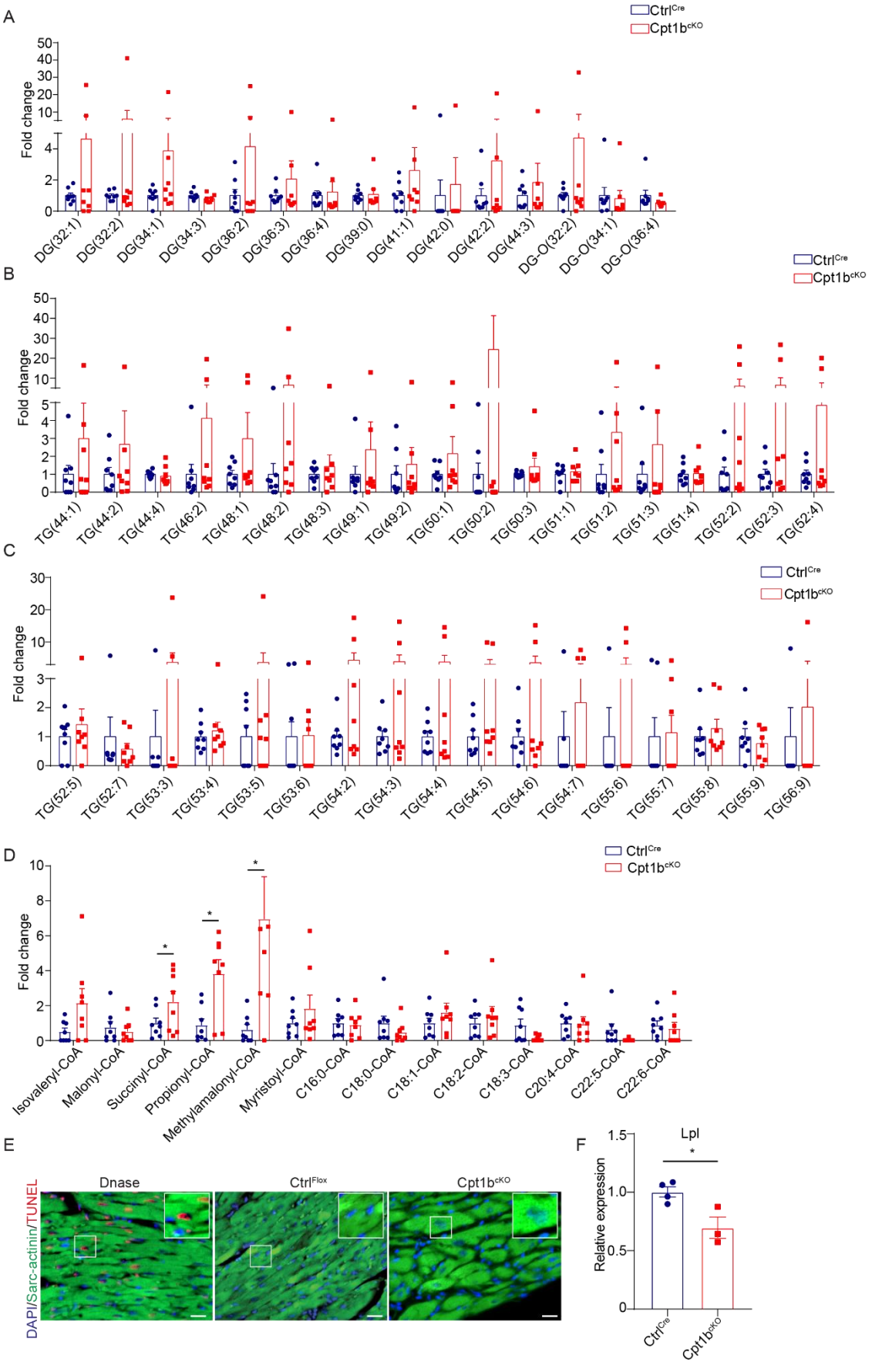
A
Ctrl^Cre
Cpt1b^cKO
Fold change
DG(32:1)
DG(32:2)
DG(34:1)
DG(34:3)
DG(36:2)
DG(36:3)
DG(36:4)
DG(39:0)
DG(41:1)
DG(42:0)
DG(42:2)
DG(44:3)
DG-O(32:2)
DG-O(34:1)
DG-O(36:4)
B
TG(44:1)
TG(44:2)
TG(44:4)
TG(46:2)
TG(48:1)
TG(48:2)
TG(48:3)
TG(49:1)
TG(49:2)
TG(50:1)
TG(50:2)
TG(50:3)
TG(51:1)
TG(51:2)
TG(51:3)
TG(51:4)
TG(52:2)
TG(52:3)
TG(52:4)
C
TG(52:5)
TG(52:7)
TG(53:3)
TG(53:4)
TG(53:5)
TG(53:6)
TG(54:2)
TG(54:3)
TG(54:4)
TG(54:5)
TG(54:6)
TG(54:7)
TG(55:6)
TG(55:7)
TG(55:8)
TG(55:9)
TG(56:9)
D
Isovaleryl-CoA
Malonyl-CoA
Succinyl-CoA
Propionyl-CoA
Methylmalonyl-CoA
Myristoyl-CoA
C16:0-CoA
C18:0-CoA
C18:1-CoA
C18:2-CoA
C18:3-CoA
C20:4-CoA
C22:5-CoA
C22:6-CoA
E
Dnase
Ctrl^Flox
Cpt1b^cKO
DAPI/Sarc-actinin/TUNEL
F
Lpl
Relative expression
Ctrl^Cre
Cpt1b^cKO

Fig21. Fatty acids do not accumulate in adult CM after *Cpt1b* ablation

(A-D) Fold changes of the intracellular levels of diglycerides (A), triglycerides (B&C), and CoAs (D) in $Cpt1b^{cKO}$ CMs compared to $Ctrl^{Cre}$ CMs based on targeted metabolomics profiles. **(E)** TUNEL assay with heart paraffin sections dissected from 20-25 weeks old $Ctrl^{Flox}$ and $Cpt1b^{cKO}$ mice. DNase treated sample was used as a positive control. Scale bar: 20 μm. **(F)** RT-qPCR analysis of *Lpl* expression in adult CMs isolated from hearts of $Ctrl^{Cre}$ and $Cpt1b^{cKO}$ mice. *36b4* was utilized as a reference gene. **A-D, F:** Error bars represent mean ± s.e.m. Statistical analysis was performed with unpaired t-test in **A-D, F**, * $p<0.05$, ** $p<0.01$.

14. αKG excessively accumulates in *Cpt1b* deficient adult CM

As the major substrates for ATP production in adult CM, free LCFA need to be transported into mitochondria and oxidized to produce Acetyl-CoA, which enters into the TCA cycle to produce NADH, FADH2 for oxidative phosphorylation (Fig22 A). To examine whether blockage of the fatty acid transportation into mitochondria has an impact on Acetyl-CoA production, the intracellular level of Acetyl-CoA was measured. Surprisingly, the Acetyl-CoA level was unchanged in $Cpt1b^{cKO}$ CM compared to $Ctrl^{Cre}$ CM, suggesting that compensatory metabolism pathways sufficiently supplement Acetyl-CoA after FAO inhibition (Fig22 B).

Since glycolysis is one of the major compensatory metabolic pathways for energy production after FAO inhibition, I next analyzed glycolysis-related metabolites in control and mutant CMs. Since glucose and fructose are technically difficult to distinguish from each other in metabolomic assays due to their structural similarity, glucose and fructose concentrations are shown together as hexose. I did not find a significant change in hexose 6P level, although a downward trend was observed. However, the pyruvate level was elevated, while the lactate level was significantly reduced in *Cpt1b* deficient CM (Fig22 C). Pyruvate can be either converted to Acetyl-CoA by pyruvate dehydrogenase complex (PDH complex) in mitochondria, or to lactate by lactate dehydrogenase A (LDHA) in the cytosol. The transcriptomic data showed that *Ldha* expression was down-regulated significantly after *Cpt1b* ablation, leading to reduced lactate production (Fig13 E & Fig22 C). Overall, these findings indicate that enhanced glycose oxidation compensates, at least partially, for the energy production following FAO inhibition.

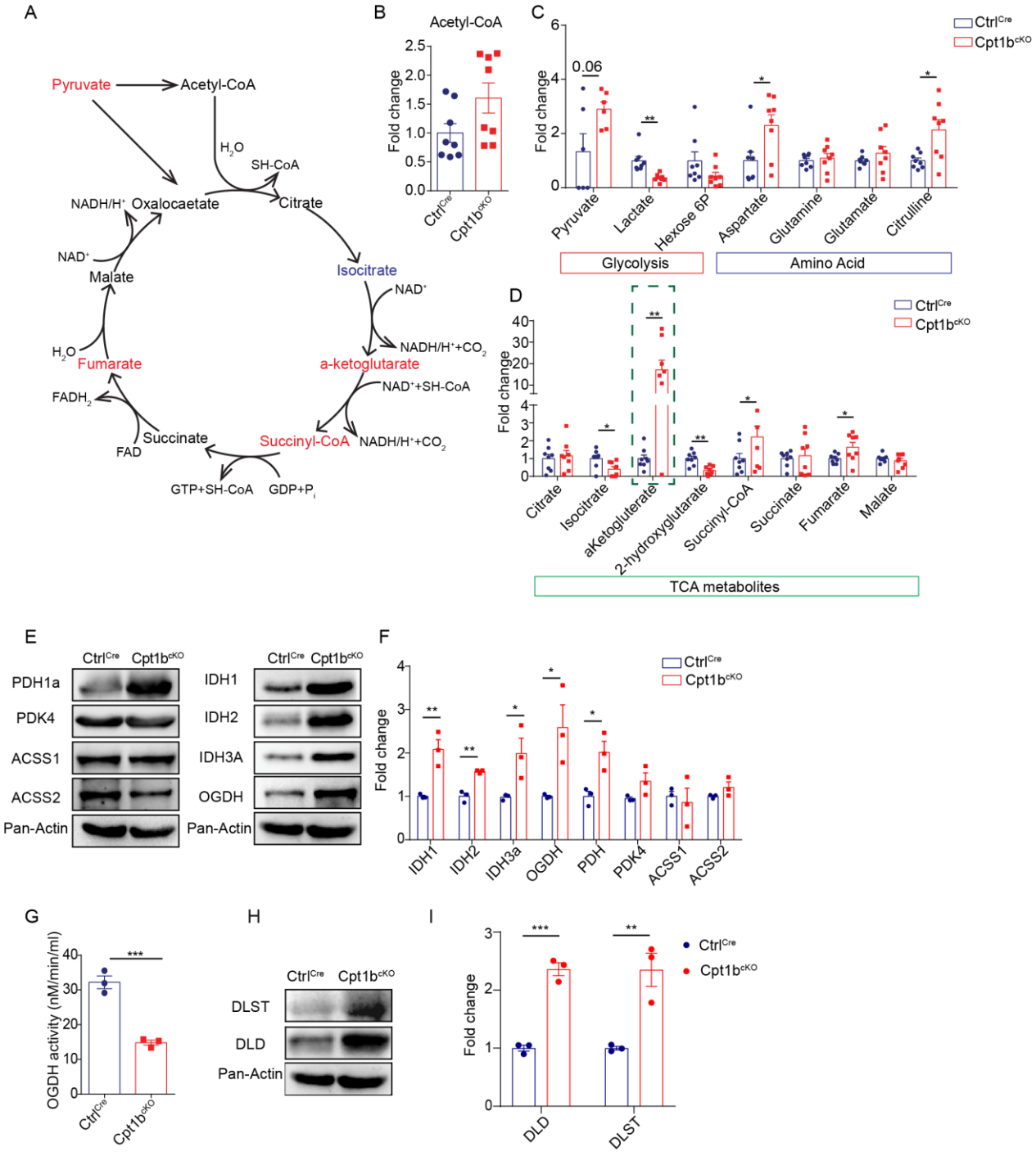

Fig22. αKG accumulates in *Cpt1b* deficient adult CM

(A) TCA cycle showing deregulated metabolites, red color represents enriched metabolites, blue indicates reduced metabolites comparing Ctrl^{Cre} and Cpt1b^{cKO}. **(B-D)** Quantification of Acetyl-CoA (B), glycolysis-associated metabolites and amino acids (C), and TCA cycle-associated metabolites (D) in adult CMs isolated from 10-week-old Ctrl^{Cre} and Cpt1b^{cKO} mice. **(E-F)** Western blot analysis of enzymes involved in acetyl-CoA production and TCA cycle enzymes in CMs isolated from 10-week-old Ctrl^{Cre} and Cpt1b^{cKO} mice (n=3). **(G)** OGDH enzymatic activity assay with whole-cell

lysates prepared from 10-week-old $Ctrl^{Cre}$ and $Cpt1b^{cKO}$ mice (n=3). **(H-I)** Western blot to detect the protein levels of the enzymes in αKG dehydrogenase complex in adult $Ctrl^{Cre}$ and $Cpt1b^{cKO}$ CMs (n=3). **B-D, F-G, I:** Error bars represent mean ± s.e.m. Statistical analysis was performed with unpaired t-test in **B-D, F-G, I**. * $p<0.05$, ** $p<0.01$, *** $p<0.001$.

Next, I compared the levels of other TCA metabolites than Acetyl-CoA in $Ctrl^{Cre}$ and $Cpt1b^{cKO}$ adult CM. Citrate was maintained at a similar level between $Ctrl^{Cre}$ and $Cpt1b^{cKO}$ CMs, while the level of its downstream intermediated metabolite, isocitrate, was significantly reduced after *Cpt1b* inactivation (Fig22 D). Impressively, the levels of αKG increased over 17 times in *Cpt1b* deficient CM compared to control CM. No significant changes were detected in downstream metabolites of αKG in the TCA cycle except succinyl-CoA and fumarate, which showed a moderate increase in *Cpt1b* deficient CM (Fig22 D). The decrease in isocitrate and the increase in αKG indicate enhanced conversion of isocitrate to αKG mediated by isocitrate dehydrogenase complex (IDH complex). Interestingly, the 2HG level was significantly lower in *Cpt1b* deficient CM (Fig22 D).

To dissect the molecular basis for changes of metabolite production, I monitored expression or activity of key enzymes involved in the production of Acetyl-CoA and αKG in adult CM isolated from $Ctrl^{Cre}$ and $Cpt1b^{cKO}$ mice. The protein level of PDH1α, a key component of the PDH complex that converts pyruvate into Acetyl-CoA, was dramatically elevated, while the protein level of PDK4, which inhibits the enzymatic activity of the PDH complex by phosphorylating PDH1α, was not changed in $Cpt1b^{cKO}$ CM compared to control CM (Fig22 E&F). These results provide additional evidence for enhanced glucose oxidation that might compensate for the Acetyl-CoA production after FAO inhibition. The other alternative precursor for Acetyl-CoA production is acetate, which can be converted to Acetyl-CoA by ACSS1 and ACSS2. The levels of these enzymes were not changed, suggesting a minor contribution to Acetyl-CoA production (Fig22 E&F).

Furthermore, I examined the protein levels of IDHs, which convert isocitrate into αKG in control and mutant CMs by western blots. All three IDHs with different subcellular localization, namely IDH1, localized in the cytosol, IDH2 in the mitochondria, IDH3a in the mitochondria and nuclei, were significantly up-regulated in *Cpt1b* deficient CM，indicating that enhanced αKG production is not limited to mitochondria (Fig22 E&F). The protein level of OGDH, the enzyme converting αKG into succinyl-CoA in the TCA cycle, was dramatically up-regulated (Fig22 E&F), but the enzymatic activity of the OGDH complex was significantly reduced (Fig22 G). To unveil the reason for reduced enzymatic activity, protein levels of other OGDH complex components were analyzed. Western blot results uncovered that dihydrolipoyl succinyltransferase (DLST) and dihydrolipoyl dehydrogenase

(DLD) remained unchanged in *Cpt1b* deficient CM, suggesting that reduced enzymatic activity is not due to the lack of individual components of the OGDH complex (Fig22 H&I). According to previous reports, the intermediate metabolites of BCAA breakdown e.g., KMV, KIC, and KIV block the enzymatic activity of the OGDH complex, (Patel, 1974). These metabolites were not included in the targeted metabolome assay, but I found an increase of other intermediate metabolites of BCAA breakdown in *Cpt1b* deficient CM (Fig20 D & Fig21 D), suggesting that the enzymatic activity of OGDH is repressed by the intermediate products of the BCAA breakdown.

15. The global level of H3K4me3 is reduced in *Cpt1b* deficient adult CM

αKG is not only a key intermediate metabolite in the TCA cycle but also serves as an essential substrate for DNA/histone demethylation. Excessive accumulation of αKG level in *Cpt1b* deficient CMs may lead to changes in histone methylations. To analyze potential changes in histone methylation, I performed western blot analysis to monitor the levels of different histone methylations, enriched either in euchromatin or in heterochromatin, in control and *Cpt1b* deficient CM. To reduce the possible background from the cytosol, protein lysates of FACS sorted adult CM nuclei were used for western blots. Among the studied histone methylation markers, H3K9me1, H3K9me2. H3K36me3, H3K79me2, H3K79me3, and H4K20me3 levels were unchanged, while H3K27me3, H4K20me2, and H3K9me3 levels were significantly increased in *Cpt1b* deficient CM (Fig23 A&B). Notably, the level of H3K4me3 was markedly reduced in *Cpt1b* deficient CM, although the levels of H3K4me1 and H3K4me2 were not altered (Fig23 A&B). These findings indicate that one or more members of the KDM5 family of αKG-dependent H3K4me3 demethylases represent potential nuclear effectors, which sense excessively accumulated αKG after FAO inhibition.

To assess potential changes of the expression levels of the histone methyltransferase (KMT) and αKG-dependent histone demethylase (KDM), which may have an impact on methylation levels in *Cpt1b* deficient CM, I analyzed the transcriptome dataset. No significant changes in both KMT and KDM were found, including the KMT2 and KDM5 families that are involved in methylation and demethylation of H3K4me3 (Fig23 C&D). Thus, I conclude that the change of histone methylation pattern in *Cpt1b* deficient CM is primarily attributed to the availability of the co-substrate αKG and that αKG accumulation may enhance KDM5 activity, leading to a global reduction of H3K4me3.

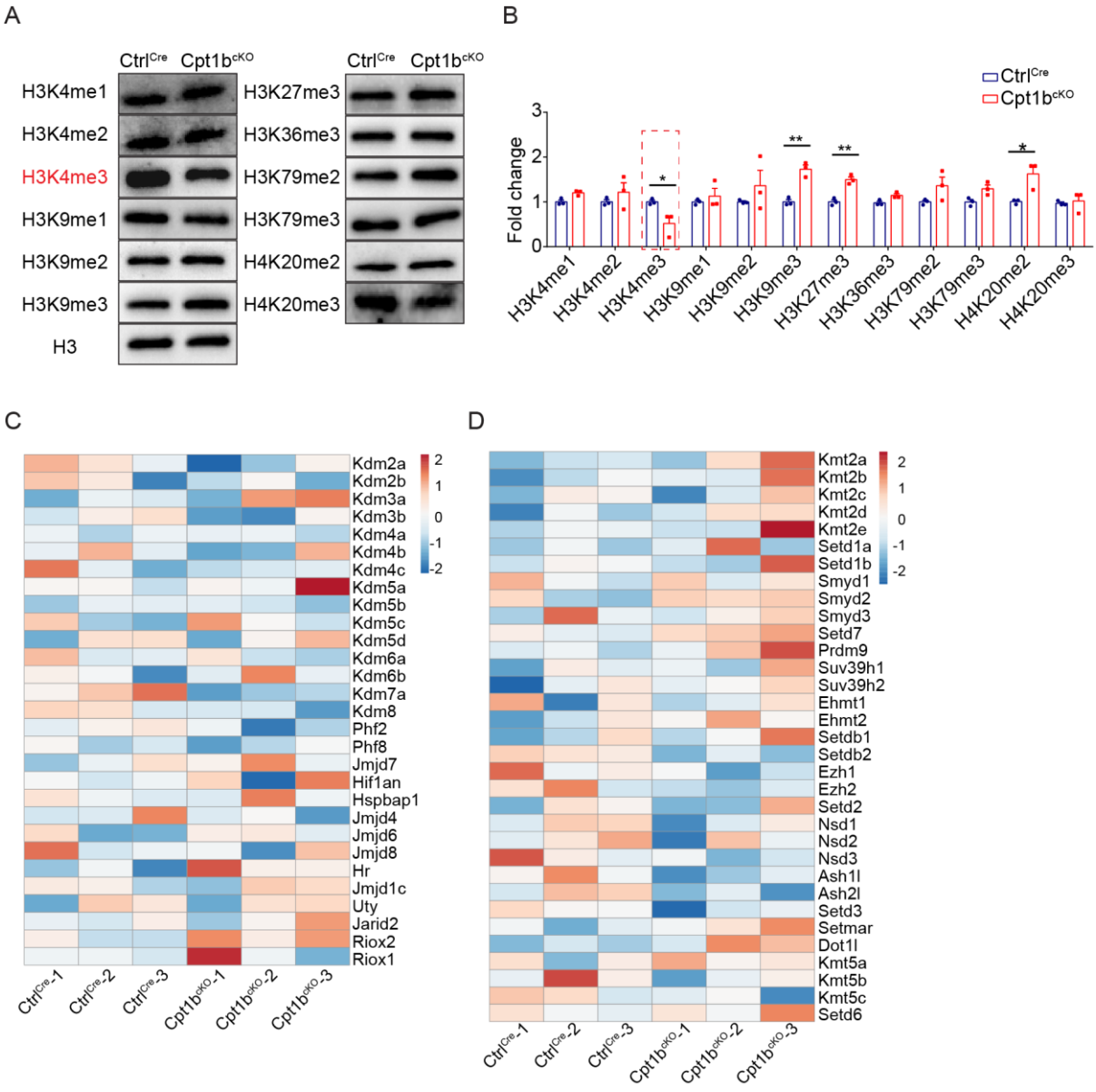

Fig23. Global H3K4me3 level is reduced in *Cpt1b* deficient CM.

(A-B) Western blot analysis of histone methylation markers with FACS sorted CM nuclei isolated from 10- week-old Ctrl^{Cre} and Cpt1b^{cKO} mice. Histone 3 (H3) was used as an internal loading control. Quantification of indicated histone methylation level is shown in B (n=3). **(C-D)** Heat map reflecting the Z-score transformed DEseq normalized RNA-seq counts of selected Jmjc domain-containing histone demethylase (C) and histone methyltransferase (D). **B:** Error bars represent mean ± s.e.m. Statistical analysis was performed with unpaired t-test in **B**, * p<0.05, ** p<0.01.

16. Loss of H3K4me3 is mainly observed in the genes associated with heart development and CM maturation

To identify genes losing H3K4me3 after *Cpt1b* ablation, H3K4me3 ChIP-Seq was performed using cardiac nuclei isolated from the Ctrl^{Cre} and Cpt1b^{cKO} hearts. Analysis of the genome-wide distribution of H3K4me3 in control and mutant CM revealed an enrichment around the TSS region and 5' intragenic region (Fig24 A). This distribution profile is consistent with the pattern of H3K4me3 deposition in the various cell types, indicating H3K4me3 ChIP-seq in this study worked robustly.

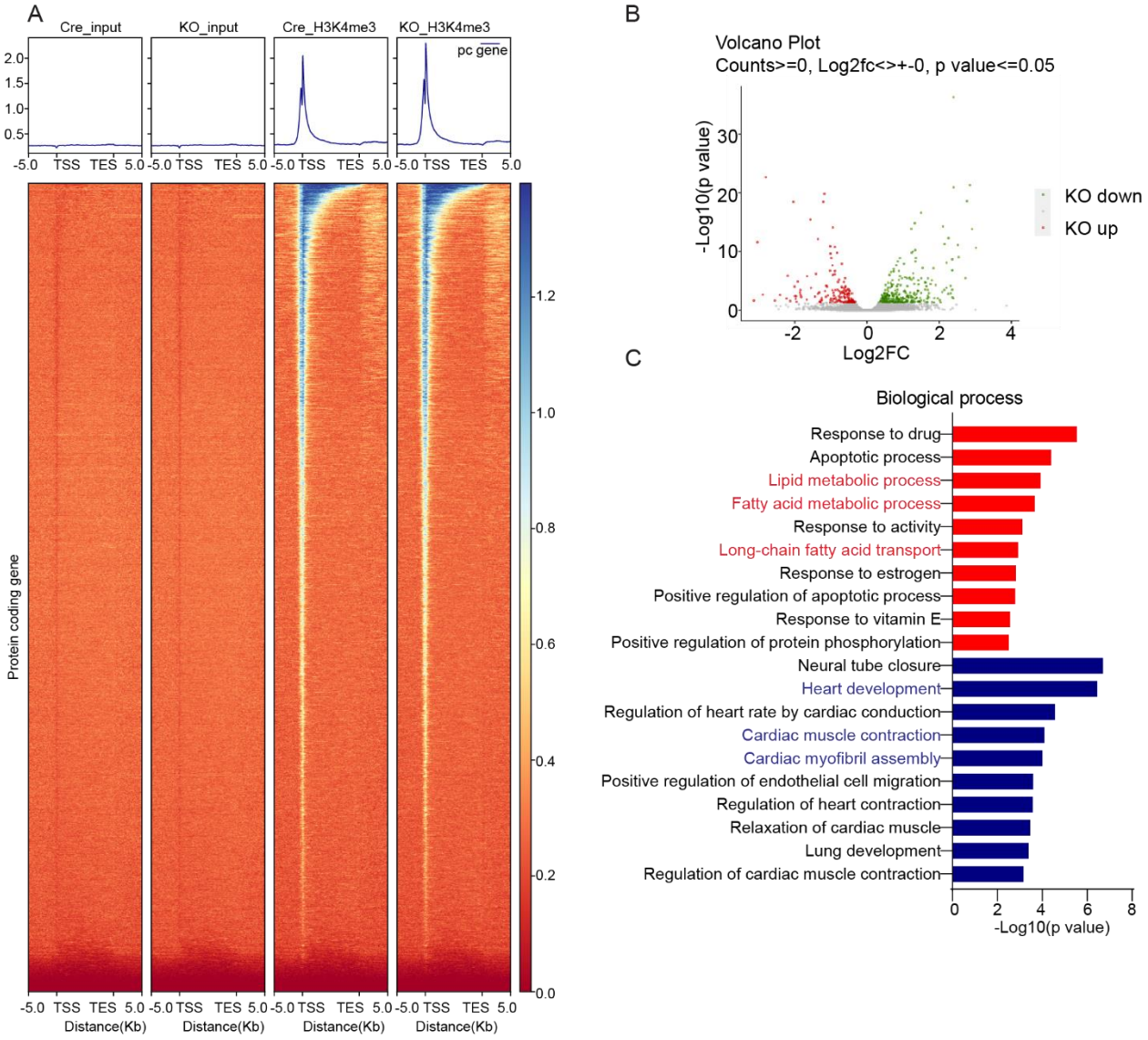

Fig24. H3K4me3 ChIP-seq signals are reduced in genes associated with heart development and maturation after inactivation of *Cpt1b*.

(A-B) Heat map of H3K4me3 ChIP-seq signal within protein-coding genes. Corresponding coverage plots are shown in the top panels. The input samples were utilized as a control for ChIP-seq (A). Volcano plot showing the deregulated peaks comparing $Ctrl^{Cre}$ vs. $Cpt1b^{cKO}$ (n=3). Green dots indicate enriched peaks in *Cpt1b* deficient adult CM, and red dots indicate reduced H3K4me3 deposition, respectively (B). **(C)** The GO terms of genes with differential H3K4me3 peaks in $Cpt1b^{cKO}$ CMs. The biological processes enriched with genes containing up-regulated peaks are represented in red and genes containing down-regulated peaks are in blue. (NGS experiment was done with the help of Dr. Stefan Guenther, ChIP-seq data analysis was assisted by Dr. Carsten Künne)

By applying the following cutoff: counts >0, Log_2 (fold of change Mut/Ctrl) < or >0, and p value ≤ 0.05, a total of 945 significantly deregulated peaks on protein-coding genes were identified in $Cpt1b^{cKO}$ CMs. 467 peaks were significantly upregulated, whereas 478 peaks were dramatically downregulated (Fig24 B). GO term enrichment analysis using a web-based tool (DAVID) revealed that genes with increased H3K4me3 deposition were enriched in pathways for lipid metabolic process, fatty acid metabolic process, and the long-chain fatty acid transport, which were also transcriptionally activated (Fig24 C). Interestingly, genes with reduced H3K4me3 deposition were enriched in terms of heart development, cardiac muscle contraction, and cardiac myofibril assembly, which are key pathways involved in CM maturation and contractile function (Fig24 C).

17. CM-specific identity genes containing H3K4me3 broad domains are demethylated and transcriptionally repressed after *Cpt1b* ablation

Bioinformatics analysis of genes with reduced H4K4me3 deposition showed that H3K4me3 deposition near the TSS and 5' intragenic region was dramatically reduced (Fig25 A). Interestingly, cell identity genes in various species and cell types are marked by broad domains of H3K4me3 at 5' intragenic region, which are positively correlated to transcriptional strength (Benayoun et al., 2014; Chen et al., 2015; Sze et al., 2020). To study the correlation of H3K4me3 breadth with cell identity maintenance in CM, I categorized the genes with H3K4me3 peak breadth: genes containing the broadest 25% peaks were defined as the broad group; genes with the narrowest 25% peaks as the narrow group; the rest (25%-75%) as the medium group (Fig25 B). Consistent with previous studies, genes containing broad H3K4me3 peaks had the highest transcription level and were largely involved in pathways such as sarcomere organization, heart development, heart morphogenesis, and cardiac

muscle contraction, all of which are biological processes required for CM cell state/identity maintenance. In contrast, genes containing the narrow peaks were transcribed to a lesser extent and were mainly associated with biological processes such as protein transport and tRNA processing, which are required for the maintenance of basic cellular functions in nearly all cell types (Fig25 C&D).

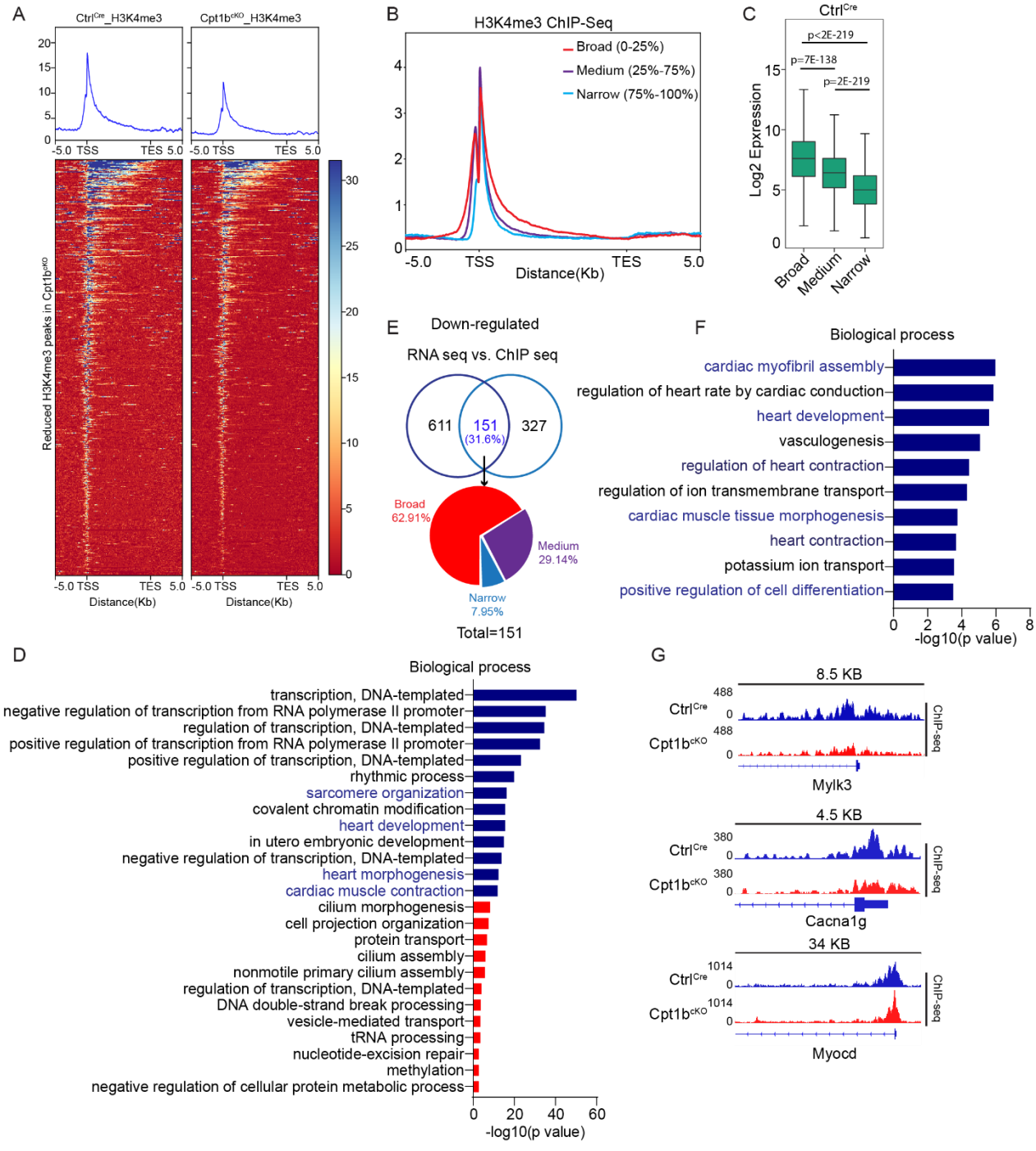

Fig25. A subset of genes containing broad H3K4me3 peaks is demethylated and transcriptionally repressed in *Cpt1b* deficient CMs.

(A) Heat map of genes with downregulated H3K4me3 ChIP-seq signals. Corresponding coverage plots are shown in the top panels. **(B)** Coverage plots of H3K4me3 ChIP-seq signals within genes categorized into three groups based on H3K4me3 peak breadth in wild-type CMs: Broad group containing the top 25% genes with broadest peaks, Narrow group containing the 25% genes with the narrowest peaks, and rest of genes (25-75%) defined as Medium group. **(C)** Box plot showing the expression level of genes with broad, medium, and narrow H3K4me3 peaks in wild-type CMs. **(D)** Biological processes enriched with genes containing Broad and Narrow H3K4me3 peaks. The GO terms enriched with genes containing broad H3K4me3 peaks are represented in blue, while GO terms enriched with the genes containing narrow H3K4me3 peaks are in red. **(E)** Venn diagram showing the overlap between down-regulated genes in RNA-seq and genes with reduced H3K4me3 deposition in Cpt1b^{cKO} compared to Ctrl^{Cre} CMs. The distribution of the overlapped peaks in the Broad, Medium, and Narrow groups is shown in the pie chart. **(F)** GO term analysis of overlapped DEGs using the David tool. **(G)** Genomic snapshots of representative genes associated with CM maturation showing reduced H3K4me3 deposition in Cpt1b^{cKO} CMs. **C**: Error bars represent mean ± s.e.m. Statistical analysis was performed with unpaired t-test in **C**, * p<0.05, ** p<0.01. (ChIP-seq data analysis was assisted by Dr. Carsten Künne)

To better understand the correlation of H3K4me3 demethylation and gene transcription, an integrative analysis of RNA-seq and H3K4me3 ChIP-seq datasets was performed. I identified 151 overlapping genes that contained reduced H3K4me3 signals and were transcriptionally down-regulated in *Cpt1b* deficient CMs (Fig25 E). Moreover, over 62% of these overlapping genes contained broad H3K4me3 peaks (Fig25 E). GO term analysis of overlapping genes disclosed that pathways involved in heart development and contraction-related terms such as cardiac myofibril assembly, heart development, regulation of heart contraction, cardiac muscle tissue morphogenesis, and positive regulation of cell differentiation were over-represented (Fig25 F). H3K4me3 demethylation within several key regulators of CM postnatal development and heart contraction, such as *Mylk3*, *Cacna1g*, and *Myocd,* were visualized in IGV snapshots (Fig25 G). Overall, my findings suggest that CM-specific cell state/identity genes are more susceptible to KDM mediated H3K4me3 demethylation in response to excessive accumulation of αKG in *Cpt1b* deficient CMs.

18. αKG treatment promotes proliferation of neonatal CMs *in vitro*

To directly dissect the link between αKG accumulation, CM proliferation/maturation, and histone methylation, P0-1 neonatal CMs were isolated and treated with cell-permeable αKG. Afterwards, cell cycle activity and histone methylation levels were determined 72-96 hours after αKG treatment. Immunofluorescence staining analysis of Ki67 showed that the percentage of Ki67+ neonatal CM dramatically increased from 3% to around 20% after αKG treatment (Fig26 A). In parallel, the

percentage of CMs that were positive for the late G2/M phase marker pH3 increased significantly from 2.5% to over 10% after αKG treatment (Fig26 B). Moreover, RT-qPCR results showed that expression of genes highly expressed during early stages of CM development, such as *Acta1*, *Nppa*, *Nppb*, and *Myh7*, were significantly increased, whereas late-stage maturation-related markers, such as *Tnni3*, *Cacna1g,* and *Myocd*, were down-regulated after αKG treatment (Fig26 C). Furthermore, I performed western blot analysis to access changes of histone methylation after αKG treatment. Consistent with the *in vivo* data, H3K4me3 was the only histone methylation mark that was significantly reduced, whereas other methylation markers were not changed after αKG treatment (Fig26 D&E). Altogether, these data suggest that the αKG treatment *in vitro* promotes cell proliferation and represses CM maturation, most likely through facilitating H3K4m3 demethylation.

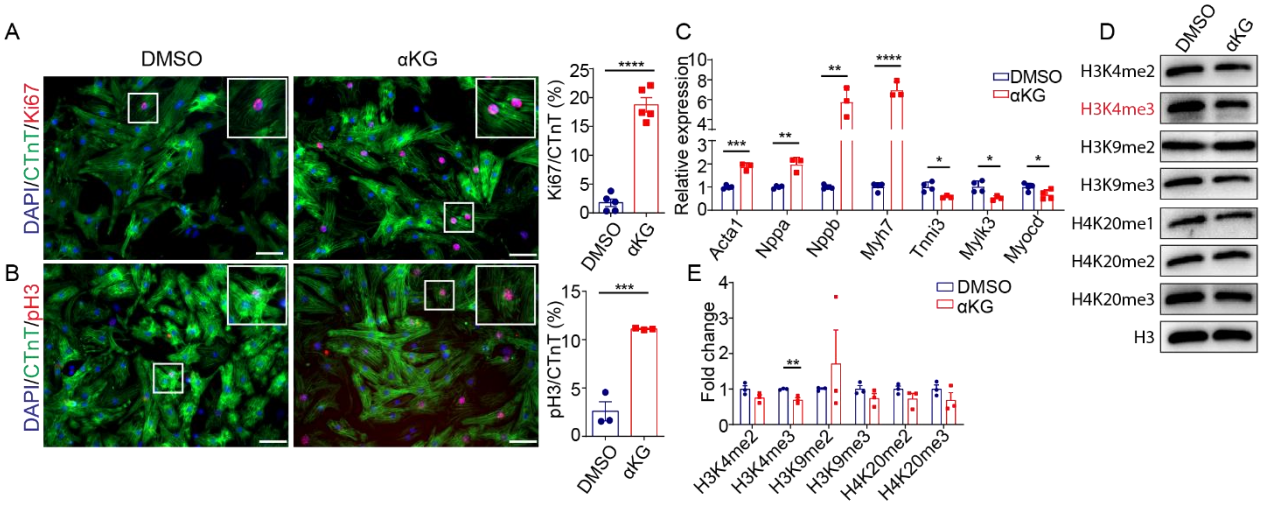

Fig26. αKG treatment induces cell proliferation and reduces H3K4me3 levels in neonatal CMs.

(A-B) IF analysis of Ki67 (A) or pH3 (Ser10) (B) in cTnT+ neonatal CMs (P0-1) after 3 days culture in the presence of DMSO or αKG. Quantification of Ki67+/cTnT+ (n=5) or pH3+/cTnT+ (n=3) is shown in right panel. Scale bar: 50 μm. **(C)** RT-qPCR expression analysis of indicated genes in P0-1 neonatal CMs after 3 days culture in the presence of DMSO or αKG (n=3). *36b4* was utilized as a reference gene. **(D-E)** Western blot analysis of indicated histone methylation markers in P0-1 neonatal CMs after 3 days culture in the presence of DMSO or αKG (D). Quantification of indicated histone methylation level was shown in E (n=3). H3 was used as an internal loading control. **A-C, E**: Error bars represent mean ± s.e.m. Statistical analysis was performed with unpaired t-test in **A-C, E**; * $p<0.05$, ** $p<0.01$, *** $p<0.001$.

19. αKG induced CM proliferation is prevented by inhibition of the histone demethylase KDM5

To test the hypothesis that αKG-dependent enzymes are the nuclear effectors increasing neonatal CM proliferation in response to αKG administration, I treated *in vitro* cultured neonatal CMs with R2HG. R2HG binds competitively to αKG-dependent enzymes and inhibits their enzymatic activity, albeit its binding affinity is lower compared to αKG. Cell cycle activity in CMs treated with αKG, R2HG, and a combination of both was accessed by Ki67 staining. I found that the percentage of Ki67 positive neonatal CMs increased dramatically after αKG treatment, while it remained at similar levels in DMSO and R2HG treated samples (Fig27 A). Notably, the percentage of Ki67+ CMs decreased substantially after combined treatment with αKG and R2GH, although it was still higher than in DMSO-treated cells (Fig27 B). This finding suggests that the pro-proliferative effect of αKG supplementation is counteracted by treatment with R2HG when αKG and R2HG are added at the same concentrations.

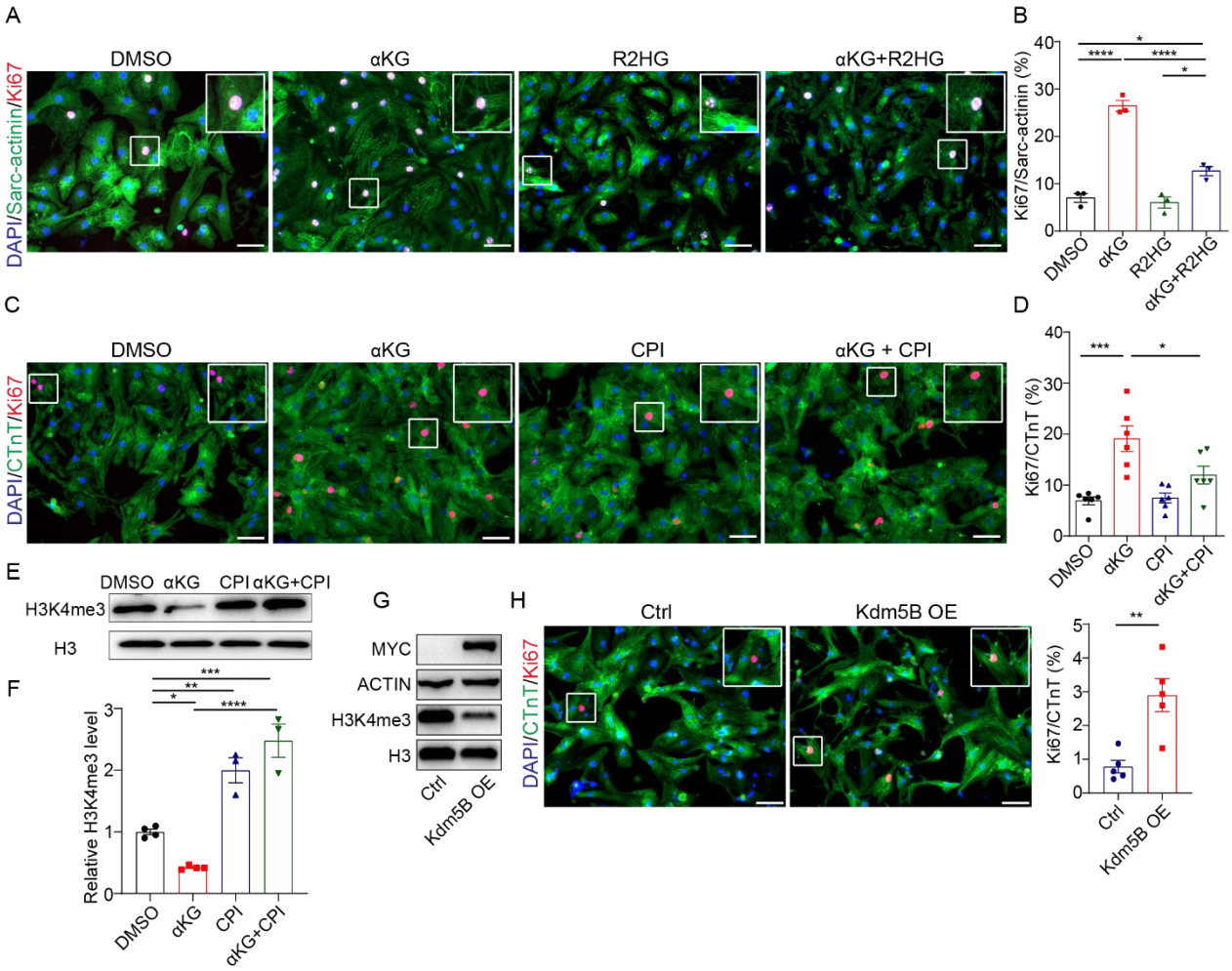

Fig27. R2HG and KDM5 inhibitor (CPI) counteract the pro-proliferative effect of αKG in neonatal CMs.

(A-B) IF analysis of Ki67 in sarc-actinin+ neonatal CMs (P0-1) after 3 days culture in the presence of DMSO, αKG, R2HG and combined αKG with R2HG, respectively (F). Quantification of the Ki67+/sarc-actinin+ CMs was shown in G. Scale bar: 50 μm. **(C-D)** IF analysis of Ki67 in cTnT+ neonatal CMs (P0-1) after 3 days culture in the presence of DMSO, αKG, CPI, and combined αKG with CPI, respectively (C). Quantification of the Ki67+/ cTnT+ CMs was shown in D. Scale bar: 50 μm**. (E-F)** Western blot analysis of H3K4me3 level in P0-1 neonatal CMs after 3 days culture in the presence of DMSO, αKG, CPI, and combined αKG with CPI (E). H3 was used as an internal loading control. Quantification of indicated histone methylation level is shown in F. **(G)** Western blot analysis of MYC and H3K4me3 level in P0-1 neonatal CMs after 96 hours of infection with control or *Kdm5b* overexpression lentivirus. ACTIN and H3 were used as internal loading control. **(H**) IF analysis of Ki67 in cTnT+ neonatal CMs (P0-1) after infection with control or *Kdm5b* overexpression lentivirus. Quantification of the Ki67+/cTnT CMs is shown on the right panel. Scale bar: 50 μm. **B, D, F, H**: Error bars represent mean ± s.e.m. Statistical analysis was performed with one-way ANOVA in **B, D, F;** with unpaired t-test in **H**; * $p<0.05$, ** $p<0.01$, *** $p<0.001$.

To examine whether the suppressive effect of R2GH on cell cycle activity was achieved by suppressing H3K4me3 specific KDMs, I also concomitantly treated neonatal CMs with a H3K4me3 demethylase inhibitor and αKG and analyzed cell cycle activity. There are six αKG-dependent H3K4me3 demethylases, namely KDM2B, KDM5A, KDM5B, KDM5C, KDM5D, and RIOX1. *Roix1* expression is extremely low in CM, excluding a major role in H3K4me3 demethylation in *Cpt1b* deficient CMs. KDM2B demethylates both H3K4me3 and H3K36me2, however, this protein is enriched in the nucleolus and represses the transcription of ribosomal RNA genes. Thus, KDM5 family members (KDM5 A-D), which demethylate both H3K4me2 and H3K4me3 (Kooistra and Helin, 2012), are potential KDMs that may account for reduction of H3K4me3 in CMs when αKG-levels are increased. Thus, the KDM5 inhibitor CPI, which specifically blocks all KDM5 family members was selected for further experiments.

Cell cycle activity of CMs treated with αKG, CPI, and combination of both αKG was assessed by Ki67 staining. As expected, αKG treatment markedly increased proliferation of neonatal CMs. CPI treatment itself did not has an obvious effect on CM proliferation (Fig27 C&D). However, when neonatal CMs were concomitantly treated with αKG and CPI, the percentage of Ki67 positive CM was dramatically reduced to control levels (Fig27 C&D). Of note, the global level of H3K4me3 was reduced after αKG treatment, but increased in both CPI and αKG+CPI treated CMs, indicating that the enzymatic activity of KDM5 demethylases was sufficiently blocked by the CPI treatment (Fig27 E&F). In conclusion, αKG supplement increases CM proliferation by enhancing the enzymatic activity of the KDM5 family.

20. *Kdm5b* overexpression promotes CM proliferation

Of the four KDM5 family members, *Kdm5c* is localized on the X chromosome, while *Kdm5d* is localized on the Y chromosome. Since the cardiac phenotypes after *Cpt1b* ablation were not gender-dependent, I assume that KDM5C and KDM5D might not be the main KDMs to erase H3K4me3 in mutant CMs. KDM5A and KDM5B display functional redundancy and play important roles in heart development (Zaidi et al., 2013) , therefore I speculate that KDM5A and/or KDM5B are potential nuclear effectors sensing increased αKG level in *Cpt1b* mutant CMs. To prove this hypothesis, I infected *in vitro* cultured neonatal CMs with lentivirus expressing a scrambled control sequence or *Kdm5B* and accessed the cell cycle activity 96 hours after infection by Ki67 staining. Notably, H3K4me3 levels were strongly reduced and the percentage of Ki67 positive neonatal CMs increased from 1% to around 3% after overexpression of *Kdm5b*, which recapitulates the pro-proliferative effect of αKG (Fig 27 G&H).

21. Excessive accumulation of αKG alters DNA methylation pattern in *Cpt1b* mutant CMs

αKG also serves as an essential co-substrate for TET-mediated DNA demethylation. Therefore, I analyzed global levels of 5mC and its oxidized derivatives in control and *Cpt1b* mutant CMs by dot blot experiments. Interestingly, 5mC levels were elevated after *Cpt1b* ablation in adult CM. 5hmC levels were dramatically reduced, 5fC levels were unchanged, and surprisingly, 5caC levels were markedly increased in *Cpt1b* mutant CM (Fig28 A). These results indicate that accumulation of αKG after *Cpt1b* deficiency stimulates the catalytic activity of TETs, which successively convert 5mC to 5hmC, 5fC, and 5caC. 5caC might eventually accumulate due to an uncoupling of the TDG-BER axis, whose activity might not be enhanced in *Cpt1b* mutant CM. To fully understand the role of DNA demethylation in regulating CM proliferation, differentiation, and maturation, Methylation DNA immune precipitation sequencings (MeDIP-seq) with 5hmC and 5caC antibodies were performed. Unfortunately, initial bioinformatics analysis did not identify marked differences in the distribution of 5hmC and 5caC between $Ctrl^{Cre}$ and $Cpt1b^{cKO}$ samples (Fig28 B&C). Further analysis of these datasets might be helpful to clarify whether the altered DNA methylation pattern has a direct impact on the transcriptional network and whether TETs and KDM5 synergistically reshape the cardiac epigenome in *Cpt1b* deficient CM.

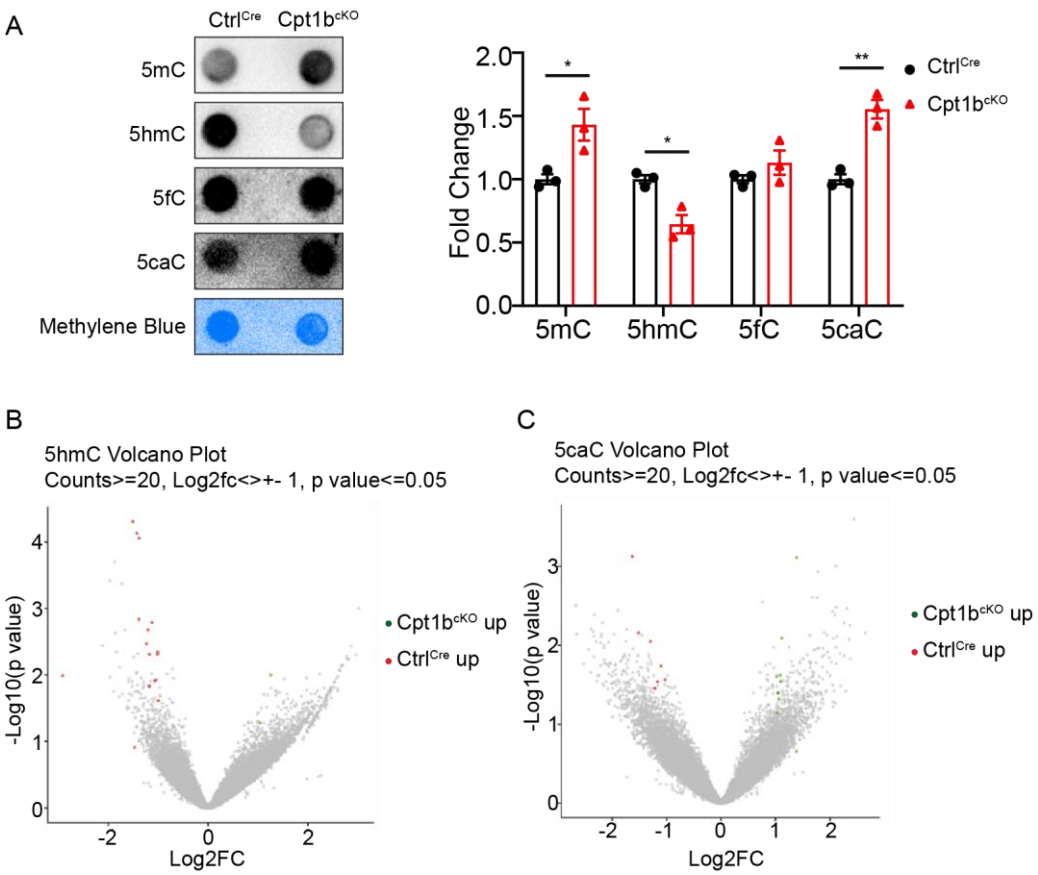

Fig28. TETs senses elevated αKG concentration to induce 5mC oxidation.

(A) Dot blot analysis for assessing DNA methylation state comparing genomic DNA extract from adult CM isolated from $Ctrl^{Cre}$ and $Cpt1b^{cKO}$ mice (n=3). Methylene Blue staining was utilized as an internal loading control. **(B-C)** Volcano plot showing the differentially methylated peaks (DEPs) comparing $Ctrl^{Cre}$ vs. $Cpt1b^{cKO}$ (n=3) in 5hmC (B) and 5caC (C) MeDIP-sequencing. **A**: Error bars represent mean ± s.e.m. Statistical analysis was performed with unpaired t-test in **A**; * $p<0.05$, ** $p<0.01$. (Dot blot assay was done with the help of Dr. Fan Wu. NGS experiment was done with the help of Dr. Stefan Guenther. MeDIP-seq data analysis was assisted by Dr. Mario Looso)

Discussion

The massive requirement for ATP in adult mammalian heart is under physiological conditions mainly met by fatty acid oxidation and oxidative phosphorylation. In this study, I uncovered that fatty acid utilization not only fuels the pump function of the heart but also maintains the adult CM at a mature state. Inhibition of fatty acid utilization by ablating *Cpt1b* retains CMs in an immature state, which allows persistent hypertrophic and hyperplasic growth in adolescent and adult hearts and enhances the regenerative capacity in response to myocardial injury. My study also reveals that FAO inhibition results in a massive accumulation of αKG, which is sensed by the αKG-dependent histone demethylase KDM5, thereby erasing CM-specific broad H3K4me3 domains at genes required for maintenance of cell identity. Thus, this study demonstrates for the first time that epigenetic modifiers act as metabolite sensors, leading to rewiring of transcription program, which in turn regulates cell identity and tissue homeostasis in response to metabolic cues.

1. Metabolic reprogramming after fatty acid oxidation inhibition

1.1 The metabolic switch from glycolysis to fatty acid oxidation is not fully completed in mouse hearts at P7

In mammals, energy metabolism in fetal heart essentially relies on glycolysis but transits shortly after birth toward fatty acid-driven OXPHOS in response to dramatic changes of substrates availability, oxygen pressure, and cardiac workload. Along with metabolic reprogramming, CMs undergo postnatal maturation reflected by a profound hypertrophic growth and cytoskeleton remodeling until reaching a fully differentiated state, which is essential for adaption to the substantial increase of cardiac workload after birth. It has been reported that glycolysis contributes to ~50% while fatty acid oxidation provides less than 10% of the total cardiac ATP production in the P1 rat heart. In stark contrast, the contribution of FAO for ATP production rises from 10% at P1 to more than 50% at two weeks of age in rabbits (Itoi et al., 1993; Lopaschuk et al., 1993; Makinde et al., 1998). These findings suggest that energy metabolism switches rapidly in the first two weeks after birth, although the specific time frame was not precisely defined.

Since αMHC-Cre mediated *Cpt1b* ablation from the embryonic stage did not provoke dramatic phenotypical changes in the heart at P7, it seems that *Cpt1b* deficiency has no strong impact on the homeostasis of fetal or neonatal CM before metabolic reprogramming occurs. Instead, inhibition of

the metabolic shift from glycolytic metabolism to FAO, which normally occurs in the first two weeks of the life, retains CM at the early neonatal state when CM are able to initiate either hyperplasic or hypertrophic growth (Cao et al., 2019; Li et al., 1996).

A compensation by CPT1A at the might also contribute to normal heart function after *Cpt1b* ablation at early neonatal stage. During cardiac development, expression of *Cpt1a* is elevated in P1 neonatal CM compared to E14.5 fetal CM but dramatically drops when CMs reach full maturity in the adult stage (Greco et al., 2016), indicating that CPT1A plays a role during early stages of heart development. Notably, CPT1A has been found to support endothelial cell proliferation by providing the raw material for dNTP synthesis (Schoors et al., 2015). However, whether CPT1A has a similar function in the cardiac lineage is still unclear. Overall, my findings indicate that *Cpt1b* deficiency in the early stage does not cause obvious cardiac defects.

1.2 FAO inhibition impairs CM maturation but promotes hypertrophic growth and CM proliferation

In this study, I have investigated the impact of *Cpt1b* deficiency on CM homeostasis in two mouse lines, in which *Cpt1b* was inactivated either in embryonic CM or in adult CMs by TAM administration. I observed a persistent expansion of CM number in both mutant strains. Furthermore, transcriptome analysis of both *Cpt1b* mutant mouse lines showed upregulated expression of positive cell cycle regulators (i.e *Ccnd1, Ccnd2, Mcm2,* and *Mcm5*), increased HIF1α signaling, but an attenuated expression of genes involved in electrophysiology, calcium handling, and contractility in adult CMs. Moreover, expression of *Acta2*, which is dominantly expressed in embryonic CM but increases in de-differentiated or hypertrophic adult CM (Ikeda et al., 2019; Kubin et al., 2011), did not show significant differences. In contrast, the skeletal muscle α-actin (*Acta1*), which is up-regulated in neonatal and de-differentiating adult CMs, was significantly increased (Gillespie-Brown et al., 1995; Vandekerckhove et al., 1986). These results indicate that metabolic reprogramming due to increased O_2 availability coincides with the transition from fetal to postnatal life but also has a profound impact on CM postnatal growth. Inhibition of the metabolic shift to FAO during postnatal development in *Cpt1b* mutant heart retains CMs at a neonatal-like stage.

Of note, the transcriptomic analysis revealed that the mRNA level of *Mtor,* a master regulator of cardiac hypertrophic growth, was significantly elevated in *Cpt1b* deficient CM. However, the levels of the active phosphorylated form of mTOR (phosph-mTOR-Ser2448) *per ser*, and S6Kinase (phosph-S6K-Thr389),

a downstream kinase of mTOR signaling, were not altered (Data not shown). These results indicate that accumulated amino acids in *Cpt1b* deficient CMs did not markedly activate mTOR-S6K signaling to support the protein synthesis as observed in the canonical hypertrophic heart.

1.3 Cardioprotective effects and enhanced CM proliferation after *Cpt1b* inactivation prevent I/R induced myocardial injury

Inhibition of FAO enhances glycolysis but attenuates oxidative stress-induced DNA damage, thereby elevating CM proliferation and regenerative capacity in response to myocardial injury (Cao et al., 2019; Cardoso et al., 2020). In this study, I detected persistent expansion of CM numbers in both Cpt1b^{cKO} and Cpt1b^{iKO} hearts under basal conditions. More importantly, increased proliferation of CM was observed within the myocardial infarction border zone 72 hours after ischemic injury, suggesting that increased capacity for CM proliferation contributes to enhanced injury repair in *Cpt1b* mutant heart. Inhibition of FAO may protect the heart from ischemic injury, probably by improving coupling of glucose oxidation with glycolysis. During and after ischemia, the rate of cytosolic glycolysis in the adult heart is high and glucose oxidation rate is low (Dyck and Lopaschuk, 2006; Kuang et al., 2004). The uncoupling of glucose oxidation from glycolysis increases the production of protons and lactate that may contribute to the development of heart failure (Fillmore et al., 2018). In *Cpt1b* mutant heart, increased PDH protein levels and elevated pyruvate but reduced lactate production was detected, indicating enhanced glucose oxidation after *Cpt1b* ablation that might improve coupling of glucose oxidation to glycolysis during ischemia, thus reducing proton production and promoting functional recovery of the heart after ischemia. In addition, inhibition of FAO due to *Cpt1b* ablation may reduce proton and Ca^{2+} overload and lower the amount of ROS production that leads to mitochondria damage and cell death during reperfusion when recovery of FAO exceeds the rate that occurs under physiological condition. Furthermore, activation of HIF1-signaling in *Cpt1b* mutant CM may also contribute to protection from ischemic injury in I/R. In zebrafish, CM regeneration is dependent upon HIF1α signaling, allowing CM to survive and the damaged heart to regenerate (Jopling et al., 2012). Overexpression of HIF1α also reduces infarct size and decrease the number of apoptotic cells during myocardial infarction in mice (Kido et al., 2005). Persistent activation of HIF1α-signaling might contribute to enhanced proliferative capacity of *Cpt1b* mutant CM but also facilitate cellular adaptation due to hypoxic preconditioning, thereby protecting *Cpt1b* mutant heart from ischemic injury. Of note, the persistent activation of HIF1α-signaling did not provoke apoptosis, since expression of anti-apoptotic genes like *Bcl2* was increased while expression of pro-apoptotic genes like *Bnip3* was

decreased in *Cpt1b* mutant heart. Thus, the benefit of *Cpt1b* deletion is based on a combination of anti-remodeling plus regeneration, though it is difficult to precisely determine the relative input. It will be important to measure the contribution of enhanced cardiac repair, but lack of proper techniques makes this difficult. Collateral vessel formation before P7 has been shown to be one of the primary reasons for reduced myocardial damage at neonatal stages (Das et al., 2019). It is unclear whether 'hypoxic preconditioning' and upregulated VEGF (data not shown) in $Cpt1b^{cKO}$ mice causes collateral artery formation at the early neonatal stage, thereby promoting the cardioprotection and heart regeneration after I/R. However, reduced scar formation after I/R surgery in $Cpt1b^{iKO}$ mice, in which *Cpt1b* was inactivated in adult CMs, indicates that enhanced ischemia resistance and proliferation capacity of *Cpt1b* deficient CM, rather than the collateral artery formation contribute primarily to improved heart regeneration.

2. Mitochondria and nucleus cross-talk: metabolite trafficking

In *Cpt1b* deficient CMs, αKG accumulation seems primarily caused by increased production of isocitrate by the IDH complex and reduced breakdown by the OGDH complex. Due to the different localization of IDH enzymes, αKG production occurs not only in the mitochondria but also in the cytoplasm via the cytosolic isoform of IDH1. It remains unclear, how or where nuclear αKG utilized by αKG-dependent DNA/histone demethylases is produced. Since αKG is hydrophobic, it is unlikely that αKG freely diffuses into the nucleus from the cytoplasm. Emerging evidence suggests that Acetyl-CoA, a high energy-containing and unstable molecule produced mainly in mitochondria can be locally produced by ATP-Citrate lyase (ACL)within the nuclei from cytosolic citrate that freely diffuse into the nucleus (Pietrocola et al., 2015; Sutendra et al., 2014). The observation that Acetyl-CoA serves as the sole donor of acetyl groups for protein/histone acetylation in many cell types argues in the same direction. Notably, PDH1A and ACSS2, enzymes capable of catalyzing the conversion of pyruvate and acetate to Acetyl-CoA in nuclei, are primarily localized in the cytosol, while ACL shows reduced levels in nuclei, although the total protein levels within the whole cell does not drop (Data not shown). Enzymatically active mitochondrial enzymes associated with the TCA cycle metabolites that are essential for epigenetic remodeling were reported to transiently and partially localize to the nucleus for activation of the zygotic genome (Nagaraj et al., 2017). Both IDH3B and IDH3G, which catalyze the conversion of isocitrate into αKG have been detected within the nuclear fraction of CMs (Data not shown). I assume that accumulated citrate can be locally converted to αKG within nuclei. To prove this idea, a precise measurement of citrate and αKG within the diverse cellular compartment,

particularly within the nuclei compartment will help answer the question about the origin of αKG in the nucleus.

3. αKG dependent enzymes function as nuclear effectors in response to cardiac metabolism reprogramming

3.1 KDM5 family senses αKG accumulation leading to demethylation of H3K4me3 broad domains

Beyond its canonical biosynthetic and bioenergetic roles, αKG plays a fundamental role in the spatiotemporal regulation of gene expression by serving as an essential cofactor of histone/DNA demethylases. Although the beneficial effect of elevated circulating αKG for protection of the heart from ischemia-reperfusion damage in a HIF1α independent manner has been reported (Olenchock et al., 2016), the exact role of αKG in the regulation of chromatin-dependent gene regulation remained unclear. In this study, I found that excessively accumulated αKG is sensed by KDM5, leading to a dramatic reduction of H3K4me3 nearby the TSS sites of genes associated with maturity and contractile function of CM.

H3K4me3 is a well-studied canonical chromatin mark of active transcription that peaks immediately downstream of the TSS but rapidly tails off (Kooistra and Helin, 2012). However, the exact role of H3K4me3 in regulating gene expression is still elusive. A recent study suggested that H3K4me3 is not an instructive signal for gene activation, since global deprivation of H3K4me3 has only a limited impact on gene expression in both yeast and mammalian cells (Brier et al., 2017). However, in support of the idea that H3K4me3 promotes transcription, H3K4me3 was reported to facilitate the recruitment of basal transcription factor TFIID to actively transcribed genes via interactions with TAF3, thereby stimulating preinitiation complex (PIC) formation (Lauberth et al., 2013). Moreover, MLL2/COMPASS mediated formation of H3K4me3 prevents suppression of developmental genes by repelling PRC2 and the DNA methylation machinery (Douillet et al., 2020). Several studies identified a small subset of genes, in which H3K4me3 distribution extends further downstream into the gene body for more than 40 kb, although most H3K4me3 is enriched at the promoter-proximal region (1–2 kb from the TSS). These genes are transcriptionally more active and mainly associated with cell identity in various species and tissues including the heart (Benayoun et al., 2014; Gilsbach et al., 2018; Howe et al., 2017). Deposition of broad H3K4me3 peaks appears to increase release of paused

Pol II and transcriptional elongation, thus facilitating gene expression (Chen et al., 2015). Consistent with these studies, I found that genes with the broadest H3K4me3 peaks (top 25%) in CMs are transcriptionally more active than genes with sharp peaks and preferentially associated with cell identity and function (Benayoun et al., 2014; Chen et al., 2015; Sze et al., 2020). 151 genes were identified that showed deregulated H3K4me3 enrichment and concomitant mitigated gene transcription in *Cpt1b* mutant CMs. Over 62% of these genes contain broad peaks and are largely involved in heart development and cardiac contraction, suggesting that genes with cell type-specific broad H3K4me3 peaks that are required for cell state and function maintenance are preferentially targeted by H3K4me3 demethylases.

An interesting question is how KDM5 specifically erases broad but not narrow H3K4me3 peaks within the set of CM identity-related genes after sensing excessive accumulation of αKG. Broader H3K4me3 domains may provide more targeting sites for KDM5, since recruitment of KDM5 to genic regions is positively correlated with H3K4me3 signals. Once KDM5 is activated by sensing elevated nuclear αKG, KDM5 may bind to its target genes more stably and spread over the broader H3K4me3 domains. It is also possible that KDM5 has a target preference on genes with cell type-specific broad H3K4me3 peaks that may represent cell identity and function genes, which differ from genes with conserved broad H3K4me3 peaks across normal cells, which usually contain distinct cis-regulatory elements such as TATA-less or TATA-rich elements, combined with other epigenetic features such as CpG methylation (Hughes et al., 2020).

Among the histone modifications examined in this study, H3K4me3 is the sole methylation mark that dropped after *Cpt1b* inactivation. It is unlikely that KMT2 mediated H3K4 trimethylation is impaired, because the mRNA levels of most KMTs including KMT2 remained unchanged. Additionally, other histone methylation marks remained unchanged or are even elevated in *Cpt1b* deficient CM, suggesting that KMT activity was not impaired by the availability of SAM, a common substrate involved in methyl group transfers. Of note, the targeted metabolome analysis showed that methionine, the precursor for SAM production, was elevated after *Cpt1b* ablation, although the intracellular levels of SAM and SAH were not directly examined. I cannot exclude the possibility that SAM levels are increased in *Cpt1b* deficient CM and subsequently lead to increased levels of H3K9me3, H3K27me3, and H4K20me2. These observations indicate that KDM5 functions as a nuclear effector in response to excessive αKG accumulation. Another possibility to explain the specificity of KDM5 as a nuclear effector is that the enzymatic kinetics of KDM5 differs from other KDMs (Cascella and Mirica, 2012).

KDM5B, which is particular interesting among four members of the KDM5 family for its cell/tissue-specific expression pattern and functional importance in heart development, has been reported to be recruited to H3K36me3 in highly expressed self-renewal associated genes in embryonic stem cell (ESC) (Zaidi et al., 2013). KDM5B-dependent demethylation of intragenic H3K4me3 is essential to safeguard transcriptional elongation via repressing aberrant intragenic entry of the Pol II machinery (Xie et al., 2011). Since overexpression of *Kdm5b* promotes CM proliferation, another interesting hypothesis is that demethylation in highly transcribed genes with broad H3K4me3 peaks CM state maintenance and function-related genes occurs more dynamically to prevent spurious transcriptional initiation in intragenic regions. This dynamic demethylation activity may make KDM5B more susceptible to changes in αKG levels, leading to demethylation specifically within highly transcribed genes.

3.2 TETs might not contribute to the cardiac phenotype in *Cpt1b* deficient mice

Dynamic DNA methylation/demethylation is an essential epigenetic mechanism regulating chromatin state and gene expression. αKG-dependent DNA demethylases, TETs, play crucial roles in regulating cardiac regeneration and remolding. In the *Tet* family, *Tet1* is lowly expressed whereas *Tet2* and *Tet3* are highly expressed in neonatal and adult CM (Giudice et al., 2014; Greco et al., 2016). However, *Tet2* ablation in the CM did not induce phenotypical abnormality, likely due to the compensatory function of *Tet3* (Greco et al., 2016). The cardiac-specific inactivation of *Tet2* and *Tet3* in the early stage of cardiogenesis leads to embryonic lethality, confirming functional redundancy of these two enzymes (Fang et al., 2019).

TETs bind to 5mC and convert it into 5hmC, followed by oxidation to 5fC and 5caC. In *Cpt1b* ablated CMs, the global level of 5mC was slightly but significantly elevated, which might be attributed to enhanced DNMT activity in response to the assumed SAM accumulation. In stark contrast, the 5hmC level was dramatically reduced. 5fC was unchanged but 5caC showed strong accumulation after *Cpt1b* ablation (Fig 28A). It appears that TETs sense the excessive αKG accumulation and actively induce 5mC oxidation. 5hmC levels were decreased after *Cpt1b* inactivation, however, 5mC showed slightly elevation. Increase of 5mC is perplexing and a convincing explanation is currently missing. It seems likely that the activity of the TDG-BER axis is not sufficiently enhanced, leading to accumulation of 5caC in *Cpt1b* deficient CMs. Moreover, 5hmC and 5caC MeDIP-seq revealed only a small proportion of differential 5hmC and 5caC peaks (DEPs) in *Cpt1b* deficient CMs within protein-coding genes

(5hmC, 13 out of 110 DEPs; 5caC, 23 out of 268 DEPs), indicating a stronger impact of *Cpt1b* deficiency on the methylation status of intergenic compared to coding regions. Notably, specific depletion of *Tet2* and *Tet3* individually or concomitantly in adult CM did not induce a cardiac phenotype, although global levels of 5mC, 5hmC, and 5caC were altered after *Cpt1b* inactivation (Data not shown). Thus, the function of TETs in *Cpt1b* deficient heart do not seem to contribute to the cardiac phenotype.

4. *Cpt1b* ablation in various Cre mouse lines has distinct effects on heart homeostasis

Several *Cpt1b* mutant mouse lines have been generated in the course of this study and in previous studies to investigate the impact of FAO on heart tissue homeostasis. Germline inactivation of *Cpt1b* leads to a lethal phenotype at embryonic stages, while *Cpt1b* haploinsufficiency aggravated cardiac hypertrophy induced by pressure overload and had substantial effects on adipose tissue (Ji et al., 2008). In addition, *Cpt1b* heterozygotes mice show a lipotoxicity phenotype with reduction of mitochondria biogenesis (He et al., 2012). I assume that *Cpt1b* inactivation in adipose tissue might lead to increased concentration of circulating free fatty acids, which subsequently induces the lipotoxic phenotype as in patients with heart failure (Goldberg et al., 2012). In the MCK-Cre mediated *Cpt1b* knockout mouse model, *Cpt1b* inactivation in both cardiac and skeletal muscle induces a strong cardiac phenotype and early mortality starting from 15 weeks after birth, which as accompanied by a lipotoxic phenotype in hearts (Haynie et al., 2014). Since the MCK-Cre mediated *Cpt1b* inactivation also resulted in random seizures, suggesting that dysregulation of fatty acid metabolism in skeletal muscle leads to elevated circulating fatty acids, which causes a cardiac pathological phenotype. Surprisingly, no lipid accumulation or a lipotoxic phenotype were detected in $Cpt1b^{cKO}$ mice. The most likely explanation for this unexpected result is metabolization of circulating lipids by skeletal muscle and fat tissue. The strong downregulation of CM-derived LPL in the heart may protect CM from lipotoxicity seen in other *Cpt1b*-deficient mouse strains.

5. Therapeutic potential of metabolic and/or epigenetic targets in myocardial injury repair

In this study, I demonstrated that inhibition of FAO by inactivating *Cpt1b* causes excessive accumulation of αKG, which supports repair of myocardial injury after I/R. This finding is consistent with the former studies showing that exogenous supplementation of αKG or inhibition of FAO by inactivating CPT1 or CPT2 improves heart function in myocardial injury models (Hirose et al., 2019). Modulating the energy metabolism, especially the balance between fatty acids oxidation, glycolysis, and amino acids metabolism has been an object of interest for researchers to develop therapeutic interventions for the treatment of patients with myocardial injury, although many hurdles have to be overcome to establish a robust therapeutic regimen. As the key player in cardiac energy metabolism, CPT1 is an example of metabolic targets for the improvement of cardiac function after injury. A previous study showed that inhibition of FAO by Etomoxir, a widely used pan-inhibitor of CPT1, improved heart function of heart failure patients in clinical trials (Holubarsch et al., 2007). However, Etomoxir, which irreversibly inhibits CPT1 can cause significant hepatotoxicity. Therefore, a highly selective inhibitor of CPT1B is required as a potential option for treatment of heart failure patients. For example, Perhexiline, which preferentially targets CPT1B instead of CPT1A and CPT1C, improves ejection fraction in patients in a small clinical trial (Abozguia et al., 2010; Kennedy et al., 1996). Oxfenicine, a precursor of the CPT1B inhibitor 4-hydroxyphenylglyoxylate, partially inhibits fatty acid oxidation and improves heart function in dogs (Lionetti et al., 2005; Ma et al., 2020). However, potential side effects still need to be evaluated more carefully in clinical trials. Trimetazidine and ranolazine are compounds inhibiting the uptake of fatty acids into CM in humans (Bagger et al., 1997; Tuunanen et al., 2006). Short-term treatment with Trimetazidine has been shown to improve left ventricle contraction in heart failure patients (Belardinelli and Purcaro, 2001). A three-month treatment of ranolazine showed promising improvement of left ventricle function and prevented ventricular repolarization abnormalities (Hale et al., 2008; Rastogi et al., 2008).

Targeting mitochondrial oxidative metabolism is a promising strategy to improve heart regeneration and repair. However, manipulation of metabolic targets of aKG in the nucleus, serving as epigenetic effectors that alter gene expression, may also own beneficial properties and improve heart function. My study demonstrates that KDM5 functions as such an epigenetic effector by sensing metabolic cues to reshape the cardiac epigenome, thereby retaining CM at a less mature but more proliferative state.

The identification of small molecules that specifically enhance the enzymatic activity of KDM5 might be an alternative and promising therapeutic approach to improve heart regeneration and repair in the future.

6. Conclusions and proposed model

In cardiac muscle cells, compensatory metabolic pathways that replenish TCA intermediate metabolites are activated when fatty acids cannot be sufficiently utilized in mitochondria. In this study, I demonstrated that increased glycolysis oxidation and amino acid metabolism compensates for reduced production of intermediate metabolites, such as Acetyl-CoA, from fatty acid oxidation after inactivation of *Cpt1b*. During these compensatory processes, the αKG level dramatically increases due to combined effects of elevated αKG production and reduced consumption (Fig.29).

Excessively accumulated αKG enhance activity of αKG dependent enzymes. In *Cpt1b* deficient CM, KDM5 family enzymes function as nuclear effectors sensing the increased αKG level and actively erase H3K4me3, particularly broad H3K4me3 domains, which demarcate a set of genes associated with CM maturation and function. As a consequence, adult CM convert into a less mature, neonatal-like state, which bestows CM not only with enhanced resistance to ischemic injury but also with augmented capacity for continuous hypertrophic and hyperplastic growth, leading to eventually to enlarged hearts with conserved cardiac function (Fig.29).

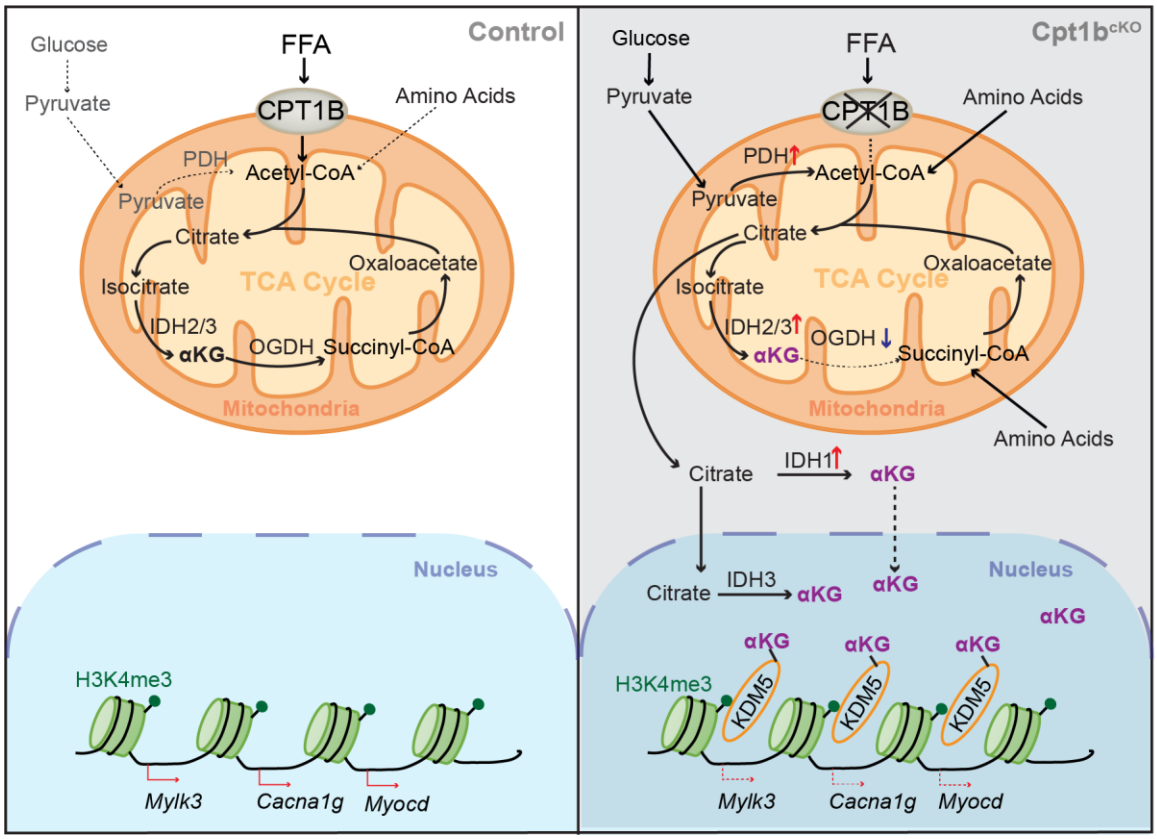

Fig29. Working model and hypothesis

Reference:

Abozguia, K., Elliott, P., McKenna, W., Phan, T.T., Nallur-Shivu, G., Ahmed, I., Maher, A.R., Kaur, K., Taylor, J., Henning, A.*, et al.* (2010). Metabolic modulator perhexiline corrects energy deficiency and improves exercise capacity in symptomatic hypertrophic cardiomyopathy. Circulation *122*, 1562-1569.

Adler, C.P., and Friedburg, H. (1986). Myocardial DNA content, ploidy level and cell number in geriatric hearts: post-mortem examinations of human myocardium in old age. J Mol Cell Cardiol *18*, 39-53.

Ang, S.Y., Uebersohn, A., Spencer, C.I., Huang, Y., Lee, J.E., Ge, K., and Bruneau, B.G. (2016). KMT2D regulates specific programs in heart development via histone H3 lysine 4 di-methylation. Development *143*, 810-821.

Atherton, H.J., Dodd, M.S., Heather, L.C., Schroeder, M.A., Griffin, J.L., Radda, G.K., Clarke, K., and Tyler, D.J. (2011). Role of pyruvate dehydrogenase inhibition in the development of hypertrophy in the hyperthyroid rat heart: a combined magnetic resonance imaging and hyperpolarized magnetic resonance spectroscopy study. Circulation *123*, 2552-2561.

Bagger, J.P., Botker, H.E., Thomassen, A., and Nielsen, T.T. (1997). Effects of ranolazine on ischemic threshold, coronary sinus blood flow, and myocardial metabolism in coronary artery disease. Cardiovasc Drugs Ther *11*, 479-484.

Bassat, E., Mutlak, Y.E., Genzelinakh, A., Shadrin, I.Y., Baruch Umansky, K., Yifa, O., Kain, D., Rajchman, D., Leach, J., Riabov Bassat, D.*, et al.* (2017). The extracellular matrix protein agrin promotes heart regeneration in mice. Nature *547*, 179-184.

Belardinelli, R., and Purcaro, A. (2001). Effects of trimetazidine on the contractile response of chronically dysfunctional myocardium to low-dose dobutamine in ischaemic cardiomyopathy. Eur Heart J *22*, 2164-2170.

Benayoun, B.A., Pollina, E.A., Ucar, D., Mahmoudi, S., Karra, K., Wong, E.D., Devarajan, K., Daugherty, A.C., Kundaje, A.B., Mancini, E.*, et al.* (2014). H3K4me3 breadth is linked to cell identity and transcriptional consistency. Cell *158*, 673-688.

Bergmann, O., Bhardwaj, R.D., Bernard, S., Zdunek, S., Barnabe-Heider, F., Walsh, S., Zupicich, J., Alkass, K., Buchholz, B.A., Druid, H.*, et al.* (2009). Evidence for cardiomyocyte renewal in humans. Science *324*, 98-102.

Bers, D.M. (2002). Cardiac excitation-contraction coupling. Nature *415*, 198-205.

Bertero, A., and Murry, C.E. (2018). Hallmarks of cardiac regeneration. Nat Rev Cardiol *15*, 579-580.

Bertero, E., and Maack, C. (2018). Metabolic remodelling in heart failure. Nat Rev Cardiol.

Bicknell, K.A., Coxon, C.H., and Brooks, G. (2004). Forced expression of the cyclin B1-CDC2 complex induces proliferation in adult rat cardiomyocytes. Biochem J *382*, 411-416.

Black, F.M., Packer, S.E., Parker, T.G., Michael, L.H., Roberts, R., Schwartz, R.J., and Schneider, M.D. (1991). The vascular smooth muscle alpha-actin gene is reactivated during cardiac hypertrophy provoked by load. J Clin Invest *88*, 1581-1588.

Bostrom, P., Mann, N., Wu, J., Quintero, P.A., Plovie, E.R., Panakova, D., Gupta, R.K., Xiao, C., MacRae, C.A., Rosenzweig, A.*, et al.* (2010). C/EBPbeta controls exercise-induced cardiac growth and protects against pathological cardiac remodeling. Cell *143*, 1072-1083.

Braz, J.C., Gregory, K., Pathak, A., Zhao, W., Sahin, B., Klevitsky, R., Kimball, T.F., Lorenz, J.N., Nairn, A.C., Liggett, S.B.*, et al.* (2004). PKC-alpha regulates cardiac contractility and propensity toward heart failure. Nat Med *10*, 248-254.

Brier, A.B., Loft, A., Madsen, J.G.S., Rosengren, T., Nielsen, R., Schmidt, S.F., Liu, Z., Yan, Q., Gronemeyer, H., and Mandrup, S. (2017). The KDM5 family is required for activation of pro-proliferative cell cycle genes during adipocyte differentiation. Nucleic Acids Res *45*, 1743-1759.

Brodsky, W.Y., Arefyeva, A.M., and Uryvaeva, I.V. (1980). Mitotic polyploidization of mouse heart myocytes during the first postnatal week. Cell Tissue Res *210*, 133-144.

Brooks, G., Poolman, R.A., McGill, C.J., and Li, J.M. (1997). Expression and activities of cyclins and cyclin-dependent kinases in developing rat ventricular myocytes. J Mol Cell Cardiol *29*, 2261-2271.

Bu, L., Jiang, X., Martin-Puig, S., Caron, L., Zhu, S., Shao, Y., Roberts, D.J., Huang, P.L., Domian, I.J., and Chien, K.R. (2009). Human ISL1 heart progenitors generate diverse multipotent cardiovascular cell lineages. Nature *460*, 113-117.

Buckingham, M., Meilhac, S., and Zaffran, S. (2005). Building the mammalian heart from two sources of myocardial cells. Nat Rev Genet *6*, 826-835.

Cao, T., Liccardo, D., LaCanna, R., Zhang, X., Lu, R., Finck, B.N., Leigh, T., Chen, X., Drosatos, K., and Tian, Y. (2019). Fatty Acid Oxidation Promotes Cardiomyocyte Proliferation Rate but Does Not Change Cardiomyocyte Number in Infant Mice. Front Cell Dev Biol *7*, 42.

Cardoso, A.C., Lam, N.T., Savla, J.J., Nakada, Y., Pereira, A.H.M., Elnwasany, A., Menendez-Montes, I., Ensley, E.L., Bezan Petric, U., Sharma, G.*, et al.* (2020). Mitochondrial substrate utilization regulates cardiomyocyte cell-cycle progression. Nature Metabolism *2*, 167-178.

Carmeliet, E. (2019). Pacemaking in cardiac tissue. From IK2 to a coupled-clock system. Physiol Rep *7*, e13862.

Cascella, B., and Mirica, L.M. (2012). Kinetic analysis of iron-dependent histone demethylases: alpha-ketoglutarate substrate inhibition and potential relevance to the regulation of histone demethylation in cancer cells. Biochemistry *51*, 8699-8701.

Cattaneo, P., Kunderfranco, P., Greco, C., Guffanti, A., Stirparo, G.G., Rusconi, F., Rizzi, R., Di Pasquale, E., Locatelli, S.L., Latronico, M.V.*, et al.* (2016). DOT1L-mediated H3K79me2 modification critically regulates gene expression during cardiomyocyte differentiation. Cell Death Differ *23*, 555-564.

Chaudhry, H.W., Dashoush, N.H., Tang, H., Zhang, L., Wang, X., Wu, E.X., and Wolgemuth, D.J. (2004). Cyclin A2 mediates cardiomyocyte mitosis in the postmitotic myocardium. J Biol Chem *279*, 35858-35866.

Chen, K., Chen, Z., Wu, D., Zhang, L., Lin, X., Su, J., Rodriguez, B., Xi, Y., Xia, Z., Chen, X.*, et al.* (2015). Broad H3K4me3 is associated with increased transcription elongation and enhancer activity at tumor-suppressor genes. Nat Genet *47*, 1149-1157.

Cho, E., Mysliwiec, M.R., Carlson, C.D., Ansari, A., Schwartz, R.J., and Lee, Y. (2018). Cardiac-specific developmental and epigenetic functions of Jarid2 during embryonic development. J Biol Chem *293*, 11659-11673.

Chowdhury, R., Yeoh, K.K., Tian, Y.M., Hillringhaus, L., Bagg, E.A., Rose, N.R., Leung, I.K., Li, X.S., Woon, E.C., Yang, M.*, et al.* (2011). The oncometabolite 2-hydroxyglutarate inhibits histone lysine demethylases. EMBO Rep *12*, 463-469.

Chuva de Sousa Lopes, S.M., Hassink, R.J., Feijen, A., van Rooijen, M.A., Doevendans, P.A., Tertoolen, L., Brutel de la Riviere, A., and Mummery, C.L. (2006). Patterning the heart, a template for human cardiomyocyte development. Dev Dyn *235*, 1994-2002.

Cluntun, A.A., Huang, H., Dai, L., Liu, X., Zhao, Y., and Locasale, J.W. (2015). The rate of glycolysis quantitatively mediates specific histone acetylation sites. Cancer Metab *3*, 10.

Collins, B.E., Greer, C.B., Coleman, B.C., and Sweatt, J.D. (2019). Histone H3 lysine K4 methylation and its role in learning and memory. Epigenetics Chromatin *12*, 7.

Dai, D.F., Danoviz, M.E., Wiczer, B., Laflamme, M.A., and Tian, R. (2017). Mitochondrial Maturation in Human Pluripotent Stem Cell Derived Cardiomyocytes. Stem Cells Int *2017*, 5153625.

Dai, Z., Ramesh, V., and Locasale, J.W. (2020). The evolving metabolic landscape of chromatin biology and epigenetics. Nat Rev Genet.

Das, S., Goldstone, A.B., Wang, H., Farry, J., D'Amato, G., Paulsen, M.J., Eskandari, A., Hironaka, C.E., Phansalkar, R., Sharma, B.*, et al.* (2019). A Unique Collateral Artery Development Program Promotes Neonatal Heart Regeneration. Cell *176*, 1128-1142 e1118.

Davila-Roman, V.G., Vedala, G., Herrero, P., de las Fuentes, L., Rogers, J.G., Kelly, D.P., and Gropler, R.J. (2002). Altered myocardial fatty acid and glucose metabolism in idiopathic dilated cardiomyopathy. J Am Coll Cardiol *40*, 271-277.

Dawlaty, M.M., Ganz, K., Powell, B.E., Hu, Y.C., Markoulaki, S., Cheng, A.W., Gao, Q., Kim, J., Choi, S.W., Page, D.C.*, et al.* (2011). Tet1 is dispensable for maintaining pluripotency and its loss is compatible with embryonic and postnatal development. Cell Stem Cell *9*, 166-175.

de Boer, V.C., and Houten, S.M. (2014). A mitochondrial expatriate: nuclear pyruvate dehydrogenase. Cell *158*, 9-10.

Devereux, R.B., Roman, M.J., Paranicas, M., O'Grady, M.J., Lee, E.T., Welty, T.K., Fabsitz, R.R., Robbins, D., Rhoades, E.R., and Howard, B.V. (2000). Impact of diabetes on cardiac structure and function: the strong heart study. Circulation *101*, 2271-2276.

Dhar, S.S., Zhao, D., Lin, T., Gu, B., Pal, K., Wu, S.J., Alam, H., Lv, J., Yun, K., Gopalakrishnan, V.*, et al.* (2018). MLL4 Is Required to Maintain Broad H3K4me3 Peaks and Super-Enhancers at Tumor Suppressor Genes. Mol Cell *70*, 825-841 e826.

Doenst, T., Nguyen, T.D., and Abel, E.D. (2013). Cardiac metabolism in heart failure: implications beyond ATP production. Circ Res *113*, 709-724.

Doenst, T., Pytel, G., Schrepper, A., Amorim, P., Farber, G., Shingu, Y., Mohr, F.W., and Schwarzer, M. (2010). Decreased rates of substrate oxidation ex vivo predict the onset of heart failure and contractile dysfunction in rats with pressure overload. Cardiovasc Res *86*, 461-470.

Douillet, D., Sze, C.C., Ryan, C., Piunti, A., Shah, A.P., Ugarenko, M., Marshall, S.A., Rendleman, E.J., Zha, D., Helmin, K.A.*, et al.* (2020). Uncoupling histone H3K4 trimethylation from developmental gene expression via an equilibrium of COMPASS, Polycomb and DNA methylation. Nat Genet *52*, 615-625.

Drake, K.J., Sidorov, V.Y., McGuinness, O.P., Wasserman, D.H., and Wikswo, J.P. (2012). Amino acids as metabolic substrates during cardiac ischemia. Exp Biol Med (Maywood) *237*, 1369-1378.

Duan, J., Gherghe, C., Liu, D., Hamlett, E., Srikantha, L., Rodgers, L., Regan, J.N., Rojas, M., Willis, M., Leask, A.*, et al.* (2012). Wnt1/betacatenin injury response activates the epicardium and cardiac fibroblasts to promote cardiac repair. EMBO J *31*, 429-442.

Dunlay, S.M., Roger, V.L., and Redfield, M.M. (2017). Epidemiology of heart failure with preserved ejection fraction. Nat Rev Cardiol *14*, 591-602.

Dyck, J.R., and Lopaschuk, G.D. (2006). AMPK alterations in cardiac physiology and pathology: enemy or ally? J Physiol *574*, 95-112.

Eisenberg, T., Abdellatif, M., Schroeder, S., Primessnig, U., Stekovic, S., Pendl, T., Harger, A., Schipke, J., Zimmermann, A., Schmidt, A.*, et al.* (2016). Cardioprotection and lifespan extension by the natural polyamine spermidine. Nat Med *22*, 1428-1438.

Fang, S., Li, J., Xiao, Y., Lee, M., Guo, L., Han, W., Li, T., Hill, M.C., Hong, T., Mo, W.*, et al.* (2019). Tet inactivation disrupts YY1 binding and long-range chromatin interactions during embryonic heart development. Nat Commun *10*, 4297.

Fernandez-Caggiano, M., Kamynina, A., Francois, A.A., Prysyazhna, O., Eykyn, T.R., Krasemann, S., Crespo-Leiro, M.G., Vieites, M.G., Bianchi, K., Morales, V.*, et al.* (2020). Mitochondrial pyruvate carrier abundance mediates pathological cardiac hypertrophy. Nat Metab *2*, 1223-1231.

Fernandez, S., Viola, J.M., Torres, A., Wallace, M., Trefely, S., Zhao, S., Affronti, H.C., Gengatharan, J.M., Guertin, D.A., Snyder, N.W.*, et al.* (2019). Adipocyte ACLY Facilitates Dietary Carbohydrate Handling to Maintain Metabolic Homeostasis in Females. Cell Reports *27*, 2772-2784.e2776.

Figueroa, M.E., Abdel-Wahab, O., Lu, C., Ward, P.S., Patel, J., Shih, A., Li, Y., Bhagwat, N., Vasanthakumar, A., Fernandez, H.F.*, et al.* (2010). Leukemic IDH1 and IDH2 mutations result in a hypermethylation phenotype, disrupt TET2 function, and impair hematopoietic differentiation. Cancer Cell *18*, 553-567.

Fillmore, N., Levasseur, J.L., Fukushima, A., Wagg, C.S., Wang, W., Dyck, J.R.B., and Lopaschuk, G.D. (2018). Uncoupling of glycolysis from glucose oxidation accompanies the development of heart failure with preserved ejection fraction. Mol Med *24*, 3.

Flink, I.L., Oana, S., Maitra, N., Bahl, J.J., and Morkin, E. (1998). Changes in E2F complexes containing retinoblastoma protein family members and increased cyclin-dependent kinase inhibitor activities during terminal differentiation of cardiomyocytes. J Mol Cell Cardiol *30*, 563-578.

Foglia, M.J., and Poss, K.D. (2016). Building and re-building the heart by cardiomyocyte proliferation. Development *143*, 729-740.

Galdos, F.X., Guo, Y., Paige, S.L., VanDusen, N.J., Wu, S.M., and Pu, W.T. (2017). Cardiac Regeneration: Lessons From Development. Circ Res *120*, 941-959.

Garcia-Martinez, V., and Schoenwolf, G.C. (1993). Primitive-streak origin of the cardiovascular system in avian embryos. Dev Biol *159*, 706-719.

Gerdes, A.M., Kellerman, S.E., Moore, J.A., Muffly, K.E., Clark, L.C., Reaves, P.Y., Malec, K.B., McKeown, P.P., and Schocken, D.D. (1992). Structural remodeling of cardiac myocytes in patients with ischemic cardiomyopathy. Circulation *86*, 426-430.

Gillespie-Brown, J., Fuller, S.J., Bogoyevitch, M.A., Cowley, S., and Sugden, P.H. (1995). The mitogen-activated protein kinase kinase MEK1 stimulates a pattern of gene expression typical of the hypertrophic phenotype in rat ventricular cardiomyocytes. J Biol Chem *270*, 28092-28096.

Gilsbach, R., Preissl, S., Gruning, B.A., Schnick, T., Burger, L., Benes, V., Wurch, A., Bonisch, U., Gunther, S., Backofen, R.*, et al.* (2014). Dynamic DNA methylation orchestrates cardiomyocyte development, maturation and disease. Nat Commun *5*, 5288.

Gilsbach, R., Schwaderer, M., Preissl, S., Gruning, B.A., Kranzhofer, D., Schneider, P., Nuhrenberg, T.G., Mulero-Navarro, S., Weichenhan, D., Braun, C.*, et al.* (2018). Distinct epigenetic programs regulate cardiac myocyte development and disease in the human heart in vivo. Nat Commun *9*, 391.

Giudice, J., Xia, Z., Wang, E.T., Scavuzzo, M.A., Ward, A.J., Kalsotra, A., Wang, W., Wehrens, X.H., Burge, C.B., Li, W.*, et al.* (2014). Alternative splicing regulates vesicular trafficking genes in cardiomyocytes during postnatal heart development. Nat Commun *5*, 3603.

Goikoetxea, M.J., Beaumont, J., Gonzalez, A., Lopez, B., Querejeta, R., Larman, M., and Diez, J. (2006). Altered cardiac expression of peroxisome proliferator-activated receptor-isoforms in patients with hypertensive heart disease. Cardiovasc Res *69*, 899-907.

Goldberg, I.J., Trent, C.M., and Schulze, P.C. (2012). Lipid metabolism and toxicity in the heart. Cell Metab *15*, 805-812.

Gorza, L., Ausoni, S., Merciai, N., Hastings, K.E., and Schiaffino, S. (1993). Regional differences in troponin I isoform switching during rat heart development. Dev Biol *156*, 253-264.

Graff, J., and Tsai, L.H. (2013). Histone acetylation: molecular mnemonics on the chromatin. Nat Rev Neurosci *14*, 97-111.

Greco, C.M., Kunderfranco, P., Rubino, M., Larcher, V., Carullo, P., Anselmo, A., Kurz, K., Carell, T., Angius, A., Latronico, M.V.*, et al.* (2016). DNA hydroxymethylation controls cardiomyocyte gene expression in development and hypertrophy. Nat Commun *7*, 12418.

Greenberg, M.V.C., and Bourc'his, D. (2019). The diverse roles of DNA methylation in mammalian development and disease. Nat Rev Mol Cell Biol *20*, 590-607.

Guo, Y., and Pu, W.T. (2020). Cardiomyocyte Maturation: New Phase in Development. Circ Res *126*, 1086-1106.

Gusterson, R., Brar, B., Faulkes, D., Giordano, A., Chrivia, J., and Latchman, D. (2002). The transcriptional co-activators CBP and p300 are activated via phenylephrine through the p42/p44 MAPK cascade. J Biol Chem *277*, 2517-2524.

Gusterson, R.J., Jazrawi, E., Adcock, I.M., and Latchman, D.S. (2003). The transcriptional co-activators CREB-binding protein (CBP) and p300 play a critical role in cardiac hypertrophy that is dependent on their histone acetyltransferase activity. J Biol Chem *278*, 6838-6847.

Hale, S.L., Shryock, J.C., Belardinelli, L., Sweeney, M., and Kloner, R.A. (2008). Late sodium current inhibition as a new cardioprotective approach. J Mol Cell Cardiol *44*, 954-967.

Hamasaki, S., Al Suwaidi, J., Higano, S.T., Miyauchi, K., Holmes, D.R., Jr., and Lerman, A. (2000). Attenuated coronary flow reserve and vascular remodeling in patients with hypertension and left ventricular hypertrophy. J Am Coll Cardiol *35*, 1654-1660.

Haynie, K.R., Vandanmagsar, B., Wicks, S.E., Zhang, J., and Mynatt, R.L. (2014). Inhibition of carnitine palymitoyltransferase1b induces cardiac hypertrophy and mortality in mice. Diabetes Obes Metab *16*, 757-760.

He, L., Kim, T., Long, Q., Liu, J., Wang, P., Zhou, Y., Ding, Y., Prasain, J., Wood, P.A., and Yang, Q. (2012). Carnitine palmitoyltransferase-1b deficiency aggravates pressure overload-induced cardiac hypertrophy caused by lipotoxicity. Circulation *126*, 1705-1716.

He, Y.F., Li, B.Z., Li, Z., Liu, P., Wang, Y., Tang, Q., Ding, J., Jia, Y., Chen, Z., Li, L.*, et al.* (2011). Tet-mediated formation of 5-carboxylcytosine and its excision by TDG in mammalian DNA. Science *333*, 1303-1307.

Heallen, T., Morikawa, Y., Leach, J., Tao, G., Willerson, J.T., Johnson, R.L., and Martin, J.F. (2013). Hippo signaling impedes adult heart regeneration. Development *140*, 4683-4690.

Heallen, T., Zhang, M., Wang, J., Bonilla-Claudio, M., Klysik, E., Johnson, R.L., and Martin, J.F. (2011). Hippo pathway inhibits Wnt signaling to restrain cardiomyocyte proliferation and heart size. Science *332*, 458-461.

Heineke, J., and Molkentin, J.D. (2006). Regulation of cardiac hypertrophy by intracellular signalling pathways. Nat Rev Mol Cell Biol *7*, 589-600.

Herget, G.W., Neuburger, M., Plagwitz, R., and Adler, C.P. (1997). DNA content, ploidy level and number of nuclei in the human heart after myocardial infarction. Cardiovasc Res *36*, 45-51.

Hinson, J.T., Chopra, A., Nafissi, N., Polacheck, W.J., Benson, C.C., Swist, S., Gorham, J., Yang, L., Schafer, S., Sheng, C.C.*, et al.* (2015). HEART DISEASE. Titin mutations in iPS cells define sarcomere insufficiency as a cause of dilated cardiomyopathy. Science *349*, 982-986.

Hirose, K., Payumo, A.Y., Cutie, S., Hoang, A., Zhang, H., Guyot, R., Lunn, D., Bigley, R.B., Yu, H., Wang, J.*, et al.* (2019). Evidence for hormonal control of heart regenerative capacity during endothermy acquisition. Science *364*, 184-188.

Holliday, R., and Pugh, J.E. (1975). DNA modification mechanisms and gene activity during development. Science *187*, 226-232.

Holtwick, R., van Eickels, M., Skryabin, B.V., Baba, H.A., Bubikat, A., Begrow, F., Schneider, M.D., Garbers, D.L., and Kuhn, M. (2003). Pressure-independent cardiac hypertrophy in mice with cardiomyocyte-restricted inactivation of the atrial natriuretic peptide receptor guanylyl cyclase-A. J Clin Invest *111*, 1399-1407.

Holubarsch, C.J., Rohrbach, M., Karrasch, M., Boehm, E., Polonski, L., Ponikowski, P., and Rhein, S. (2007). A double-blind randomized multicentre clinical trial to evaluate the efficacy and safety of two doses of etomoxir in comparison with placebo in patients with moderate congestive heart failure: the ERGO (etomoxir for the recovery of glucose oxidation) study. Clin Sci (Lond) *113*, 205-212.

Howe, F.S., Fischl, H., Murray, S.C., and Mellor, J. (2017). Is H3K4me3 instructive for transcription activation? Bioessays *39*, 1-12.

Huang, G.N., Thatcher, J.E., McAnally, J., Kong, Y., Qi, X., Tan, W., DiMaio, J.M., Amatruda, J.F., Gerard, R.D., Hill, J.A.*, et al.* (2012). C/EBP transcription factors mediate epicardial activation during heart development and injury. Science *338*, 1599-1603.

Huang, K., Liu, P., Li, X., Chen, S., Wang, L., Qin, L., Su, Z., Huang, W., Liu, J., Jia, B.*, et al.* (2014). Neural progenitor cells from human induced pluripotent stem cells generated less autogenous immune response. Sci China Life Sci *57*, 162-170.

Huang, X., Lv, X., Song, H., Yang, Q., Sun, Y., Zhang, W., Yu, X., Dong, S., Yao, W., Li, Y.*, et al.* (2017). The relationship between S-adenosylhomocysteine and coronary artery lesions: A case control study. Clin Chim Acta *471*, 314-320.

Hughes, A.L., Kelley, J.R., and Klose, R.J. (2020). Understanding the interplay between CpG island-associated gene promoters and H3K4 methylation. Biochim Biophys Acta Gene Regul Mech *1863*, 194567.

Ikeda, S., Mizushima, W., Sciarretta, S., Abdellatif, M., Zhai, P., Mukai, R., Fefelova, N., Oka, S.I., Nakamura, M., Del Re, D.P.*, et al.* (2019). Hippo Deficiency Leads to Cardiac Dysfunction Accompanied by Cardiomyocyte Dedifferentiation During Pressure Overload. Circ Res *124*, 292-305.

Ito, S., D'Alessio, A.C., Taranova, O.V., Hong, K., Sowers, L.C., and Zhang, Y. (2010). Role of Tet proteins in 5mC to 5hmC conversion, ES-cell self-renewal and inner cell mass specification. Nature *466*, 1129-1133.

Ito, S., Shen, L., Dai, Q., Wu, S.C., Collins, L.B., Swenberg, J.A., He, C., and Zhang, Y. (2011). Tet proteins can convert 5-methylcytosine to 5-formylcytosine and 5-carboxylcytosine. Science *333*, 1300-1303.

Itoi, T., Huang, L., and Lopaschuk, G.D. (1993). Glucose use in neonatal rabbit hearts reperfused after global ischemia. Am J Physiol *265*, H427-433.

Jezek, P. (2020). 2-Hydroxyglutarate in Cancer Cells. Antioxid Redox Signal *33*, 903-926.

Ji, S., You, Y., Kerner, J., Hoppel, C.L., Schoeb, T.R., Chick, W.S., Hamm, D.A., Sharer, J.D., and Wood, P.A. (2008). Homozygous carnitine palmitoyltransferase 1b (muscle isoform) deficiency is lethal in the mouse. Mol Genet Metab *93*, 314-322.

Jiang, D.S., Yi, X., Li, R., Su, Y.S., Wang, J., Chen, M.L., Liu, L.G., Hu, M., Cheng, C., Zheng, P.*, et al.* (2017). The Histone Methyltransferase Mixed Lineage Leukemia (MLL) 3 May Play a Potential Role on Clinical Dilated Cardiomyopathy. Mol Med *23*, 196-203.

Jiang, Y., Qian, X., Shen, J., Wang, Y., Li, X., Liu, R., Xia, Y., Chen, Q., Peng, G., Lin, S.Y.*, et al.* (2015). Local generation of fumarate promotes DNA repair through inhibition of histone H3 demethylation. Nat Cell Biol *17*, 1158-1168.

Jopling, C., Sune, G., Faucherre, A., Fabregat, C., and Izpisua Belmonte, J.C. (2012). Hypoxia induces myocardial regeneration in zebrafish. Circulation *126*, 3017-3027.

Kang, M.J., Kim, J.S., Chae, S.W., Koh, K.N., and Koh, G.Y. (1997). Cyclins and cyclin dependent kinases during cardiac development. Mol Cells *7*, 360-366.

Karbassi, E., Fenix, A., Marchiano, S., Muraoka, N., Nakamura, K., Yang, X., and Murry, C.E. (2020). Cardiomyocyte maturation: advances in knowledge and implications for regenerative medicine. Nat Rev Cardiol *17*, 341-359.

Karlstaedt, A., Zhang, X., Vitrac, H., Harmancey, R., Vasquez, H., Wang, J.H., Goodell, M.A., and Taegtmeyer, H. (2016). Oncometabolite d-2-hydroxyglutarate impairs alpha-ketoglutarate dehydrogenase and contractile function in rodent heart. Proc Natl Acad Sci U S A *113*, 10436-10441.

Kennedy, J.A., Unger, S.A., and Horowitz, J.D. (1996). Inhibition of carnitine palmitoyltransferase-1 in rat heart and liver by perhexiline and amiodarone. Biochem Pharmacol *52*, 273-280.

Kidder, B.L., Hu, G., and Zhao, K. (2014). KDM5B focuses H3K4 methylation near promoters and enhancers during embryonic stem cell self-renewal and differentiation. Genome Biol *15*, R32.

Kido, M., Du, L., Sullivan, C.C., Li, X., Deutsch, R., Jamieson, S.W., and Thistlethwaite, P.A. (2005). Hypoxia-inducible factor 1-alpha reduces infarction and attenuates progression of cardiac dysfunction after myocardial infarction in the mouse. J Am Coll Cardiol *46*, 2116-2124.

Kim, J., Wende, A.R., Sena, S., Theobald, H.A., Soto, J., Sloan, C., Wayment, B.E., Litwin, S.E., Holzenberger, M., LeRoith, D.*, et al.* (2008). Insulin-like growth factor I receptor signaling is required for exercise-induced cardiac hypertrophy. Mol Endocrinol *22*, 2531-2543.

Kimura, W., Xiao, F., Canseco, D.C., Muralidhar, S., Thet, S., Zhang, H.M., Abderrahman, Y., Chen, R., Garcia, J.A., Shelton, J.M.*, et al.* (2015). Hypoxia fate mapping identifies cycling cardiomyocytes in the adult heart. Nature *523*, 226-230.

King, A., Selak, M.A., and Gottlieb, E. (2006). Succinate dehydrogenase and fumarate hydratase: linking mitochondrial dysfunction and cancer. Oncogene *25*, 4675-4682.

Koitabashi, N., Danner, T., Zaiman, A.L., Pinto, Y.M., Rowell, J., Mankowski, J., Zhang, D., Nakamura, T., Takimoto, E., and Kass, D.A. (2011). Pivotal role of cardiomyocyte TGF-beta signaling in the murine pathological response to sustained pressure overload. J Clin Invest *121*, 2301-2312.

Kolwicz, S.C., Jr., Purohit, S., and Tian, R. (2013). Cardiac metabolism and its interactions with contraction, growth, and survival of cardiomyocytes. Circ Res *113*, 603-616.

Kooistra, S.M., and Helin, K. (2012). Molecular mechanisms and potential functions of histone demethylases. Nat Rev Mol Cell Biol *13*, 297-311.

Kook, H., Lepore, J.J., Gitler, A.D., Lu, M.M., Wing-Man Yung, W., Mackay, J., Zhou, R., Ferrari, V., Gruber, P., and Epstein, J.A. (2003). Cardiac hypertrophy and histone deacetylase-dependent transcriptional repression mediated by the atypical homeodomain protein Hop. J Clin Invest *112*, 863-871.

Kosugi, M., Otani, M., Kikkawa, Y., Itakura, Y., Sakai, K., Ito, T., Toyoda, M., Sekita, Y., and Kimura, T. (2020). Mutations of histone demethylase genes encoded by X and Y chromosomes, Kdm5c and Kdm5d, lead to noncompaction cardiomyopathy in mice. Biochem Biophys Res Commun.

Kuang, M., Febbraio, M., Wagg, C., Lopaschuk, G.D., and Dyck, J.R. (2004). Fatty acid translocase/CD36 deficiency does not energetically or functionally compromise hearts before or after ischemia. Circulation *109*, 1550-1557.

Kubin, T., Poling, J., Kostin, S., Gajawada, P., Hein, S., Rees, W., Wietelmann, A., Tanaka, M., Lorchner, H., Schimanski, S.*, et al.* (2011). Oncostatin M is a major mediator of cardiomyocyte dedifferentiation and remodeling. Cell Stem Cell *9*, 420-432.

Kuhn, B., del Monte, F., Hajjar, R.J., Chang, Y.S., Lebeche, D., Arab, S., and Keating, M.T. (2007). Periostin induces proliferation of differentiated cardiomyocytes and promotes cardiac repair. Nat Med *13*, 962-969.

Kuwahara, F., Kai, H., Tokuda, K., Kai, M., Takeshita, A., Egashira, K., and Imaizumi, T. (2002). Transforming growth factor-beta function blocking prevents myocardial fibrosis and diastolic dysfunction in pressure-overloaded rats. Circulation *106*, 130-135.

Kwon, C., Qian, L., Cheng, P., Nigam, V., Arnold, J., and Srivastava, D. (2009). A regulatory pathway involving Notch1/beta-catenin/Isl1 determines cardiac progenitor cell fate. Nat Cell Biol *11*, 951-957.

Laflamme, M.A., and Murry, C.E. (2011). Heart regeneration. Nature *473*, 326-335.

Larson, A.C., White, R.D., Laub, G., McVeigh, E.R., Li, D., and Simonetti, O.P. (2004). Self-gated cardiac cine MRI. Magn Reson Med *51*, 93-102.

Lauberth, S.M., Nakayama, T., Wu, X., Ferris, A.L., Tang, Z., Hughes, S.H., and Roeder, R.G. (2013). H3K4me3 interactions with TAF3 regulate preinitiation complex assembly and selective gene activation. Cell *152*, 1021-1036.

Leach, J.P., Heallen, T., Zhang, M., Rahmani, M., Morikawa, Y., Hill, M.C., Segura, A., Willerson, J.T., and Martin, J.F. (2017). Hippo pathway deficiency reverses systolic heart failure after infarction. Nature *550*, 260-264.

Leach, J.P., and Martin, J.F. (2018). Cardiomyocyte Proliferation for Therapeutic Regeneration. Curr Cardiol Rep *20*, 63.

Lee, Y., Song, A.J., Baker, R., Micales, B., Conway, S.J., and Lyons, G.E. (2000). Jumonji, a nuclear protein that is necessary for normal heart development. Circ Res *86*, 932-938.

Lescroart, F., Chabab, S., Lin, X., Rulands, S., Paulissen, C., Rodolosse, A., Auer, H., Achouri, Y., Dubois, C., Bondue, A.*, et al.* (2014). Early lineage restriction in temporally distinct populations of Mesp1 progenitors during mammalian heart development. Nat Cell Biol *16*, 829-840.

Li, E., and Zhang, Y. (2014). DNA methylation in mammals. Cold Spring Harb Perspect Biol *6*, a019133.

Li, F., Wang, X., Capasso, J.M., and Gerdes, A.M. (1996). Rapid transition of cardiac myocytes from hyperplasia to hypertrophy during postnatal development. J Mol Cell Cardiol *28*, 1737-1746.

Li, X., Pei, D., and Zheng, H. (2014). Transitions between epithelial and mesenchymal states during cell fate conversions. Protein Cell *5*, 580-591.

Li, X., Yue, X., Pastor, W.A., Lin, L., Georges, R., Chavez, L., Evans, S.M., and Rao, A. (2016). Tet proteins influence the balance between neuroectodermal and mesodermal fate choice by inhibiting Wnt signaling. Proc Natl Acad Sci U S A *113*, E8267-E8276.

Lin, Z., Guo, H., Cao, Y., Zohrabian, S., Zhou, P., Ma, Q., VanDusen, N., Guo, Y., Zhang, J., Stevens, S.M.*, et al.* (2016). Acetylation of VGLL4 Regulates Hippo-YAP Signaling and Postnatal Cardiac Growth. Dev Cell *39*, 466-479.

Lionetti, V., Linke, A., Chandler, M.P., Young, M.E., Penn, M.S., Gupte, S., d'Agostino, C., Hintze, T.H., Stanley, W.C., and Recchia, F.A. (2005). Carnitine palmitoyl transferase-I inhibition prevents ventricular remodeling and delays decompensation in pacing-induced heart failure. Cardiovasc Res *66*, 454-461.

Liu, J., Laksman, Z., and Backx, P.H. (2016a). The electrophysiological development of cardiomyocytes. Adv Drug Deliv Rev *96*, 253-273.

Liu, L., Lei, I., Karatas, H., Li, Y., Wang, L., Gnatovskiy, L., Dou, Y., Wang, S., Qian, L., and Wang, Z. (2016b). Targeting Mll1 H3K4 methyltransferase activity to guide cardiac lineage specific reprogramming of fibroblasts. Cell Discov *2*, 16036.

Liu, P., Chen, S., Li, X., Qin, L., Huang, K., Wang, L., Huang, W., Li, S., Jia, B., Zhong, M.*, et al.* (2013). Low immunogenicity of neural progenitor cells differentiated from induced pluripotent stem cells derived from less immunogenic somatic cells. PLoS One *8*, e69617.

Lopaschuk, G.D., and Jaswal, J.S. (2010). Energy metabolic phenotype of the cardiomyocyte during development, differentiation, and postnatal maturation. J Cardiovasc Pharmacol *56*, 130-140.

Lopaschuk, G.D., and Spafford, M.A. (1992). Differences in myocardial ischemic tolerance between 1- and 7-day-old rabbits. Can J Physiol Pharmacol *70*, 1315-1323.

Lopaschuk, G.D., Spafford, M.A., and Marsh, D.R. (1991). Glycolysis is predominant source of myocardial ATP production immediately after birth. Am J Physiol *261*, H1698-1705.

Lopaschuk, G.D., Wambolt, R.B., and Barr, R.L. (1993). An imbalance between glycolysis and glucose oxidation is a possible explanation for the detrimental effects of high levels of fatty acids during aerobic reperfusion of ischemic hearts. J Pharmacol Exp Ther *264*, 135-144.

Lopez-Sanchez, C., and Garcia-Martinez, V. (2011). Molecular determinants of cardiac specification. Cardiovasc Res *91*, 185-195.

Lorchner, H., Poling, J., Gajawada, P., Hou, Y., Polyakova, V., Kostin, S., Adrian-Segarra, J.M., Boettger, T., Wietelmann, A., Warnecke, H.*, et al.* (2015). Myocardial healing requires Reg3beta-dependent accumulation of macrophages in the ischemic heart. Nat Med *21*, 353-362.

Lydell, C.P., Chan, A., Wambolt, R.B., Sambandam, N., Parsons, H., Bondy, G.P., Rodrigues, B., Popov, K.M., Harris, R.A., Brownsey, R.W.*, et al.* (2002). Pyruvate dehydrogenase and the regulation of glucose oxidation in hypertrophied rat hearts. Cardiovasc Res *53*, 841-851.

Ma, Y., Wang, W., Devarakonda, T., Zhou, H., Wang, X.Y., Salloum, F.N., Spiegel, S., and Fang, X. (2020). Functional analysis of molecular and pharmacological modulators of mitochondrial fatty acid oxidation. Sci Rep *10*, 1450.

MacGrogan, D., Munch, J., and de la Pompa, J.L. (2018). Notch and interacting signalling pathways in cardiac development, disease, and regeneration. Nat Rev Cardiol *15*, 685-704.

Madsen, A., Hoppner, G., Krause, J., Hirt, M.N., Laufer, S.D., Schweizer, M., Tan, W.L.W., Mosqueira, D., Anene-Nzelu, C.G., Lim, I.*, et al.* (2020). An Important Role for DNMT3A-Mediated DNA Methylation in Cardiomyocyte Metabolism and Contractility. Circulation *142*, 1562-1578.

Magadum, A., Singh, N., Kurian, A.A., Munir, I., Mehmood, T., Brown, K., Sharkar, M.T.K., Chepurko, E., Sassi, Y., Oh, J.G.*, et al.* (2020). Pkm2 Regulates Cardiomyocyte Cell Cycle and Promotes Cardiac Regeneration. Circulation *141*, 1249-1265.

Mahdavi, V., Lompre, A.M., Chambers, A.P., and Nadal-Ginard, B. (1984). Cardiac myosin heavy chain isozymic transitions during development and under pathological conditions are regulated at the level of mRNA availability. Eur Heart J *5 Suppl F*, 181-191.

Mahmoud, A.I., Kocabas, F., Muralidhar, S.A., Kimura, W., Koura, A.S., Thet, S., Porrello, E.R., and Sadek, H.A. (2013). Meis1 regulates postnatal cardiomyocyte cell cycle arrest. Nature *497*, 249-253.

Makinde, A.O., Kantor, P.F., and Lopaschuk, G.D. (1998). Maturation of fatty acid and carbohydrate metabolism in the newborn heart. Mol Cell Biochem *188*, 49-56.

Margueron, R., and Reinberg, D. (2010). Chromatin structure and the inheritance of epigenetic information. Nat Rev Genet *11*, 285-296.

Martinez-Chantar, M.L., Vazquez-Chantada, M., Ariz, U., Martinez, N., Varela, M., Luka, Z., Capdevila, A., Rodriguez, J., Aransay, A.M., Matthiesen, R.*, et al.* (2008). Loss of the glycine N-methyltransferase gene leads to steatosis and hepatocellular carcinoma in mice. Hepatology *47*, 1191-1199.

McCommis, K.S., Kovacs, A., Weinheimer, C.J., Shew, T.M., Koves, T.R., Ilkayeva, O.R., Kamm, D.R., Pyles, K.D., King, M.T., Veech, R.L.*, et al.* (2020). Nutritional modulation of heart failure in mitochondrial pyruvate carrier-deficient mice. Nat Metab *2*, 1232-1247.

McMullen, J.R., Shioi, T., Huang, W.Y., Zhang, L., Tarnavski, O., Bisping, E., Schinke, M., Kong, S., Sherwood, M.C., Brown, J.*, et al.* (2004). The insulin-like growth factor 1 receptor induces physiological heart growth via the phosphoinositide 3-kinase(p110alpha) pathway. J Biol Chem *279*, 4782-4793.

Mentch, S.J., Mehrmohamadi, M., Huang, L., Liu, X., Gupta, D., Mattocks, D., Gomez Padilla, P., Ables, G., Bamman, M.M., Thalacker-Mercer, A.E.*, et al.* (2015). Histone Methylation Dynamics and Gene Regulation Occur through the Sensing of One-Carbon Metabolism. Cell Metab *22*, 861-873.

Meyfour, A., Pahlavan, S., Ansari, H., Baharvand, H., and Salekdeh, G.H. (2019). Down-Regulation of a Male-Specific H3K4 Demethylase, KDM5D, Impairs Cardiomyocyte Differentiation. J Proteome Res *18*, 4277-4282.

Michalak, E.M., Burr, M.L., Bannister, A.J., and Dawson, M.A. (2019). The roles of DNA, RNA and histone methylation in ageing and cancer. Nat Rev Mol Cell Biol *20*, 573-589.

Mohamed, T.M.A., Ang, Y.S., Radzinsky, E., Zhou, P., Huang, Y., Elfenbein, A., Foley, A., Magnitsky, S., and Srivastava, D. (2018). Regulation of Cell Cycle to Stimulate Adult Cardiomyocyte Proliferation and Cardiac Regeneration. Cell *173*, 104-116 e112.

Mohammed, S.F., Hussain, S., Mirzoyev, S.A., Edwards, W.D., Maleszewski, J.J., and Redfield, M.M. (2015). Coronary microvascular rarefaction and myocardial fibrosis in heart failure with preserved ejection fraction. Circulation *131*, 550-559.

Mollova, M., Bersell, K., Walsh, S., Savla, J., Das, L.T., Park, S.Y., Silberstein, L.E., Dos Remedios, C.G., Graham, D., Colan, S.*, et al.* (2013). Cardiomyocyte proliferation contributes to heart growth in young humans. Proc Natl Acad Sci U S A *110*, 1446-1451.

Morikawa, Y., Heallen, T., Leach, J., Xiao, Y., and Martin, J.F. (2017). Dystrophin-glycoprotein complex sequesters Yap to inhibit cardiomyocyte proliferation. Nature *547*, 227-231.

Murakami, M., Nakagawa, M., Olson, E.N., and Nakagawa, O. (2005). A WW domain protein TAZ is a critical coactivator for TBX5, a transcription factor implicated in Holt-Oram syndrome. Proc Natl Acad Sci U S A *102*, 18034-18039.

Nagaraj, R., Sharpley, M.S., Chi, F., Braas, D., Zhou, Y., Kim, R., Clark, A.T., and Banerjee, U. (2017). Nuclear Localization of Mitochondrial TCA Cycle Enzymes as a Critical Step in Mammalian Zygotic Genome Activation. Cell *168*, 210-223 e211.

Nahrendorf, M. (2018). Myeloid cell contributions to cardiovascular health and disease. Nat Med *24*, 711-720.

Nakada, Y., Canseco, D.C., Thet, S., Abdisalaam, S., Asaithamby, A., Santos, C.X., Shah, A., Zhang, H., Faber, J.E., Kinter, M.T.*, et al.* (2016). Hypoxia induces heart regeneration in adult mice. Nature.

Nakamura, M., and Sadoshima, J. (2018). Mechanisms of physiological and pathological cardiac hypertrophy. Nat Rev Cardiol.

Neri, F., Rapelli, S., Krepelova, A., Incarnato, D., Parlato, C., Basile, G., Maldotti, M., Anselmi, F., and Oliviero, S. (2017). Intragenic DNA methylation prevents spurious transcription initiation. Nature.

Neri Serneri, G.G., Boddi, M., Modesti, P.A., Cecioni, I., Coppo, M., Padeletti, L., Michelucci, A., Colella, A., and Galanti, G. (2001). Increased cardiac sympathetic activity and insulin-like growth factor-I formation are associated with physiological hypertrophy in athletes. Circ Res *89*, 977-982.

Nguyen, A.T., Xiao, B., Neppl, R.L., Kallin, E.M., Li, J., Chen, T., Wang, D.Z., Xiao, X., and Zhang, Y. (2011). DOT1L regulates dystrophin expression and is critical for cardiac function. Genes Dev *25*, 263-274.

Nuhrenberg, T.G., Hammann, N., Schnick, T., Preissl, S., Witten, A., Stoll, M., Gilsbach, R., Neumann, F.J., and Hein, L. (2015). Cardiac Myocyte De Novo DNA Methyltransferases 3a/3b Are Dispensable for Cardiac Function and Remodeling after Chronic Pressure Overload in Mice. PLoS One *10*, e0131019.

O'Connell, T.D., Rodrigo, M.C., and Simpson, P.C. (2007). Isolation and culture of adult mouse cardiac myocytes. Methods Mol Biol *357*, 271-296.

Oka, T., Akazawa, H., Naito, A.T., and Komuro, I. (2014). Angiogenesis and cardiac hypertrophy: maintenance of cardiac function and causative roles in heart failure. Circ Res *114*, 565-571.

Okano, M., Bell, D.W., Haber, D.A., and Li, E. (1999). DNA methyltransferases Dnmt3a and Dnmt3b are essential for de novo methylation and mammalian development. Cell *99*, 247-257.

Okano, M., Xie, S., and Li, E. (1998). Cloning and characterization of a family of novel mammalian DNA (cytosine-5) methyltransferases. Nat Genet *19*, 219-220.

Olenchock, B.A., Moslehi, J., Baik, A.H., Davidson, S.M., Williams, J., Gibson, W.J., Chakraborty, A.A., Pierce, K.A., Miller, C.M., Hanse, E.A.*, et al.* (2016). EGLN1 Inhibition and Rerouting of alpha-Ketoglutarate Suffice for Remote Ischemic Protection. Cell *164*, 884-895.

Olson, E.N. (2006). Gene regulatory networks in the evolution and development of the heart. Science *313*, 1922-1927.

Olszanecka, A., Dragan, A., Kawecka-Jaszcz, K., Fedak, D., and Czarnecka, D. (2017). Relationships of insulin-like growth factor-1, its binding proteins, and cardiometabolic risk in hypertensive perimenopausal women. Metabolism *69*, 96-106.

Omede, A., Zi, M., Prehar, S., Maqsood, A., Stafford, N., Mamas, M., Cartwright, E., and Oceandy, D. (2016). The oxoglutarate receptor 1 (OXGR1) modulates pressure overload-induced cardiac hypertrophy in mice. Biochem Biophys Res Commun *479*, 708-714.

Opie, L.H., and Knuuti, J. (2009). The adrenergic-fatty acid load in heart failure. J Am Coll Cardiol *54*, 1637-1646.

Palmer, J.W., Tandler, B., and Hoppel, C.L. (1977). Biochemical properties of subsarcolemmal and interfibrillar mitochondria isolated from rat cardiac muscle. J Biol Chem *252*, 8731-8739.

Pasumarthi, K.B., Nakajima, H., Nakajima, H.O., Soonpaa, M.H., and Field, L.J. (2005). Targeted expression of cyclin D2 results in cardiomyocyte DNA synthesis and infarct regression in transgenic mice. Circ Res *96*, 110-118.

Patel, M.S. (1974). Inhibition by the branched-chain 2-oxo acids of the 2-oxoglutarate dehydrogenase complex in developing rat and human brain. Biochem J *144*, 91-97.

Patterson, M., Barske, L., Van Handel, B., Rau, C.D., Gan, P., Sharma, A., Parikh, S., Denholtz, M., Huang, Y., Yamaguchi, Y.*, et al.* (2017). Frequency of mononuclear diploid cardiomyocytes underlies natural variation in heart regeneration. Nat Genet *49*, 1346-1353.

Perrino, C., Naga Prasad, S.V., Mao, L., Noma, T., Yan, Z., Kim, H.S., Smithies, O., and Rockman, H.A. (2006). Intermittent pressure overload triggers hypertrophy-independent cardiac dysfunction and vascular rarefaction. J Clin Invest *116*, 1547-1560.

Peuhkurinen, K.J., Takala, T.E., Nuutinen, E.M., and Hassinen, I.E. (1983). Tricarboxylic acid cycle metabolites during ischemia in isolated perfused rat heart. Am J Physiol *244*, H281-288.

Pietrocola, F., Galluzzi, L., Bravo-San Pedro, J.M., Madeo, F., and Kroemer, G. (2015). Acetyl coenzyme A: a central metabolite and second messenger. Cell Metab *21*, 805-821.

Pinto, A.R., Ilinykh, A., Ivey, M.J., Kuwabara, J.T., D'Antoni, M.L., Debuque, R., Chandran, A., Wang, L., Arora, K., Rosenthal, N.A.*, et al.* (2016). Revisiting Cardiac Cellular Composition. Circ Res *118*, 400-409.

Polizzotti, B.D., Arab, S., and Kuhn, B. (2012). Intrapericardial delivery of gelfoam enables the targeted delivery of Periostin peptide after myocardial infarction by inducing fibrin clot formation. PLoS One *7*, e36788.

Pound, K.M., Sorokina, N., Ballal, K., Berkich, D.A., Fasano, M., Lanoue, K.F., Taegtmeyer, H., O'Donnell, J.M., and Lewandowski, E.D. (2009). Substrate-enzyme competition attenuates upregulated anaplerotic flux through malic enzyme in hypertrophied rat heart and restores triacylglyceride content: attenuating upregulated anaplerosis in hypertrophy. Circ Res *104*, 805-812.

Puente, B.N., Kimura, W., Muralidhar, S.A., Moon, J., Amatruda, J.F., Phelps, K.L., Grinsfelder, D., Rothermel, B.A., Chen, R., Garcia, J.A.*, et al.* (2014). The oxygen-rich postnatal environment induces cardiomyocyte cell-cycle arrest through DNA damage response. Cell *157*, 565-579.

Quaife-Ryan, G.A., Sim, C.B., Porrello, E.R., and Hudson, J.E. (2016). Resetting the epigenome for heart regeneration. Semin Cell Dev Biol *58*, 2-13.

Rainer, P.P., and Kass, D.A. (2016). Old dog, new tricks: novel cardiac targets and stress regulation by protein kinase G. Cardiovasc Res *111*, 154-162.

Randle, P.J., Garland, P.B., Hales, C.N., and Newsholme, E.A. (1963). The glucose fatty-acid cycle. Its role in insulin sensitivity and the metabolic disturbances of diabetes mellitus. Lancet *1*, 785-789.

Rastogi, S., Sharov, V.G., Mishra, S., Gupta, R.C., Blackburn, B., Belardinelli, L., Stanley, W.C., and Sabbah, H.N. (2008). Ranolazine combined with enalapril or metoprolol prevents progressive LV dysfunction and remodeling in dogs with moderate heart failure. Am J Physiol Heart Circ Physiol *295*, H2149-2155.

Richardson, G.D. (2016). Simultaneous Assessment of Cardiomyocyte DNA Synthesis and Ploidy: A Method to Assist Quantification of Cardiomyocyte Regeneration and Turnover. J Vis Exp.

Riggs, A.D. (1975). X inactivation, differentiation, and DNA methylation. Cytogenet Cell Genet *14*, 9-25.

Sabry, M.A., and Dhoot, G.K. (1989). Identification and pattern of expression of a developmental isoform of troponin I in chicken and rat cardiac muscle. J Muscle Res Cell Motil *10*, 85-91.

Sack, M.N., Rader, T.A., Park, S., Bastin, J., McCune, S.A., and Kelly, D.P. (1996). Fatty acid oxidation enzyme gene expression is downregulated in the failing heart. Circulation *94*, 2837-2842.

Sadoshima, J., and Izumo, S. (1995). Rapamycin selectively inhibits angiotensin II-induced increase in protein synthesis in cardiac myocytes in vitro. Potential role of 70-kD S6 kinase in angiotensin II-induced cardiac hypertrophy. Circ Res *77*, 1040-1052.

Saks, V., Kuznetsov, A.V., Gonzalez-Granillo, M., Tepp, K., Timohhina, N., Karu-Varikmaa, M., Kaambre, T., Dos Santos, P., Boucher, F., and Guzun, R. (2012). Intracellular Energetic Units regulate metabolism in cardiac cells. J Mol Cell Cardiol *52*, 419-436.

Sassoli, C., Chellini, F., Pini, A., Tani, A., Nistri, S., Nosi, D., Zecchi-Orlandini, S., Bani, D., and Formigli, L. (2013). Relaxin prevents cardiac fibroblast-myofibroblast transition via notch-1-mediated inhibition of TGF-beta/Smad3 signaling. PLoS One *8*, e63896.

Schaper, J., Meiser, E., and Stammler, G. (1985). Ultrastructural morphometric analysis of myocardium from dogs, rats, hamsters, mice, and from human hearts. Circ Res *56*, 377-391.

Schiattarella, G.G., and Hill, J.A. (2015). Inhibition of hypertrophy is a good therapeutic strategy in ventricular pressure overload. Circulation *131*, 1435-1447.

Schoors, S., Bruning, U., Missiaen, R., Queiroz, K.C., Borgers, G., Elia, I., Zecchin, A., Cantelmo, A.R., Christen, S., Goveia, J*., et al.* (2015). Fatty acid carbon is essential for dNTP synthesis in endothelial cells. Nature *520*, 192-197.

Scuderi, G.J., and Butcher, J. (2017). Naturally Engineered Maturation of Cardiomyocytes. Front Cell Dev Biol *5*, 50.

Senyo, S.E., Steinhauser, M.L., Pizzimenti, C.L., Yang, V.K., Cai, L., Wang, M., Wu, T.D., Guerquin-Kern, J.L., Lechene, C.P., and Lee, R.T. (2013). Mammalian heart renewal by pre-existing cardiomyocytes. Nature *493*, 433-436.

Sharma, S., Adrogue, J.V., Golfman, L., Uray, I., Lemm, J., Youker, K., Noon, G.P., Frazier, O.H., and Taegtmeyer, H. (2004). Intramyocardial lipid accumulation in the failing human heart resembles the lipotoxic rat heart. FASEB J *18*, 1692-1700.

Shioi, T., McMullen, J.R., Tarnavski, O., Converso, K., Sherwood, M.C., Manning, W.J., and Izumo, S. (2003). Rapamycin attenuates load-induced cardiac hypertrophy in mice. Circulation *107*, 1664-1670.

Soonpaa, M.H., Kim, K.K., Pajak, L., Franklin, M., and Field, L.J. (1996). Cardiomyocyte DNA synthesis and binucleation during murine development. Am J Physiol *271*, H2183-2189.

Soonpaa, M.H., Koh, G.Y., Pajak, L., Jing, S., Wang, H., Franklin, M.T., Kim, K.K., and Field, L.J. (1997). Cyclin D1 overexpression promotes cardiomyocyte DNA synthesis and multinucleation in transgenic mice. J Clin Invest *99*, 2644-2654.

Sorokina, N., O'Donnell, J.M., McKinney, R.D., Pound, K.M., Woldegiorgis, G., LaNoue, K.F., Ballal, K., Taegtmeyer, H., Buttrick, P.M., and Lewandowski, E.D. (2007). Recruitment of compensatory pathways to sustain oxidative flux with reduced carnitine palmitoyltransferase I activity characterizes inefficiency in energy metabolism in hypertrophied hearts. Circulation *115*, 2033-2041.

Srivastava, D. (2006). Making or breaking the heart: from lineage determination to morphogenesis. Cell *126*, 1037-1048.

Stanley, W.C., Morgan, E.E., Huang, H., McElfresh, T.A., Sterk, J.P., Okere, I.C., Chandler, M.P., Cheng, J., Dyck, J.R., and Lopaschuk, G.D. (2005a). Malonyl-CoA decarboxylase inhibition suppresses fatty acid oxidation and reduces lactate production during demand-induced ischemia. Am J Physiol Heart Circ Physiol *289*, H2304-2309.

Stanley, W.C., Recchia, F.A., and Lopaschuk, G.D. (2005b). Myocardial substrate metabolism in the normal and failing heart. Physiol Rev *85*, 1093-1129.

Su, R., Dong, L., Li, C., Nachtergaele, S., Wunderlich, M., Qing, Y., Deng, X., Wang, Y., Weng, X., Hu, C.*, et al.* (2018). R-2HG Exhibits Anti-tumor Activity by Targeting FTO/m(6)A/MYC/CEBPA Signaling. Cell *172*, 90-105 e123.

Sulkowski, P.L., Oeck, S., Dow, J., Economos, N.G., Mirfakhraie, L., Liu, Y., Noronha, K., Bao, X., Li, J., Shuch, B.M.*, et al.* (2020). Oncometabolites suppress DNA repair by disrupting local chromatin signalling. Nature.

Sutendra, G., Kinnaird, A., Dromparis, P., Paulin, R., Stenson, T.H., Haromy, A., Hashimoto, K., Zhang, N., Flaim, E., and Michelakis, E.D. (2014). A nuclear pyruvate dehydrogenase complex is important for the generation of acetyl-CoA and histone acetylation. Cell *158*, 84-97.

Suurmeijer, A.J., Clement, S., Francesconi, A., Bocchi, L., Angelini, A., Van Veldhuisen, D.J., Spagnoli, L.G., Gabbiani, G., and Orlandi, A. (2003). Alpha-actin isoform distribution in normal and failing human heart: a morphological, morphometric, and biochemical study. J Pathol *199*, 387-397.

Swan, J.W., Anker, S.D., Walton, C., Godsland, I.F., Clark, A.L., Leyva, F., Stevenson, J.C., and Coats, A.J. (1997). Insulin resistance in chronic heart failure: relation to severity and etiology of heart failure. J Am Coll Cardiol *30*, 527-532.

Sze, C.C., Ozark, P.A., Cao, K., Ugarenko, M., Das, S., Wang, L., Marshall, S.A., Rendleman, E.J., Ryan, C.A., Zha, D.*, et al.* (2020). Coordinated regulation of cellular identity-associated H3K4me3 breadth by the COMPASS family. Sci Adv *6*, eaaz4764.

Taegtmeyer, H., Golfman, L., Sharma, S., Razeghi, P., and van Arsdall, M. (2004). Linking gene expression to function: metabolic flexibility in the normal and diseased heart. Ann N Y Acad Sci *1015*, 202-213.

Tahiliani, M., Koh, K.P., Shen, Y., Pastor, W.A., Bandukwala, H., Brudno, Y., Agarwal, S., Iyer, L.M., Liu, D.R., Aravind, L.*, et al.* (2009). Conversion of 5-methylcytosine to 5-hydroxymethylcytosine in mammalian DNA by MLL partner TET1. Science *324*, 930-935.

Tam, P.P., Parameswaran, M., Kinder, S.J., and Weinberger, R.P. (1997). The allocation of epiblast cells to the embryonic heart and other mesodermal lineages: the role of ingression and tissue movement during gastrulation. Development *124*, 1631-1642.

TeSlaa, T., Chaikovsky, A.C., Lipchina, I., Escobar, S.L., Hochedlinger, K., Huang, J., Graeber, T.G., Braas, D., and Teitell, M.A. (2016). alpha-Ketoglutarate Accelerates the Initial Differentiation of Primed Human Pluripotent Stem Cells. Cell Metab *24*, 485-493.

Thirstrup, K., Christensen, S., Moller, H.A., Ritzen, A., Bergstrom, A.L., Sager, T.N., and Jensen, H.S. (2011). Endogenous 2-oxoglutarate levels impact potencies of competitive HIF prolyl hydroxylase inhibitors. Pharmacol Res *64*, 268-273.

Tran, T.Q., Hanse, E.A., Habowski, A.N., Li, H., Gabra, M.B.I., Yang, Y., Lowman, X.H., Ooi, A.M., Liao, S.Y., Edwards, R.A.*, et al.* (2020). alpha-Ketoglutarate attenuates Wnt signaling and drives differentiation in colorectal cancer. Nat Cancer *1*, 345-358.

Trivedi, C.M., Lu, M.M., Wang, Q., and Epstein, J.A. (2008). Transgenic overexpression of Hdac3 in the heart produces increased postnatal cardiac myocyte proliferation but does not induce hypertrophy. J Biol Chem *283*, 26484-26489.

Turkbey, E.B., McClelland, R.L., Kronmal, R.A., Burke, G.L., Bild, D.E., Tracy, R.P., Arai, A.E., Lima, J.A., and Bluemke, D.A. (2010). The impact of obesity on the left ventricle: the Multi-Ethnic Study of Atherosclerosis (MESA). JACC Cardiovasc Imaging *3*, 266-274.

Tuunanen, H., Engblom, E., Naum, A., Nagren, K., Hesse, B., Airaksinen, K.E., Nuutila, P., Iozzo, P., Ukkonen, H., Opie, L.H.*, et al.* (2006). Free fatty acid depletion acutely decreases cardiac work and efficiency in cardiomyopathic heart failure. Circulation *114*, 2130-2137.

Vandekerckhove, J., Bugaisky, G., and Buckingham, M. (1986). Simultaneous expression of skeletal muscle and heart actin proteins in various striated muscle tissues and cells. A quantitative determination of the two actin isoforms. J Biol Chem *261*, 1838-1843.

Vega, R.B., Konhilas, J.P., Kelly, D.P., and Leinwand, L.A. (2017). Molecular Mechanisms Underlying Cardiac Adaptation to Exercise. Cell Metab *25*, 1012-1026.

von Gise, A., Lin, Z., Schlegelmilch, K., Honor, L.B., Pan, G.M., Buck, J.N., Ma, Q., Ishiwata, T., Zhou, B., Camargo, F.D.*, et al.* (2012). YAP1, the nuclear target of Hippo signaling, stimulates heart growth through cardiomyocyte proliferation but not hypertrophy. Proc Natl Acad Sci U S A *109*, 2394-2399.

Wan, X., Liu, L., Ding, X., Zhou, P., Yuan, X., Zhou, Z., Hu, P., Zhou, H., Li, Q., Zhang, S.*, et al.* (2014). Mll2 controls cardiac lineage differentiation of mouse embryonic stem cells by promoting H3K4me3 deposition at cardiac-specific genes. Stem Cell Rev Rep *10*, 643-652.

Wang, J., Liu, S., Heallen, T., and Martin, J.F. (2018). The Hippo pathway in the heart: pivotal roles in development, disease, and regeneration. Nat Rev Cardiol *15*, 672-684.

Wang, Y., Wu, B., Chamberlain, A.A., Lui, W., Koirala, P., Susztak, K., Klein, D., Taylor, V., and Zhou, B. (2013). Endocardial to myocardial notch-wnt-bmp axis regulates early heart valve development. PLoS One *8*, e60244.

Weber, K.T., Sun, Y., Bhattacharya, S.K., Ahokas, R.A., and Gerling, I.C. (2013). Myofibroblast-mediated mechanisms of pathological remodelling of the heart. Nat Rev Cardiol *10*, 15-26.

Wellen, K.E., Hatzivassiliou, G., Sachdeva, U.M., Bui, T.V., Cross, J.R., and Thompson, C.B. (2009). ATP-citrate lyase links cellular metabolism to histone acetylation. Science *324*, 1076-1080.

Werner, J.C., Sicard, R.E., and Schuler, H.G. (1989). Palmitate oxidation by isolated working fetal and newborn pig hearts. Am J Physiol *256*, E315-321.

Wilcox, J.E., Fonarow, G.C., Ardehali, H., Bonow, R.O., Butler, J., Sauer, A.J., Epstein, S.E., Khan, S.S., Kim, R.J., Sabbah, H.N.*, et al.* (2015). "Targeting the Heart" in Heart Failure: Myocardial Recovery in Heart Failure With Reduced Ejection Fraction. JACC Heart Fail *3*, 661-669.

Wu, T.T., Ma, Y.W., Zhang, X., Dong, W., Gao, S., Wang, J.Z., Zhang, L.F., and Lu, D. (2020). Myocardial tissue-specific Dnmt1 knockout in rats protects against pathological injury induced by Adriamycin. Lab Invest *100*, 974-985.

Xiao, D., Zeng, L., Yao, K., Kong, X., Wu, G., and Yin, Y. (2016). The glutamine-alpha-ketoglutarate (AKG) metabolism and its nutritional implications. Amino Acids *48*, 2067-2080.

Xiao, M., Yang, H., Xu, W., Ma, S., Lin, H., Zhu, H., Liu, L., Liu, Y., Yang, C., Xu, Y.*, et al.* (2012). Inhibition of alpha-KG-dependent histone and DNA demethylases by fumarate and succinate that are accumulated in mutations of FH and SDH tumor suppressors. Genes Dev *26*, 1326-1338.

Xie, L., Pelz, C., Wang, W., Bashar, A., Varlamova, O., Shadle, S., and Impey, S. (2011). KDM5B regulates embryonic stem cell self-renewal and represses cryptic intragenic transcription. EMBO J *30*, 1473-1484.

Xin, M., Kim, Y., Sutherland, L.B., Murakami, M., Qi, X., McAnally, J., Porrello, E.R., Mahmoud, A.I., Tan, W., Shelton, J.M.*, et al.* (2013a). Hippo pathway effector Yap promotes cardiac regeneration. Proc Natl Acad Sci U S A *110*, 13839-13844.

Xin, M., Kim, Y., Sutherland, L.B., Qi, X., McAnally, J., Schwartz, R.J., Richardson, J.A., Bassel-Duby, R., and Olson, E.N. (2011). Regulation of insulin-like growth factor signaling by Yap governs cardiomyocyte proliferation and embryonic heart size. Sci Signal *4*, ra70.

Xin, M., Olson, E.N., and Bassel-Duby, R. (2013b). Mending broken hearts: cardiac development as a basis for adult heart regeneration and repair. Nat Rev Mol Cell Biol *14*, 529-541.

Yanazume, T., Hasegawa, K., Morimoto, T., Kawamura, T., Wada, H., Matsumori, A., Kawase, Y., Hirai, M., and Kita, T. (2003a). Cardiac p300 is involved in myocyte growth with decompensated heart failure. Mol Cell Biol *23*, 3593-3606.

Yanazume, T., Morimoto, T., Wada, H., Kawamura, T., and Hasegawa, K. (2003b). Biological role of p300 in cardiac myocytes. Mol Cell Biochem *248*, 115-119.

Yang, X., Pabon, L., and Murry, C.E. (2014). Engineering adolescence: maturation of human pluripotent stem cell-derived cardiomyocytes. Circ Res *114*, 511-523.

Yuan, X., and Braun, T. (2013). An unexpected switch: regulation of cardiomyocyte proliferation by the homeobox gene meis1. Circ Res *113*, 245-248.

Yuan, X., and Braun, T. (2017). Multimodal Regulation of Cardiac Myocyte Proliferation. Circ Res *121*, 293-309.

Yue, Q., Wagstaff, L., Yang, X., Weijer, C., and Munsterberg, A. (2008). Wnt3a-mediated chemorepulsion controls movement patterns of cardiac progenitors and requires RhoA function. Development *135*, 1029-1037.

Zaidi, S., Choi, M., Wakimoto, H., Ma, L., Jiang, J., Overton, J.D., Romano-Adesman, A., Bjornson, R.D., Breitbart, R.E., Brown, K.K.*, et al.* (2013). De novo mutations in histone-modifying genes in congenital heart disease. Nature *498*, 220-223.

Zhang, D., Contu, R., Latronico, M.V., Zhang, J., Rizzi, R., Catalucci, D., Miyamoto, S., Huang, K., Ceci, M., Gu, Y.*, et al.* (2010). MTORC1 regulates cardiac function and myocyte survival through 4E-BP1 inhibition in mice. J Clin Invest *120*, 2805-2816.

Zhang, D., Gaussin, V., Taffet, G.E., Belaguli, N.S., Yamada, M., Schwartz, R.J., Michael, L.H., Overbeek, P.A., and Schneider, M.D. (2000). TAK1 is activated in the myocardium after pressure overload and is sufficient to provoke heart failure in transgenic mice. Nat Med *6*, 556-563.

Zhang, D., Wang, Y., Lu, P., Wang, P., Yuan, X., Yan, J., Cai, C., Chang, C.P., Zheng, D., Wu, B.*, et al.* (2017). REST regulates the cell cycle for cardiac development and regeneration. Nat Commun *8*, 1979.

Zhang, L., Malik, S., Pang, J., Wang, H., Park, K.M., Yule, D.I., Blaxall, B.C., and Smrcka, A.V. (2013). Phospholipase Cepsilon hydrolyzes perinuclear phosphatidylinositol 4-phosphate to regulate cardiac hypertrophy. Cell *153*, 216-227.

Zhang, Y., Taufalele, P.V., Cochran, J.D., Robillard-Frayne, I., Marx, J.M., Soto, J., Rauckhorst, A.J., Tayyari, F., Pewa, A.D., Gray, L.R*., et al.* (2020). Mitochondrial pyruvate carriers are required for myocardial stress adaptation. Nat Metab *2*, 1248-1264.

Zhou, Y., Kim, J., Yuan, X., and Braun, T. (2011). Epigenetic modifications of stem cells: a paradigm for the control of cardiac progenitor cells. Circ Res *109*, 1067-1081.

Zlotorynski, E. (2017). Gene expression: ACSS2 boosts local histone acetylation. Nat Rev Mol Cell Biol *18*, 405.

List of figures

Acknowledgments

This work was carried out at Max Planck Institute for Heart and Lung Research in Bad Nauheim, Germany. First, I would like to express my gratitude to my Ph.D. supervisor Prof. Dr. Dr. Thomas Braun, for providing me with this valuable opportunity to pursue my Ph.D. study. His excellent knowledge and outstanding scientific ideas impressed me deeply. Throughout my Ph.D. life, he supported and motivated me to develop ideas for scientific research projects rigorously, learn and try fascinating techniques freely, and establish collaboration with superior scientists bravely. I am grateful that I could have the opportunity to work with Dr. Yonggang Zhou. He is a role model for all of us. He taught me how to fight failure in both scientific and everyday life. His optimistic attitude towards life encouraged me to keep fighting during the darkest time. I would like to express my gratitude to my Ph.D. supervisor Dr. Xuejun Yuan. She motivated and supported me during the development of this project. She could always convince me to solve critical issues from an inspiring perspective. She is always an excellent friend and gives us a lot of encouragement and unconditional supports for our life. Her patience and diligence facilitated the progression of this project. I express my appreciation to Prof. Dr. Reinhard Dammann for his willingness to be my second corrector and for his valuable advice as my thesis committee. Thanks to all AG Braun members for their supports. Many thanks to my group members/friends, Dr. Ting Zhang, Dr. Hui Qi, Dr. Angelina Georgieva, Dr. Dong Ding, Dr. Fan Wu, Hang Liu, and Xinyue Guo, for all their supports. It is a valuable memory for life to work together with these dear friends. Thanks to my dear girlfriend, Dr. Fan Wu. Her support, accompany and love alleviating all the bitterness during this study. She could always find a way to cheer me up when I was deeply depressed. I would also like to express my appreciation to Dr. Mario Looso, Dr. Stefan Guenther, and Dr. Carsten Kuenne for the bioinformatics analysis. I have really appreciated the help from the magic hand Marion Wiesnet for the countless adult cardiomyocyte isolation and animal surgery. Finally, I would like to express my gratitude to my parent and my grandparent for the understanding and encouragement. With all your support, I could achieve as much as I can. I dedicate this dissertation to them.